DUST FLOW SEPARATOR

TYPE ELECTROSTATIC PRECIPITATOR

DUST FLOW SEPARATOR TYPE ELECTROSTATIC PRECIPITATOR FOR A CONTROL OF PARTICULATE MATTER EMISSIONS FROM NATURAL GAS COMBUSTION

By

LILI GUAN, B. Eng.

A Thesis

Submitted to the School of Graduate Studies

In Partial Fulfilment of the Requirements

for the Degree

Master of Applied Science

McMaster University

Master of Applied Science (2005) McMaster University

(Engineering Physics) Hamilton, Ontario

TITLE: Dust Flow Separator Type Electrostatic Precipitator For A Control Of Particulate Matter Emissions From Natural Gas Combustion

AUTHOR: Lili Guan

B. Eng. (Electrical Engineering)

Hunan University, Changsha, P. R. China

SUPERVISORS: Dr. J. S. Chang, Dr. G. D. Harvel

NUMBER OF PAGES: xvi, 168

ABSTRACT

Pollution problems have drawn worldwide awareness and become significantly important now. Particulate matter (PM) emission is one of the key pollution issues. Particulate matter has a significant impact on the environment and human health, especially particle sizes that range below 10μm. Researches continuously work an improvement of fine particulate matter collections emitted from all kinds of sources, such as automobiles, industrial combustion, etc. Governments in many countries are planning to regulate the PM emission from the existing PM_{10} (particle diameter<10μm) to new limits $PM_{2.5}$ (particle diameter<2.5μm) within the next few years. For this reason, present PM control system needs to be improved.

The objective of this work is to develop a dust flow separator type electrostatic precipitator (DFS-ESP) for the effective control of fine particulate matter emission from natural gas combustions. The characteristic of PM emitted from natural gas combustion is studied, and the performance of a DFS-ESP is evaluated by experiments and numerical predictions.

An experiment was conducted for natural gas combustion exhaust flow rates from 2.5 to 9 Nm^3/h, ESP applied voltages from 0 to 30kV, and gas temperature from 80 to 160°C. A series of particle measurements were conducted at upstream, downstream and middle of the DFS-ESP system by an optical particle counter for particle mass density, and by condensation nucleate particle counter for particle size distributions and particle

number density. Particle sampled from the natural gas combustion system was also analyzed by an environmental scanning electron microscope (ESEM) technique. Flow velocity profile and pressure drop of the DFS-ESP were measured by a Pitot tube and diaphragm type pressure transducer, respectively.

The experimental results show that the particle size emitted from natural gas combustion ranges from 17 to 300nm in diameter, and the volume density is approximately from 5×10^{8} #pt/m^{3} to 5×10^{9} #pt/m^{3} depending on the combustion conditions. The dust flow separator can concentrate 90% of fine particles in 1 to 3% of the gas flow and divert it from the main flow to the ESP section where the particles can be removed. In terms of overall particle collection efficiency, the DFS-ESP system can remove up to 90% of the particles based on the number density. The pressure drop across the DFS-ESP is observed to be lower than 1Pa for the present range of flow rate, which is within acceptable limits for industrial applications.

ACKNOWLEDGEMENTS

It is a precious opportunity to express my sincere acknowledgements to a number of groups of people for their great contribution and support with my master project.

I would like to thank my supervisors Dr. Jen-Shih Chang and Dr. Glenn D. Harvel for their intellectual research guidance, supervision and the continuous encouragements. I appreciate their valuable time in reviewing my thesis a numbers of times. I also want to express my special appreciation to Dr. Drazena Brocilo for the very helpful suggestions and discussions throughout the research work. Dr. Kuniko Urashima provided me much help in both academic research work and personal life.

My colleagues and research group members, Marcos A. Ara Montrichard, Melissa Nock, Scott Ambridge, Anas Khaial, Steve Shelestynsky, Tatiana Masala, and Dr. Jong Taek Kim, selflessly contributed their time to provide me assistance in the lab, and many useful information. Our technician Greg Ksiazek also gave me a hand in the set up of the experiment rig and solving the technical problems during the experiment.

The visiting scholar, Dr. Sung-Ho Park, is acknowledged for his work of the numerical prediction of DFS-ESP using FLUENT code and for giving the permission to use his raw modeling data for my thesis. Many thanks are also sent to Dr. Su Jian and Dr. Nito Debacher for their suggestions and encouragements with my thesis writing during their stay.

At last, I am deeply grateful to my mom and dad for their understanding, mental support, and irreplaceable love in my life. This dissertation is for them.

TABLE OF CONTENTS

LIST OF FIGURES

LIST OF TABLES

NOMENCLATURE

A	Constant related to ESP configuration for I-V characteristic;
	Cross-section area, (m^2)
C_c	Cunningham correction factor
C_m	Velocity jump coefficient, (=1.146)
C_s	Thermal creep coefficient, (=1.147)
C_t	Thermal jump coefficient, (=2.20)
D_p	Diffusion coefficient, (m^2/s)
d	Particle diameter (m);
	Pipe diameter, (m)
d^*	Kelvin diameter, (m)
d_c	Cylinder diameter, (m)
E	Electric field, (V/m)
e	Electron charge, ($=1.60\times10^{-19}C$)
F_{adh}	Particle adhesive force, (N)
F_D	Stoke drag force, (N)
F_E	Field charging factor
F_{th}	Thermal force, (N)
f	Specific collection area, (m^2)
f_1	Pressure factor for flow rate correction
f_2	Temperature factor for flow rate correction

f_3	Specific gravity factor for flow rate correction
I	Intensity of a light beam;
	ESP corona current, (mA)
Kn	Knudsen number, $(\frac{2\lambda_g}{d_p})$
K	Coagulation coefficient;
	Gas-solid interfacial drag number
K_{th}	Thermophoretic coefficient
k	Boltzmann constant, $(=1.38\times10^{-23} J/K)$;
	Thermal conductivity;
	Factor of dust species, Eq. 2.25
L	Characteristic length of flow channel (m);
	Pipe length, (m)
M	Molecular weight of the condensing liquid, (kG)
m	Index of refraction, (c/V_p)
m_i	Mass of the ion
m_p	Particle molecular mass
$\dot{m}$	Mass flow rate
N	Number density of particles
N_p	Surface charge density
N_s	Saturated surface charge density
n	Number of charges

P	gas pressure, (Pa)
P_s	Saturation vapor pressure
Q	Flow rate
R	Gas constant, $(J/(kg \cdot K))$
R_p	Particle radius
Ra_p	Particle diffusion Reynolds number
Re	Reynolds number
S_c	Schmidt number
S_i	Dimensionless factor (Speed ratio) for particle fielding charging
St	Stoke number
T	Absolute temperature, (^oK)
t	Time
U_0	Velocity of reference flow;
	Flow velocity at entrance;
	Undisturbed air velocity
U_i	Drift velocity of ion
U_p	Velocity of particle
u_{th}	Thermophoretic velocity
V	ESP voltage, (kV)
V_c	Corona-onset voltage, (kV)
V_s	Sparkover voltage, (kV)
V_d	Molecular thermal diffusional velocity

W_e	Particle effective migration velocity
Ehd	EHD number (or Conductive electric Rayleigh number)
Md	Masuda number (or Dielectric electric Rayleigh number)

Greek:

λ_g	Gas mean free path, (m)
λ	wavelength of light
ρ	Density of the condensing liquid
ε_0	Permittivity of vacuum, (=8.854 pF/m)
γ	Surface tension of the condensing liquid
τ	Particle traveling time
τ_{rp}	Particle relaxation time
ν	Kinematic viscosity, (m^2/s)
μ	Dynamic viscosity, ($kg/(m \cdot s)$)
μ_i	Mobility of the ion
η	Flow separation efficiency;
	Particle collection efficiency
$\sum_{2\phi}$	Two-phase interaction number

CHAPTER 1

INTRODUCTION

1.1 AIR POLLUTION AND HEALTH IMPACTS

Environmental problems such as water contamination, air pollution, waste residue, chemical pollution, noise and even heat pollution are drawing more attention now a days. Especially, atmospheric pollution is a globally recognized issue that has been studied since the industrial revolution. The numerous sources of air pollution can be divided into two basic categories: natural sources, such as an erupting volcano, accidental forest fires, dust storms, etc; and anthropogenic sources, including industrial activities such as iron mill, manufactory etc, utilities such as electric power plant, waste disposal facilities etc., and personal sources such as automobile exhaust, incinerator, heating and cooking etc. [2] The pollutants can be categorized as: particulate matter (PM); acid gases such as SO_x, NO_x, HCl, etc; greenhouse gases such as CO_x, N_xO_y, PFC's, etc; ozone depletion substances such as Freon, Halon, etc; volatile organic compounds such as TCE, TCA, toluene, xylene, etc; and toxic gases such as Hg, dioxins, etc. [1]. Various air pollutions are impacting the ecosystem resulting in global warming, decreasing visibility, and harmfully influence for human health [2]. The statistics shown in China from 1990 to 1995 demonstrates that air-pollution-related diseases are becoming the leading cause among all other causes as shown in the Table 1.1, where similar percentage per populations also reported by many countries as well as in many cities in Canada [1].

Table 1.1 Selected causes of death in China [103]

Cause	Approximated Number/yr [1990-1995]
Air-pollution-related lung and heart disease	1,100,000
Smoking-related lung disease, heart disease, and stroke	800,000
Stroke from hypertension	600,000
Infectious diseases, except pneumonia	500,000
Suicide	300,000
Liver cancer from hepatitis, microcystin, and aflatoxin	250,000
Falls and drowning	200,000
Motor vehicle accidents	135,000
Homicide	50,000
Fires and burns	24,000
Coal mining accidents	5,000
All causes, 1995	*8,000,000*

(Source: Environmental Science & Technology, American Chemical Society)

Among all the pollutants, particulate matter (PM) contributes to more severe effects on the both environment and human than normally realized [2]. Particulate matter can be defined in its simplest form as solid or liquid particles suspended in air ranging

from several nanometer to a couple hundred-micrometer diameter. PMs originate from power plants, automobile exhaust, steel manufacturing, pulp and paper plants, food processing, etc. as well as commercial buildings and home ventilation systems [2]. It is statistically estimated that the annual gross mass of anthropogenic-discharged pollutants is over six hundred million tons in a worldwide range, and 16% of them are aerosol particles [4]. It is well known that particles smaller than 10μm (PM_{10}) can be seriously effect to human health, but the degrees of effect directly related to the aerodynamic characteristic of particles. For those particles greater than 10μm, they could be prevented by vibrissa and rhinal mucus due to the inertial effect; smaller particles passing through the nasal region can be deposited on the surface of the tracheobronchial wall by diffusion and removed later by impacts with the walls of the bronchi; while particles less than 2.5μm ($PM_{2.5}$, also named respirable particles) can go deep into human lungs, deposit in the alveolus, and may be transported to systemic apparatus or tissue leading to various health problems. [3,4] For this reason, new regulations on PM control will be adjusted from existing PM_{10} to the new emission limits such as $PM_{2.5}$ within the next few years.

1.2 NATURAL GAS AND ITS EMISSIONS

Natural gas is a vital component of the world's supply of energy. Pure natural gas is a colourless and odourless gas fuel, mainly composed from methane (CH_4), the simplest organic compound. It is produced underground, generally related to the oil deposits.

Uses of natural gas are increasing annually and are an important energy source worldwide. Figure 1.1 shows recent energy consumption in 2002 in Canada for different sources [104]. Natural gas is used for almost all fields, from industrial to residential applications. Figure 1.2 shows the distribution of natural gas use per sector [104].

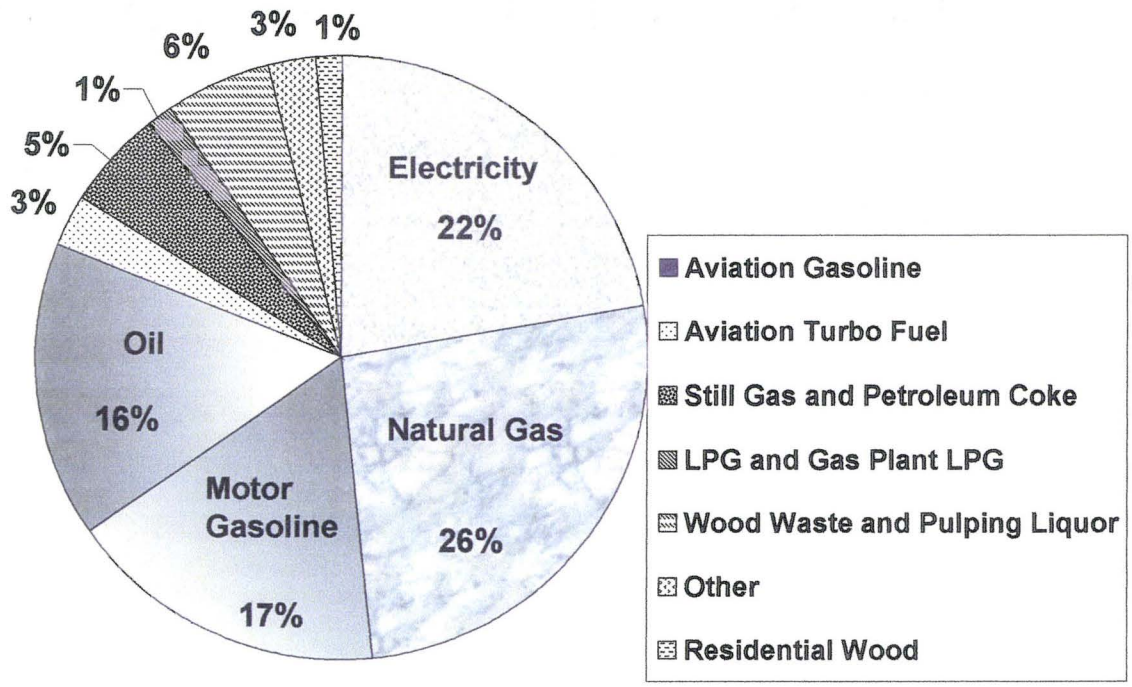

Figure 1.1 Total energy consumed in Canada –2002 [104]

(Data Source: Natural Resources Canada, 2004)

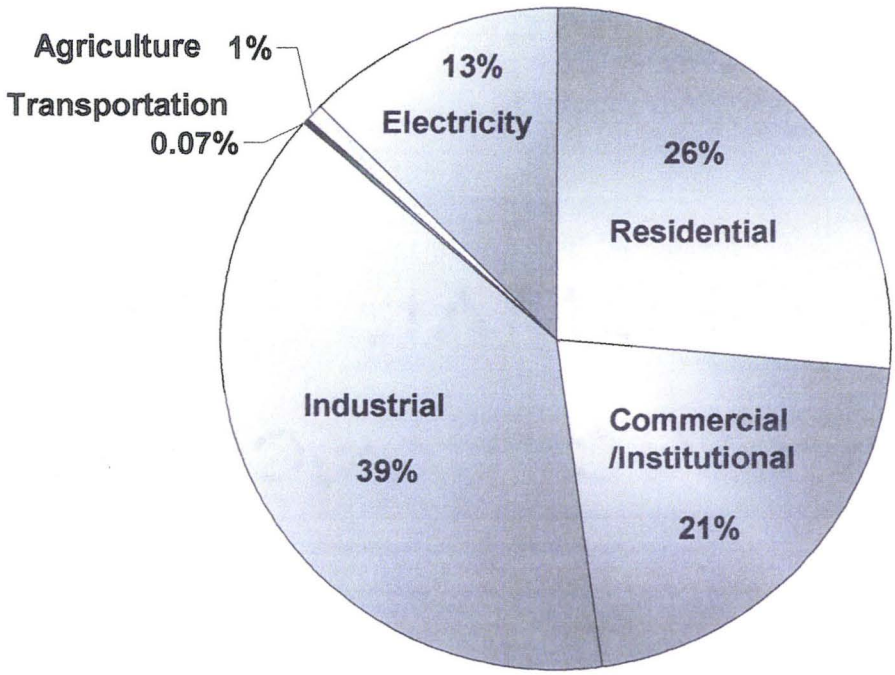

Figure 1.2 Natural gas use in Canada by sector—2002 [104]

(Data Source: Natural Resource Canada, 2004)

The specific gravity of natural gas is approximately 0.6, therefore lighter than air and can dissipate into air very quickly if leaked. The typical composition of natural gas is summarized in Table 1.2 [52].

Table 1.2 Typical composition of natural gas [52]

Methane	CH_4	70-90%
Ethane	C_2H_6	0-20%
Propane	C_3H_8	
Butane	C_4H_{10}	
Carbon Dioxide	CO_2	0-8%
Oxygen	O_2	0-0.2%
Nitrogen	N_2	0-5%
Hydrogen sulphide	H_2S	0-5%
Rare gases	A, He, Ne, Xe	trace

(Data Source: Natural Gas Supply Association, USA)

The combustion of natural gas follows a chemical process such as:

$$CH_4+2O_2 \longrightarrow CO_2+2H_2O+Heat$$

An ignition temperature of 1100 °F to 1200 °F or 593 °C to 649 °C is required to initiate combustion. A natural gas mixture can ignite within a range of 25:1 to 7:1 air-to-fuel ratio by volume. By comparison, a propane mixture ignites within a range 50:1 to 10:1 air-to-fuel ratio by volume. The air to natural gas ratio by volume for complete combustion is approximately 9.5:1 to 10:1. This ratio is not exact because of the slight variations in fuel composition and engine configuration [8].

The combustion products of natural gas are mainly the carbon dioxides (CO_2) and water vapor, in terms of mass concentration. There are also a small amount of nitrogen

oxides (NO_x), carbon monoxide (CO), methane (CH_4), nitrous oxide (N_2O), volatile organic compounds (VOC), trace amounts of sulfur dioxide (SO_2), and particulate matter (PM). Compared to emission from combustion of coal and oil (Table 1.3), natural gas is a relatively cleaner energy source [52].

Table 1.3 Comparison of typical fossil fuel emission level [52]

-Kg per Billion kJ of Energy Input-

Pollutant	Natural Gas	Oil	Coal
Carbon Dioxide	50,301	70,507	89,424
Carbon Monoxide	17	14	89
Nitrogen Oxides	40	193	196
Sulfur Dioxide	0.43	482	1,114
Particulates	3	36	1,180
Mercury	0	0.003	0.0069

(Source: EIA, Natural Gas Issues and Trends, 1998)

Based on the Table 1.3, natural gas releases a smaller amount of greenhouse gas (CO_2), and much smaller ash or particulate matter, so that not many investigations exist that characterized the particulate matter emitted from natural gas combustion. The PM from natural gas combustion has been estimated to be less than 1 micrometer in size and has filterable and condensable fraction [9]. Therefore, characterizing the PM from natural gas combustion becomes one of the primary objectives for this research.

1.3 CONVENTIONAL PARTICLE CONTROL TECHNOLOGY

Particle control technologies or equipment have been developed and commercialized for centuries. There are basically five approaches for removing particulate matters based on different mechanism: settling and momentum separators by gravity, inertia and centrifugal separation such as cyclones, baffle chambers and settling chambers; filtration separators by diffusion, interception, and in certain cases electrostatic forces such as fabric filters, paper filters and baghouse; wet collectors mainly scrubbers by impingement, diffusion, thermal gradients precipitation; acoustic agglomeration resulting from sound waves; and electrostatic precipitation by an electrostatic particle charging.

- ***Centrifugation***

The most commonly used device that separates by the principle of centrifugation is a cyclone. In this case, separation is achieved based on rotating flow, resulting in the initiation of a centrifugal force exerted on the particles to be separated from the gas stream. This centrifugal force is normally at least two orders of magnitude greater than the gravitational force on the particles larger than 3μm [14]. The separation performance of the tangential inlet cyclone can be estimated by Leith and Licht's model [10], which usually depends on the shape of the cyclone, size and density of the particles, and incoming tangential velocity.

- ***Filtrations***

In filtration, solid particles are separated from the gas stream when the gas-solid suspension passes through a single-layer screen, a multiple-layer screen, or a porous, permeable medium, which retains the solid particles. The separation efficiency of a fiber is defined as the ratio of the number of particles striking the fiber to the number, which would strike it if the streamlines were not diverted [11]. For particles larger than 1μm, the particles are collected primarily by inertial impaction and interception; for submicrometer particles and relatively low gas velocity, collection is predominated by diffusion [12].

- ***Settling Chamber***

In a gravity-settling chamber, dusty gas flows horizontal into a large expansion chamber, resulting in the significant decrease in the gas velocity. The particles then settle downward on the collection surface or hopper collectors at the bottom of the chamber. There are two basic types of gravity settling chambers existing in the industries: the simple horizontal flow settling chamber and the multiple-tray settling chamber, where the vertical settling distance is greatly shorter and gas velocity is slightly larger for improving the collection efficiency [14].

- ***Scrubbers***

Wet scrubbers use liquid droplets, films or bubbles to remove fine dust in a gas stream. The function of the liquid medium in scrubbers is similar to that of spherical fibers in filtration. Therefore, the basic cleaning mechanism involved in scrubbing is similar to those in filtration, i.e., inertial impaction, interception, and diffusion. Besides

these, thermophoresis due to the temperature gradients, coagulation and particle growth by condensation are also involved. Three types of commonly used scrubbers are the spray chambers, cyclonic scrubbers, and venturi scrubbers based on the dust flow movement and the water spraying style, where the scrubbers' performance can be evaluated by Fonda and Herne's model [13].

- ***Particle Collection Performance Comparison***

There are normally several criteria for evaluation of dust collector's performance, such as, collection efficiency, pressure drop, energy consumption, economics and maintenance.

Collection efficiency is the ratio of separated particles or dusts to the total inlet as a bulk of dusty gas flowing into the dust collectors, either mass ratio or volume ratio. Besides the gross dust separation evaluation, the partial particle collection efficiency for various particle size ranges is also an important index. Table 1.4 shows the partial collection efficiency based on mass ratio by various dust collectors.

Table 1.4 Typical partial collection efficiency by various dust collectors [14]

Separators	Separation Efficiency (%)		
	50μm	5μm	1μm
Cyclone	96	73	27
Spray Chamber	99	94	55
Dry ESP	99	99	86
Baghouse Filter	99	99	99

Pressure loss across the dust collector should also be evaluated. Large pressure drop would cause higher energy consumption, and might be on-set turbulent flow in the system affecting particle separation. Normally this refers to the time-averaged static pressure. Comparing various types of dust collectors as shown in Table 1.5, ESP is of the lowest ΔP, followed by gravity settling chamber, which the total pressure drop is no higher than 500Pa; cyclones, and baghouse are within the range of 500 to 2000Pa; and that of Venturi scrubber is between 2 to 20KPa.

In terms of the economic evaluation, it includes the cost of equipment investment, and operation and maintenance. Generally speaking, ESP has the highest equipment investment, while cyclone and Venturi scrubber the lowest; however, Venturi scrubber generates the greatest pressure drop, enhancing the energy consumption, as well as the operating and maintenance fee, ESP is on the contrary [4,5]. The characteristics and collection behaviour for existing particle control devices are compared in Table 1.5.

Table 1.5 Comparison of various particle control systems [4, 5]

Dedusting Type	**Devices**	d_p **[μm]**	ΔP **[Pa]**	η **[%]**	**Merits**	**Demerits**
Gravity	Settling chamber	50~100	100~150	40~60	Low cost, easy to maintain	Not practical for ultrafine particles
Inertial	Baffle chamber	50~100	300~700	50~70	Low cost, easy to maintain, suitable for high temperature exhaust	Not practical for ultrafine particles
Centrifugal	Cyclone	>3	500~1500	10~80	Small volume, high temperature gas, condensed particle fluid	High ΔP, not for wet and corrosive exhaust gas
Wet scrubber	Venturi	Small: <1	2500~8000	80~90	High η, less field occupation, high η even for diluted exhaust gas	Large amount of water required, hard to maintain
		Large: >1		90~99		
Filtration	Baghouse	0.1~20	1000~2000	90~99	High η, easy operation, suitable for diluted exhaust gas	Large field occupation, huge amount of fabric demand, not for high temperature
Electrostatic	ESP	0.01~20	100~200	80~99.9	High η, low ΔP, low operation cost, ease of maintenance, suitable for high temperature exhaust	Large field, easy aging, affected by particle resistivity
Acoustic			600~1000	80~95	Low operation cost	High equipment cost

It is summarized in Table 1.5 that an electrostatic precipitator (ESP) is the most effective equipment for removing submicron (d_p<1μm) and even ultrafine particles (d_p<0.1μm) as small as 0.01μm, in addition, its very high collection efficiency for almost all size ranges of particles, low pressure drop, lower operation cost, and ease of maintenance. These benefits together make ESP a popular topic of research and a widely used device for industrial gas cleaning for combustion exhausts, and indoor air cleaning such as home, office, hospital, machine shops, food processing plants etc. [6]

1.4 RESEARCH OBJECTIVE

This research focuses on the control of submicron (d_p<1μm) and ultrafine (d_p<0.1μm) particles from natural gas combustion exhaust. Natural gas is an increasingly important source of energy and used to has been considered as a highly clean source, since the main pollutants from the combustion of natural gas (CO_2, CO, NO_x, and SO_2 except hydrocarbons) are relatively lower than the other fossil fuels, e.g. coal and oil, and PMs are relatively small in terms of mass fraction (mg/m^3). However, recent studies show that a significant number of ultrafine particles are observed from natural gas combustion exhaust, size range below 0.1μm [7], which may be hazardous to human health. Therefore, characterization of the PM emission from natural gas combustion is one of the primary objectives for this research.

The federal and provincial governments in many countries are planning to revise the regulations under the Environmental Protection Act with the proposed Clean Air

program, one of which involves the restriction of particulate matter emission level from PM_{10} to $PM_{2.5}$ in the next few years. Besides the directly generated fine particles from fossil fuel combustion, emissions of environmental concern also included secondary particles formed from gas phases, for example, the ammonia compounds in air often convert NO_x and SO_x into fine ammonium salt aerosol particles or acid rain. [8] However conventional ESPs have several limitations. Firstly, the particle size collection efficiency in terms of number density for the ultrafine- or submicron-particles by a conventional ESP is still relatively low, since these particles are mostly small in mass loading but relatively large in number density [35-39]. Secondly, heavy dust loading can cause corona quenching of the discharge electrode and a high possibility of local rise of electric field in the region near the collecting electrode triggering sparking [39, 73]. Thirdly, the particle re-entrainment can be generated during the rapping process, or back corona [77-80].

Therefore, a dust flow separator type electrostatic precipitator (DFS-ESP) is proposed to solve these problems in PM control from natural gas combustion exhaust.

1.5 THESIS ORGANIZATION

The structure of the thesis is composed in four parts.

In Chapter 2, the existing literature is reviewed and theoretical background is discussed to provide information on approaching the collection of fine particles.

Chapter 3 presents the experimental facilities, design of flow separator and electrostatic precipitator respectively, and measurement techniques used in the experiment.

The experimental results are provided in Chapter 4, including results of the particle characteristics, overall collection efficiency, partial collection efficiency, and pressure drop of DFS-ESP, with comparison to the numerical simulation.

The conclusions are summarised in Chapter 5 and recommendations for future work are provided as a closure in Chapter 6.

CHAPTER 2

BACKGROUND AND LITERATURE REVIEW

2.1 AEROSOL PARTICLES AND AIR POLLUTION

Natural air pollution problems on the earth are as old as the earth itself. A lot of factors contribute to this global problem, such as volcanoes, fumaroles, natural fires, and desert dusts [2,4]. More recently, the burning of coal, chemicals, oil, gasoline, kerosene, diesel, natural gas, and waste and the release of chemicals have contributed to several major air pollution problems on a spatial scale [2,4,16]. Although most air pollution regulations focus on gases, aerosol particles cause more visibility degradation and possibly more human health effects than do gases, and particles smaller than 2.5μm in diameter may cause the additional impacts on health as discussed in the previous chapter.

Therefore, it is crucial to understand the particles characteristics before selecting the control technologies. In this section, the dust particle characteristics from natural gas emissions and particle related pollution issues are reviewed.

2.1.1 Characteristics of Aerosol Particles

The fine particles that suspended in the air are of many kinds: re-suspended soil particles, smokes from combustion, photochemically formed particles, salt particles formed from ocean spray, and atmospheric clouds of water droplets or ice particles. These airborne particles are all examples of aerosols [16]. An aerosol is defined in its simplest form as solid or liquid particles suspended in a gas. Aerosols are two-phase systems,

comprising both the particles and the gas in which they are suspended, and include a wide range of phenomena such as dust, fume, smoke, mist, fog, haze and smog [16, 18].

Particle size is the most important parameter for characterizing the behaviour of aerosols. In general, dust, ground material and pollen are in the micrometer range or larger size, while fumes and smoke are submicrometer or smaller size [16]. In comparison, the wavelength of visible light is in the submicrometer range, about $0.5\mu m$. There are three separate size regimes that can be considered for fine particles in gaseous media near standard conditions (1atm, 20°C) to distinguish the different physical characteristics of various size particles [15], as shown in Table 2.1.

Table 2.1 Knudsen number (Kn) and particle diameter for various size particles in air at standard condition [15]

	Size Regimes		
	Free Molecule	Transition	Continuum
Kn *	>10	10~0.1	<0.1
d, μm	<0.01	0.01~1	>1

**: Kn—particle Knudsen number, will be discussed in section 2.1.2.*

In terms of shape, liquid aerosol particles are nearly spherical, while solid aerosol particles usually have complex shapes, which need to be characterized for each specific case [16,18]. Particles can also be agglomerates of several single particles.

Another very important aerosol property in terms of health and environmental effects is the aerosol concentration. Specifically, mass concentration (mg/m^3) and number concentration (#particles/m^3) are most commonly measured parameters.

The aerosol particles intrinsic characteristics affect their motion and the related processing mechanism, such as adhesion, diffusion, coagulation, condensation, thermal precipitation, electrical and optical properties. They are discussed in detail in the following sections. The characteristics of particles are also presented.

- ***Adhesion***

The characteristic that the aerosol particles can attach firmly to the surface they contact is one that distinguishes them from gas molecules. The adhesion could be the function of Van der Waals force, electrostatic force, or the surface tension of adsorbed liquid films, which are affected by the particles' physical properties such as shape, size and material; by surface condition of the attached matter; and by environment temperature, relative humidity, particle-to-surface contact duration, and particle initial velocity [16].

The experimental measurements for adhesive forces, based on determining the force required to separate a particle from a surface, can be expressed [16] as follows,

$$F_{adh} \cong 1.5d[0.5 + 0.0045(\%RH)] \times 10^{-3} \quad (2.1)$$

where the force F_{adh} is in Newton, particle diameter d is in centimetres, and %RH is the relative humidity in percent. Equation 2.1 is based on direct measurement at 25 °C and available for hard and clean surfaces.

The adhesive forces are proportional to particle size d while separation forces are proportional to d^3 for vibration and centrifugal force or d^2 for airflow [16]. Thus, it is increasingly difficult to remove particles from surfaces for decreasing particle sizes. As shown in Table 2.2, adhesive force on particles less than 10μm is much greater than other forces they could experience, in which, the adhesion is calculated by Equation 2.1 for 50%RH.

Table 2.2 Comparison of various forces on spherical unit-density particles [16]

Diameter *[μm]*	**Adhesion** *[N]*	**Gravity** *[N]*	**Airflow (at 10m/s)** *[N]*
0.1	$1x10^{-8}$	$5x10^{-18}$	$2x10^{-10}$
1.0	$1x10^{-7}$	$5x10^{-15}$	$2x10^{-9}$
10	$1x10^{-6}$	$5x10^{-12}$	$3x10^{-8}$
100	$1x10^{-5}$	$5x10^{-9}$	$6x10^{-7}$

Solid particle collection methods such as impactors and fibrous filters are dependent on adhesion of particles to surfaces, but the particle re-entrainment problem would reduce its collection efficiency.

- ***Diffusion***

Diffusion is the primary transport mechanism for particles less than 0.1μm in diameter. It is the net transport of particles doing Brownian motion in a concentration gradient. Fick's first law of diffusion defines the relationship of the flux of aerosol particles J and the concentration gradient by [16],

$$J = -D_p \frac{dn}{dx} \tag{2.2}$$

where J is the net number of particles traveling through $1cm^2$ each second; and D_p is the diffusion coefficient, which can be expressed by Stokes-Einstein equation [17],

$$D_p = \frac{kTC_c}{3\pi\mu_g d} \tag{2.3}$$

where k is Boltzmann's constant; T is absolute temperature; μ_g is the gas viscosity; d is particle size in diameter; and C_c is the Cunningham correction factor (also known as slip correction factor), which is expressed by [16],

$$C_c = 1 + Kn \cdot [1.257 + 0.4\exp(-\frac{1.10}{Kn})] \tag{2.4}$$

The relationship between Cunningham correction factor and particles diameter is shown in figure 2.1 at standard conditions. Cunningham correction factor increases greatly as size decreases for particles smaller than 1μm. Therefore, Cunningham correction factor must be applied for particles diameter less than 1μm. From Equation 2.3, the diffusion coefficient is proportional to temperature, i.e., as increasing the temperature,

particle Brownian motion becomes more vigorous and the mass transfer in a concentration gradient (diffusion) is therefore more rapid, as expected from the similar relationship for gas molecules by Einstein [17]. It is also concluded from Eq. 2.3 that for particle size large enough to neglect the Cunningham correction factor, D_p is inversely proportional to particle diameter d; for those with large C_c, D_p is inversely proportional to d^2. Effect of particle size on the diffusion coefficient for temperature from 0 to 300°C is shown in Figure 2.2. A 0.01μm particle will be transported by diffusion approximately 20,000 times faster than a 10μm particle under the same condition.

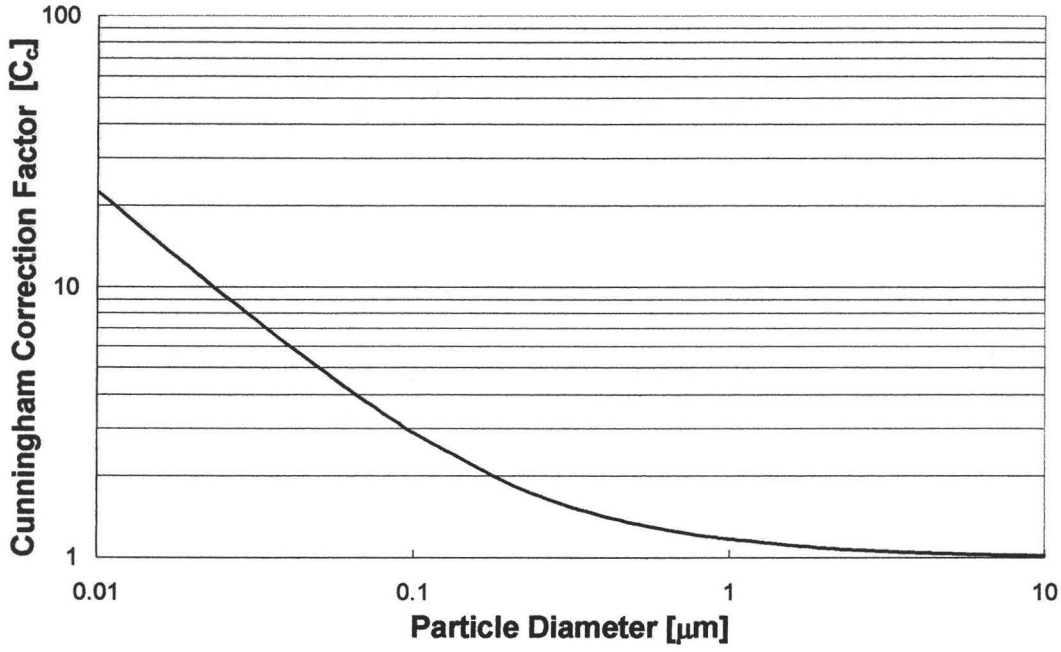

Figure 2.1 Cunningham correction factor versus particle diameter at Standard Conditions

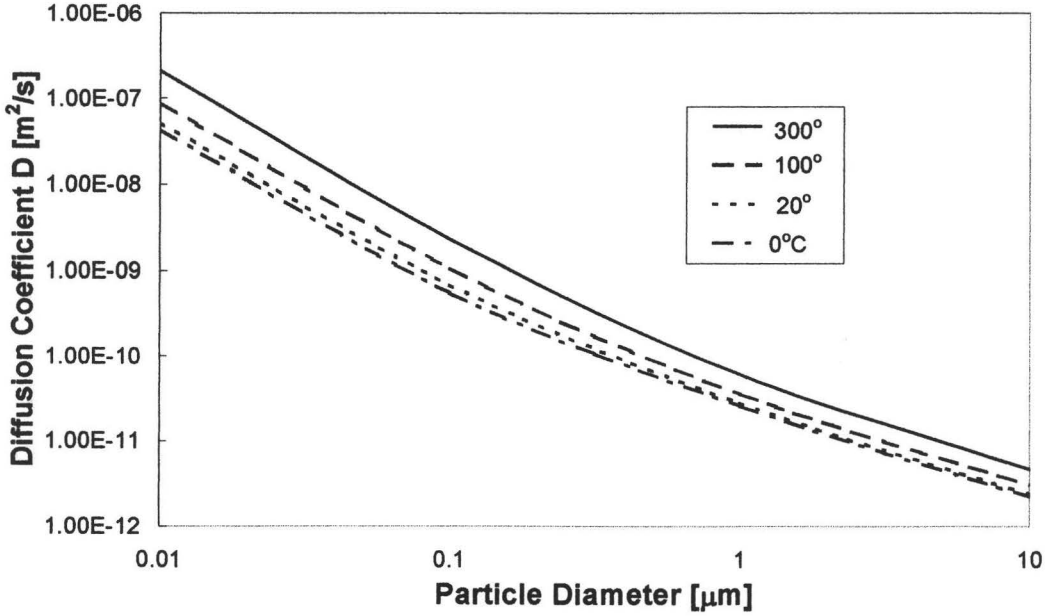

Figure 2.2 Diffusion coefficient versus particle diameter for temperature from 0 to 300°C

Classic kinetic theory indicates that gas molecules with Brownian motion will rebound when they collide with a surface after a momentum transfer process. As discussed in section 2.1.1, unlike the gas molecules, particles tend to adhere to the surface when they collide with. This would establish a continuous diffusion of aerosol particles to the surface by the concentration gradient and leads to a gradual decay in concentration.

- ***Thermophoresis***

Temperature gradient can exert a force on particles moving them toward the colder region. A motion of fine particles resulting from this thermal force is so-called thermophoresis. The steady state molecular thermal diffusional velocity can be derived from Nernst-Einstein equation [18] as follows:

$$V_d = \sqrt{\frac{8kT}{m_p}} \tag{2.5}$$

This shows particles move faster under warmer condition, therefore the interaction between particles can become more active and cause greater momentum exchange when the collision occurs. As a result of this process, particles are pushed away from warmer side and deposit on the colder surface.

Equation 2.5 also shows that particle motion by thermophoresis is also a function of particle properties. For example, smaller particles experience greater momentum transfer for the same species. Waldmann and Schmitt [19] estimated the theoretical thermal force on the particles in free molecule regime ($d<\lambda$) by,

$$F_{th} = \frac{-p\lambda d^2 \nabla T}{T} \tag{2.6}$$

where p is the gas pressure, λ the gas mean free path, and T the absolute temperature of particles. Equation 2.6 shows that thermophoresis force is proportional to d^2 for particles in the free molecule regime. The thermophoresis motion of particles can also be described by the thermophoretic velocity (u_{th}) by [20],

$$\bar{u}_{th} = -K_{th} \frac{\nu_g}{T_g} \nabla T_g \tag{2.7}$$

where ν_g is the gas kinetic viscosity, T_g the gas temperature, and K_{th} is the thermophoretic coefficient given by Talbot et al. [20] for the full range of Knudsen number as follows,

$$K_{th} = 2C_s \frac{(k_g / k_p + C_t Kn)[1 + Kn(1.2 + 0.41e^{-0.88Kn})]}{(1 + 3C_m Kn)(1 + 2k_g / k_p + 2C_t Kn)} \tag{2.8}$$

where k_g and k_p are the thermal conductivity for gas and particle respectively, C_s the thermal creep coefficient=1.147, C_t the temperature jump coefficient=2.20, and C_m the velocity jump coefficient=1.146.

There are many models for prediction of particle deposition by thermophoresis. For example, Nisho et al. [21] predicted the thermophoretic deposition of aerosol particles ranging in 0.3~1.3μm in a counter-current heat exchanger tube at the tube inlet for both laminar and turbulent flow, and confirmed the prediction by experiments. Byers and Calvert [22] analyzed the particle thermophoretic deposition for slug flow. Romay et

al.[23] studied the thermophoretic deposition of aerosol particles ranging in 0.1~0.7mm for pipe flow at Reynolds number from 4000 to 10000.

- ***Coagulation***

Coagulation is the process where aerosol particles collide with each other due to a relative motion between them and adhere to form larger particles. Thermal coagulation is based on the particles Brownian motion; while kinetic coagulation is based on the external force such as gravity or electrical forces. For solid particles, this process is normally called agglomeration and the resulting particle clusters as agglomerates.

Coagulation is a very complex process. Smoluchowski [16] starts the basic approach from the diffusion theory for simple monodisperse spherical particles and Fuchs [15] defined the coagulation coefficient (K), indicating that coagulation is independent from the particles size for those where slip correction is negligible, while for small particles affected by the slip correction factor K is increasing as decreasing the particle size, as shown in figure 2.6. K can be expressed by [16],

$$K = \frac{4kTC_c}{3\mu_g} \tag{2.9}$$

Substituting the standard conditions (1atm, 20°C) into Equation.2.9, the coagulation coefficient can be simplified to,

$$K = 3.0 \times 10^{-10} C_c \ [cm^3/s] \tag{2.10}$$

Figure 2.3 shows the coagulation coefficients as a function of particle size calculated by Equation 2.10. For particle diameter less than 1μm, K is inversely proportional to particle size, while for particle size larger than 1μm, K is not affected by size.

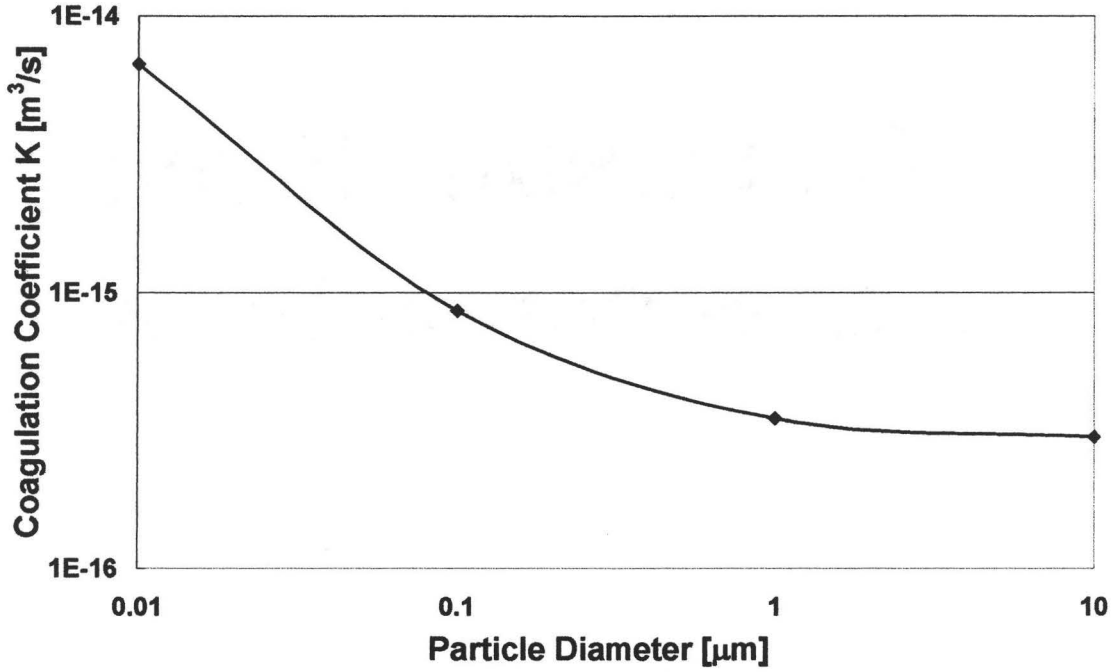

Figure 2.3 Coagulation coefficients at standard conditions

- ***Condensation***

The condensation process is formed when presenting a supersaturated vapor and initiating nuclei or ions as particle formation bases, also named *heterogeneous condensation*. Another type of condensation, *homogeneous condensation*, happens when the supersaturation becomes high enough. The degree of supersaturation is measured as a saturation ratio, P/P_s, a ratio of the actual vapor partial pressure (P) and the saturation vapor pressure (P_s) for a given temperature. Gas-vapor supersaturation is corresponding

to a saturation ratio greater than one. If equal to one, the gas-vapor is saturated and if less than one, the gas-vapor is unsaturated. Particle size is a vital factor affecting heterogeneous condensation for a given saturation ratio, and the minimum particle size required for this process is defined as the *Kelvin diameter*. The relationship between particle Kelvin diameter and the saturation ratio required for equilibrium is developed in *Kelvin* or *Thomson-Gibbs equation* [16],

$$\frac{P}{P_s} = exp[\frac{4\gamma \cdot M}{\rho RTd^*}] \tag{2.11}$$

where γ is the surface tension of the condensing liquid; M is molecules weight of the condensing liquid; ρ is density of the condensing liquid; R is the gas constant; and d^* is Kelvin diameter.

Particles with condensate droplets would neither grow nor evaporate for particles with a Kelvin diameter at one specific saturation ratio based on Equation 2.8. If P/P_s is greater than this saturation ratio value, the particle size grows to a new corresponding equilibrium. When P/P_s is less than this value, droplets evaporate until reaching another new equilibrium. This effect is called the Kelvin effect and is significant only for particles less than 0.1μm.

The most commonly useful application for the particle condensation process is the condensation nuclei particle counters (CNPC), which plays an irreplaceable role in the particles number concentration and size detection for the present project as discussed in Section 3.4.

- ***Electrical properties***

Due to electrical properties, particles can be charged and influenced by electrostatic forces. The motion induced by electrostatic force forms the basis for important types of air-cleaning equipment and aerosol sampling and measuring instruments, such as Electrostatic Precipitators.

The presence of unipolar ions is the prerequisite for the particle charging. The amount of ions depositing on a particle determines how well it is charged, which could be affected by the ions residence time, particle radius and shape, external electric and magnetic fields, particle velocity, etc.

Since unipolar ions are required for the field charging and diffusion charging, and very short lifetime of such ions exist due to their mutual repulsion and high mobilities, it is crucial to have a continuously generated ion source. Only corona discharge can produce unipolar ions at a stable and high enough concentration for aerosol charging while the many other methods, such as radioactive discharge, ultraviolet radiation, and flames [16] are for bipolar ion generations.

The details of particles electrical properties would be reviewed in section 2.3.2.

- ***Optical properties***

Based on classic kinetic theory, a beam of light (i.e. electromagnetic radiation) passing through a region of space occupied by an aerosol will suffer a decrease in intensity. The loss of energy from a beam of radiation results from the processes of absorption and scattering by the particles. These optical properties of aerosols are

responsible for many spectacular atmospheric effects, such as colourful sky, rainbows, sunsets, etc. The most noticeable negative effect is visibility degradation.

The process of scattering and absorption is typically presented by the fractional change of intensity (dI/I) of a beam of radiation passing through a material with dx thickness,

$$\frac{dI}{I} = -C_{ex}dx \tag{2.12}$$

where, C_{ex} is the extinction (attenuation) coefficient, representing the total contribution of all particles within the dx thickness material to the processes of scattering and absorption. Research indicated that the intensity also varies with the particle size, concentration, and refractive index [24-28]. The scattering of light by very small particles, those less than 0.05μm in diameter, is described by Rayleigh's theory [16], the theory of free molecular scattering. The scattering by particles greater than 100μm can be analyzed readily by geometric optics, the tracking of refracted rays of light through the particle; and in between these sizes, is the Mie scattering region [16], where the particle size and the wavelength of light have the same order of magnitude.

Two theories developed by *Rayleigh* and *Mie* [16] are used to determine quantitative expressions for the light scattering intensity. For Rayleigh scattering, the electromagnetic field is uniformly distributed over the small particle, and all the induced dipoles re-radiate light (the scattered light) equally in all directions, where the scattered intensity for unpolarized incident light cannot be analyzed by this model [16],

$$I(\theta)=\frac{I_0\pi^4 d^6}{8R^2\lambda^4}\left(\frac{m^2-1}{m^2+2}\right)^2(1+\cos^2\theta) \tag{2.13}$$

where $I(\theta)$ is the total intensity of light scattered in the direction θ at a distance R from the particle.

For Mie theory, the dipoles are not uniformly distributed and a vector sum has to be carried out to determine the total scattered intensity at a certain point. This scattered intensity is a strong function of the angle with respect to the incident beam. Mie scattering theory provides a complicated but very general solution to the problem of scattering by spheres, where the more accurate models were also presented by Van de Hulst [29], and Kerker [30] etc.

Light scattering provides an extremely sensitive tool for the measurement of concentration and particle size of aerosols due to the advantage of minimally disturbing the aerosol and providing instantaneous information often suitable for continuous monitoring. The most commonly used tool is an Optical Particle Counter (OPC). Sachweh et al. [31] shows that OPCs can be operated up to 10^7 #pt/cm^3 without dilution. Umhauer and Berbner [32] observed that the electrical signals obtained from the system are (disregarding changes in Rayleigh scattering background) independent of pressure, composition and viscosity of the gas, and can be performed over a wide range of temperatures.

Based on above examination on particle characteristics, it is possible to analyze and design particles' measuring and removing mechanisms.

2.1.2 Particle Characteristic Parameters

Various groupings of physical parameters are useful to identify specific properties of a given PM system. Some of these numbers can be considered ratios of forces or effects in the system so as to be dimensionless, and these numbers are necessary in the study. These numbers are reviewed and explained in detail as follows:

- *Diffusion Reynolds Number of Particle (Ra_p)*

An expression of particle flow is needed when the particle moves in an unconfined fluid medium or in a system where the walls of the device have essentially no effect on the particle [16]. The particle diffusion Reynolds number used for this is,

$$Ra_p = \frac{U_0 \cdot L}{D_p} \tag{2.14}$$

where U_0 is the characteristic flow or reference flow, L is the characteristic length (i.e., flow channel width or diameter), and D_p is the diffusion coefficient of particles.

- *Mean free path (λ)*

In many situations, the discontinuous nature of the gas has to be taken into account, i.e., the gas should be treated as groups of rapidly moving molecules randomly colliding with the particles. The criterion for such an approach depends on the particle size relative to the spacing between molecules. Mean free path is defined as the average distance traveled by a molecule between successive collisions [18]. The mean free path λ of a gas can be determined from the average number of collisions a particular molecule

has in one second (n_g) and the average distance it has traveled in that second. Kinetic-molecular theory predicts that the mean free path for a gas can be estimated using [16]:

$$\lambda_g = \frac{\mu_g}{0.499\rho_g}\sqrt{\frac{\pi M}{8RT}} \approx \frac{\mu_g}{\rho_g}\sqrt{\frac{\pi M}{2RT}} \tag{2.15}$$

where μ_g is the viscosity of gas or fluid, ρ_g is the gas density, M is the molecular weight, T is the absolute temperature (°K), and R is the universal gas constant. In metric units, the value of R is 8.314kJ/(kmole·°K).

For air at standard conditions (1 atmosphere and 20°C), the mean free path predicted by Equation 2.15 is about 6.60×10^{-8} m.

A simplified expression of mean free path can be derived by adapting the kinetic theory equation to the Glasstone [33] viscosity relationship used for air near standard conditions:

$$\lambda_{air} = (2.26\times10^{-5})\frac{T}{P} \tag{2.16}$$

where P is the pressure in millibars (mb) and T is the absolute temperature in °K. At standard conditions, the mean free path of air is about 6.53×10^{-8} m (6.53×10^{-2} μm) predicted by Equation 2.16.

- *Knudsen Number (Kn)*

The Knudsen number is used to evaluate how far a gaseous system, including the particles, deviates from the normal (continuum state) [34]. It is defined for any positive

number and zero. As Kn becomes smaller, the gas acts more normal and behaves as a continuum. The Knudsen number is:

$$Kn = \frac{2\lambda_g}{d} \tag{2.17}$$

where λ_g is the mean free path of the gas molecules. According to this definition, Kn can vary for a given size particle depending on what gas is present and whether a gas is hot or cold [34]. Kn is a very important indicator in particle size characterization.

- *Schmidt Number for particles (Sc_p)*

This number considers the diffusivity of particles and for isothermal mass transfer is analogous to the Prandtl number in heat transfer. The Schmidt number correlates the properties of viscosity, density and diffusivity whereas the Prandtl number correlates specific heat, viscosity and thermal conductivity. Both are relatively independent of pressure and temperature when conditions are near standard conditions. The Schmidt number for particles is:

$$Sc_p = \frac{\mu_g}{\rho_g D_p} = \frac{\nu_g}{D_p} \tag{2.18}$$

Brownian diffusivity becomes less significant compared with convective motion of particles, as $ReSc_p$ increases in value.

- *Cunningham Correction Factor (C_c)*

An important assumption of Stokes's law is that the relative velocity of the gas right at the surface of the sphere is zero. This assumption is not suitable for fine particles whose size approaches the mean free path of the gas. Such particles settle faster than predicted by Stokes's law because there is "slip" at the surface of the particle. At standard conditions this error becomes significant for particles less than 1 μm in diameter. Cunningham derived a correction factor for Stokes's law to account for this effect. The factor, called the Cunningham correction factor C_c, is always greater than one and reduces the Stokes drag force by

$$F_D = \frac{3\pi\mu_g U_p d}{C_c} \tag{2.20}$$

For particles less than 1 μm, because the Cunningham correction factor increases rapidly as size decreases, the Cunningham or slip correction factor must be applied [16].

2.2 CONTROL OF FINE PARTICULATE MATTERS

At present, devices for particulate matter control are commercially available based on five fundamental mechanisms as per discussion in Chapter 1. However, present pollution control devices cannot efficiently remove those particles ranging in submicron or ultrafine level to satisfy the upcoming new regulations on particle emissions. ESP and baghouse filters are the most common industrial particulate control systems. Based on the discussion in section 1.3, the baghouse filter can collect submicrometer particles with high efficiency; however, it generates high pressure drop. Conventional ESP can remove

more than 99% particles in terms of mass particle density (mg/m^3), while below 50% particle collection efficiency in terms of number particle density ($\#particles/m^3$) [35-39], since most of the submicrometer particles escape from the ESP due to insufficient particle charging and flow instabilities by EHD induced flow and onset of turbulence [40-45].

Several attempts are proposed to improve collection efficiency of submicron particles as follows:

- Physical agglomeration of the fine particles by ultrasonic [46-48] and electrostatic agglomerates [49,50];
- Chemical agglomeration of the fine particles by conditioning agents such as ammonia, ethanol amines, etc [38,51];
- Thermal precipitation [53];
- Electron particle charging [6,54];
- Wet electrostatic precipitation [6,55,51].

Electrostatic [49,50] and sound-wave [46-48] have been applied for the particle agglomerations. The chemical agglomeration, the thermal precipitation and the enhancement of electron particle charging by short pulse corona energization can also be considered. The short pulse energization of an ESP generates much higher electron density than dc energization, therefore enhances particle charging due to much larger mobility of electrons, and improves the fine particle collection efficiency [55-59]. The ultrafine particle collection efficiency under a pulse-energized ESP has been investigated by Zukeran et al. [76]. However, most of these techniques remain under investigation.

2.3 ELECTROSTATIC PRECIPITATOR

Since the first electrostatic precipitator (ESP) was invented by F. G. Cottrell in 1906 [4], ESPs are continuously of great interest in industrial and scientific research because of its obvious high collection efficiency and many other advantages over the other particulate control devices. Figure 2.4 describes the basic working principle of the wire-plate type ESP as an example.

It fundamentally consists of two electrodes, discharge and collecting. Under certain values of applied voltage, corona discharges are generated. When particles flow through the ionized field, some ions could collide and deposit to the particle surface by either diffusion charging or field charging. By Coulombic force charged particles migrate towards the collecting electrode due to the electric field, release the ions and then sediment (i.e. precipitate). As particles accumulate to the collection electrode to a certain thickness, proper post treatment (rapping or rinsing) devices are operated to clean the collection electrode. Negative corona has lower onset voltage and higher spark-over voltage, i.e. the working range is much broader in negative corona than in a positive one, enabling relative stable operation under harsh conditions. Thus, negative corona is used in industrial gas cleaning. However, positive corona generates much less ozone than a negative one, so that positive corona is employed in the indoor environment for air purification [6].

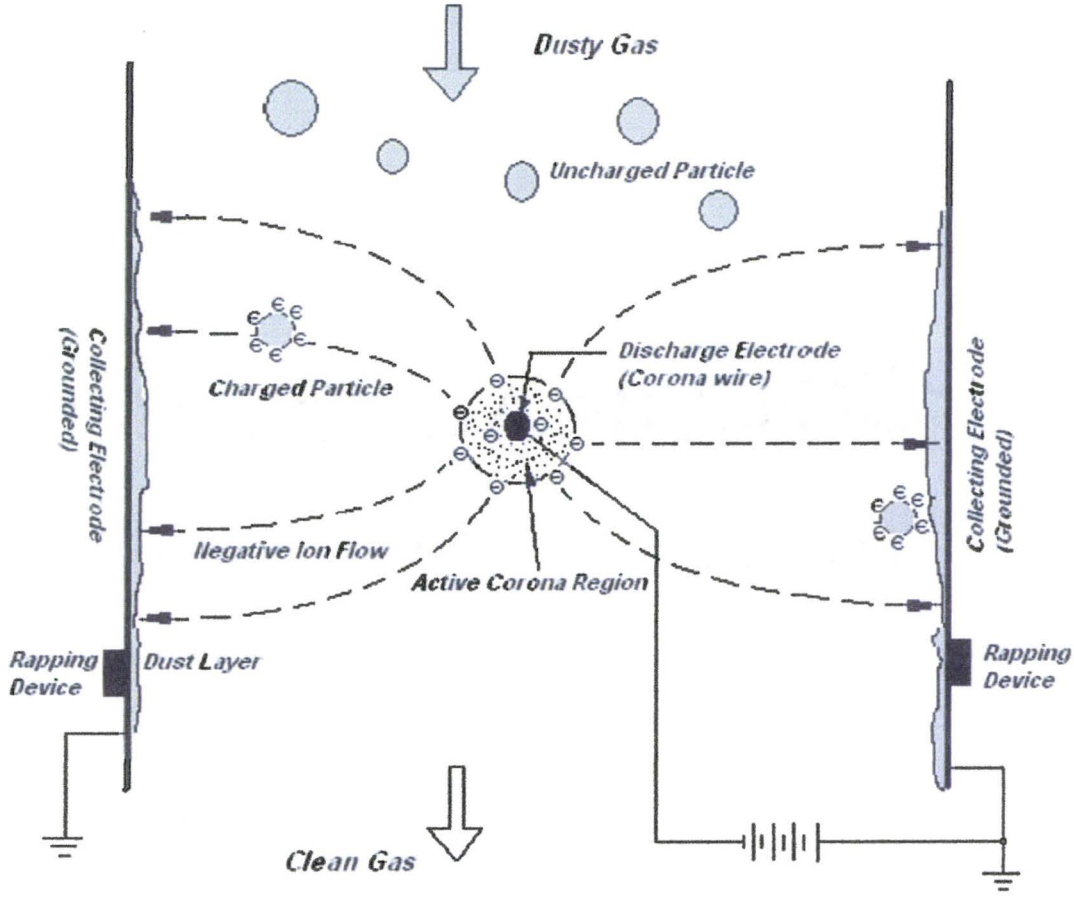

Figure 2.4 The working principle of ESP

ESP has been developed in many different geometry for various applications, such as *wire-pipe* or *wire-plate type* depending on the collecting electrode geometrics; *vertical* or *horizontal type* depending on the flow direction of treated exhaust gases; *wet* or *dry type* depending on the method of post treatment of the dust layer; and *one-stage* or *two-stage* type depending on the arrangement of the particle-charging area and the particle-separating area [4, 6].

Physics of the ESP will be theoretically reviewed in the following section, for improving its performance and better utilizing in present research project.

2.3.1 Particle Charging by Unipolar Ions

- ***Diffusion Charging***

The process of particles charging by random collisions to unipolar ions is called unipolar diffusion charging, because of the Brownian motion (thermal diffusion) of ions and particles. Many literatures have developed the theory of diffusion charging for spherical particles with continuum (d>1.3μm) and free molecule (d<0.01μm) size conditions [60-68]; and the theory of diffusion charging on aerosol particles of arbitrary shape has been developed for continuum to free molecule regimes by Chang [69]. An approximate expression for the number of charges (n) acquired by a particle of diameter (d_p) by diffusion charging during a time t for free molecule conditions is [61],

$$n = \frac{2\pi\varepsilon_0 dkT}{e^2} ln(1 + \frac{e^2 N_0 d}{2\varepsilon_0 \sqrt{2m_i \pi kT}} t) \tag{2.21}$$

where ε_0 is the permittivity of vacuum, ($8.854pF/m$); k is the Boltzmann constant, ($1.38 \times 10^{-23} J/K$); e is the electron charge, ($1.60 \times 10^{-19} C$); N_0 is the initial ion density before charging; and m_i is the mass of ion. An example of calculated results for numbers of charges acquired by various particle diameters versus time by equation 2.21 is shown in figure 2.5.

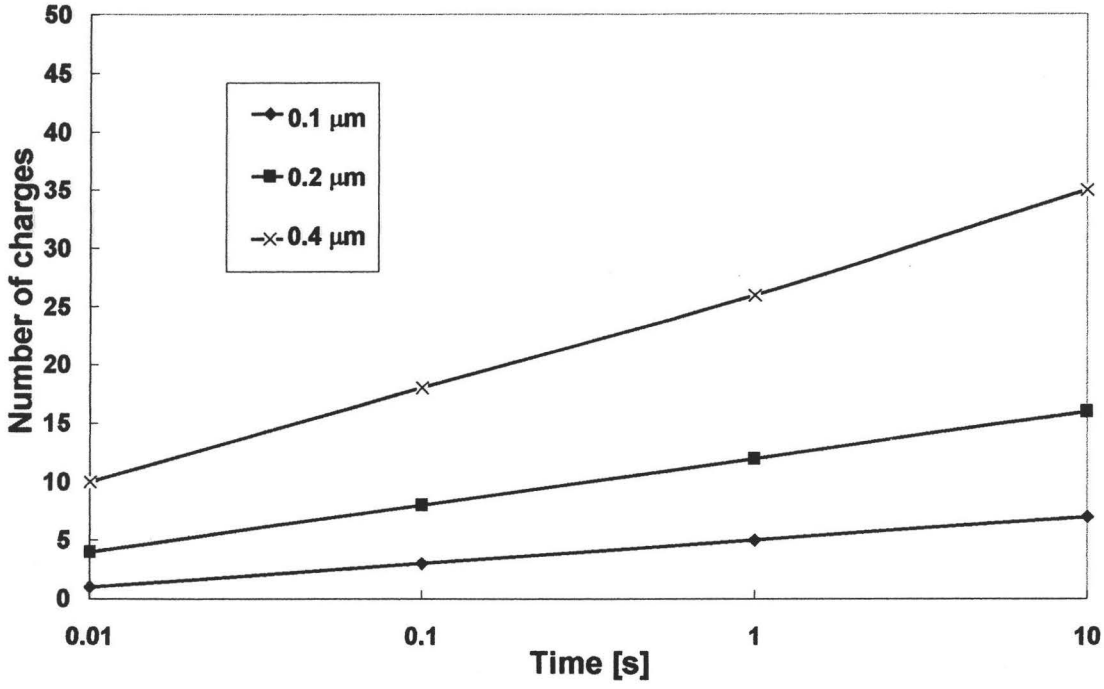

Figure 2.5 Number of charges for various spherical particle diameters versus time

- ***Field Charging***

Another particle charging mechanism is *field charging*, which is formed when it is under the influence of an external electric field E and when the field charging factor F_E becomes much larger than 1 [69], where $F_E = eER_p / kT$. Brock [70], Brock and Wu [71], and Parker [68] developed the theory of unipolar charging of aerosol particles under an electric field for free molecule particle size regime ($d<0.01\mu m$). Parker [68] and Chang et al. [72] have used a dimensionless factor $S_i = U_i / (2kT / \pi m_i)^{1/2}$ to analyze the effect of an external field on the particle charging under free molecular conditions, where $U_i = e\mu_i E$ is the drift velocity of the ion, E is the external electric field, μ_i is the

mobility of the ion, and m_i is the mass of the ion. For continuum condition, the relationship of surface charge density and time can be derived as [73],

$$N_P = N_s \frac{t}{t + t_0} \tag{2.22}$$

$$t_0 = \frac{4\varepsilon_0}{eN_i\mu_i} \tag{2.23}$$

$$N_s = \frac{12\pi\varepsilon_0 R_p^{\,2} E\varepsilon_s}{\varepsilon_s + 2} \tag{2.24}$$

where N_P is the surface charge density; N_s is the saturated surface charge density; R_P is the particle radius; and E is the external electrical field. From Equation 2.22, t_0 can be considered as a time constant for evaluating how fast a dust particle can be charged. When $t=t_0$, surface charge density would be 50% of its saturation value; when $t=10t_0$, *90%* is reached; and *99%* when $t=100t_0$. Therefore, when t_0 is relatively small, the rate of particle field charging is fast; vice versa, as shown in Figure 2.6.

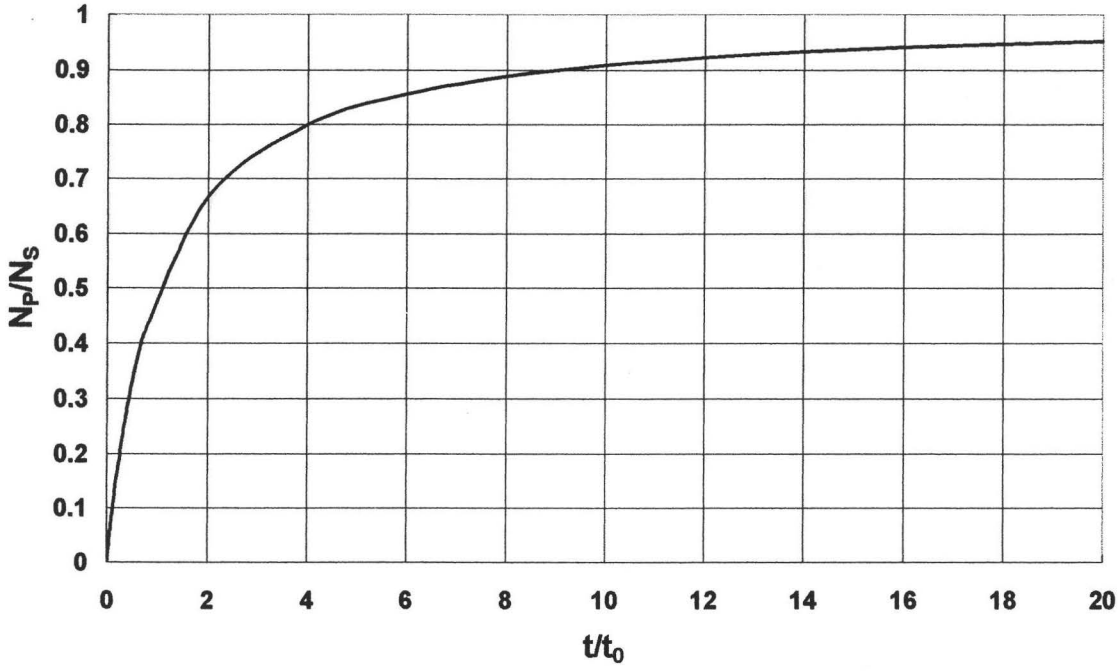

Figure 2.6 Time-dependent of spherical particle charge by field charging

Unlike the field charging, unipolar diffusion charging has no saturation charge value, since diffusion charging is closely related to the Brownian motion, the ions in equilibrium with the gas molecules have a Boltzmann distribution of velocity which has no upper limit, resulting in the charging rate are slowly approaches zero [16].

In the real case, field charging and diffusion charging will both function on the particles flowing through an ionized region. Liu and Kapadia [74] present results of numerical analysis for the situation where both mechanisms are important. The charge acquired is proportional to d_p^2 in field charging and to d_p in diffusion charging, therefore field charging is the dominant mechanism for particles larger than $1 \mu m$ and diffusion

charging is the dominant mechanism for particles less than $0.1\mu m$ even in the presence of a weak electric field, as predicted by Masuda et al. [6] as shown in the Figure 2.7.

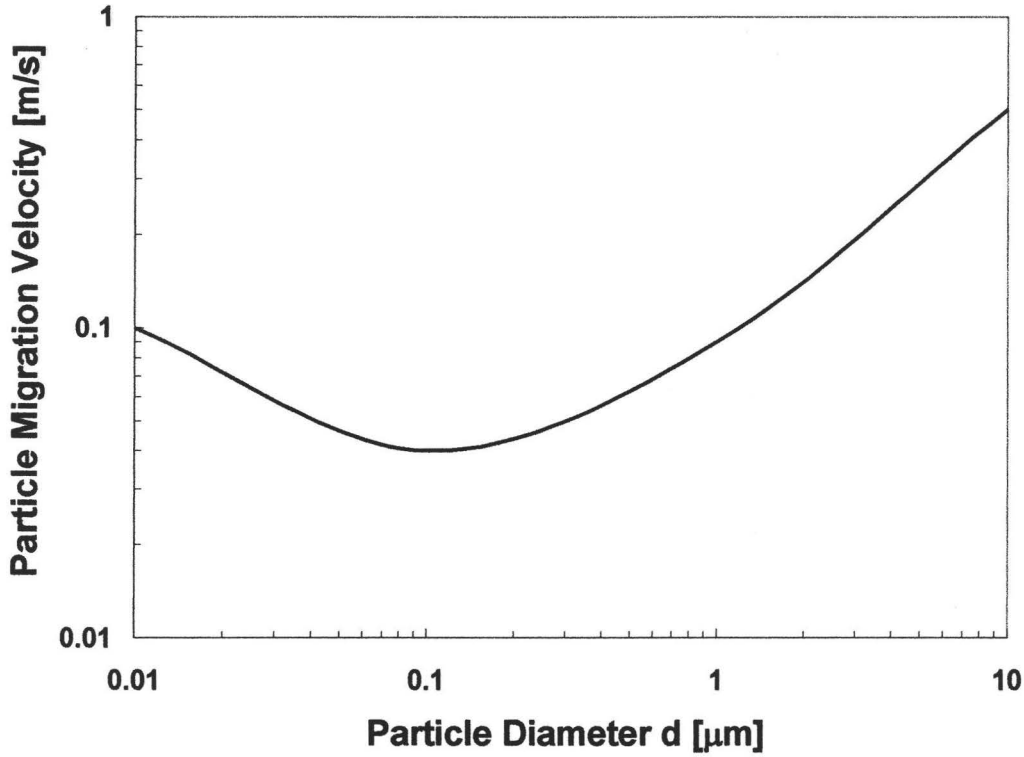

Figure 2.7 Typical theoretical migration velocity vs. particle radius [6]

Matts and Ohnfeldt [75] modified the Deutsch equation of ESP collection efficiency as follows:

$$\eta = 1 - exp(-W_e f)^k \tag{2.25}$$

where W_e is the particles effective migration velocity, a product of charged particles mobility (μ_d) and electric field (E), and f is the specific collection area, k is the factor depending upon dust species, such as 0.5 proposed by Matts [75] for coal fly ash. For Deutsch model, k is usually selected in the range of 0.5 and 1 [75].

2.3.2 Current-Voltage Characteristic of ESP

ESP time averaged current-voltage characteristic is always the first thing to be examined under each different experiment conditions. The schematics of I-V curve of corona discharge is shown in figure 2.8.

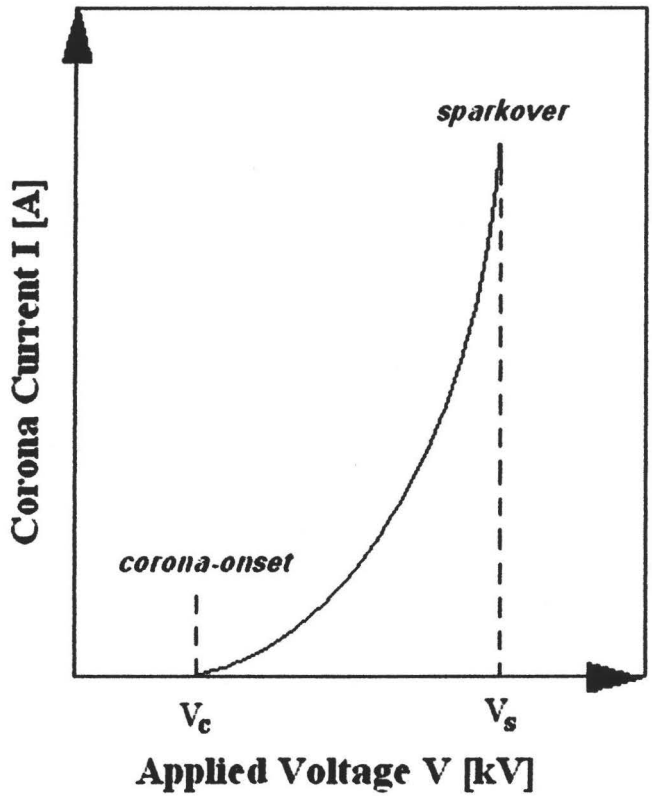

Figure 2.8 Schematics of time averaged current-voltage relationship for corona discharge

The applied voltage must be increased to exceed a specific threshold, the corona-onset voltage (V_c), before corona discharge starts to occur on the surface of the discharge electrode. Glow dots can be observed along the discharge electrode. The increasing current will follow an exponential relationship to the voltage above corona-onset. This relationship can be expressed in the fashion of,

$$I = A \cdot V \cdot (V - V_c) \tag{2.26}$$

where A represents a constant related to ESP configurations, temperature, pressure, and composition of the gas. When further increasing the applied voltage to a certain value (the sparkover voltage), sparking occurs, and glowing turns into arcing. So the current-voltage characteristic describes the relationship and reflects all possible operational conditions of a precipitator. The higher the applied voltage, the better the collection performance under normal conditions, where no back corona is occurring. The range from V_c to V_s is generally much broader and more stable in negative corona than in positive one. This is also the reason that negative corona is normally utilized in most of the industrial ESP.

2.3.3 Factors Influencing ESP Performance

The predominantly high performance of ESPs could be often influenced by various factors in the practical processes.

- ***Particle Size***

As indicated in the Figure 2.7, particles ranging from 0.1 to 1μm have the minimum theoretical migration velocity, so that conventional ESPs have the worst performance for this fraction of particles. These particles are normally small in mass loading, however, very large in number, and most hazardous to human health [35-38,76]. An ESP has high performance for particles larger than several tens of micrometers, but experience severe rapping re-entrainment problems.

- ***Corona Quenching (Heavy Dust Loading)***

The effect of dust loading on the particle collection efficiency by an ESP has been experimentally analysed by Zukeran et al [39], where the collection efficiency of particles (based on particle number) with various diameters as a function of different dust loadings was studied. The results show that collection efficiency decreases with increasing dust loading greater than $4.5 \times 10^{10} \# pts/m^3$. Based on the theory developed by Pauthenier and Moreau-Hanot [73], the electric field in an ESP is a Poisson electric field determined by the space charge density in the inter-electrode space, its gap length and the corona current. Space charge density is a combination of free space charges and dust charges ($\rho_{total} = \rho_i + \rho_d$). For a dust loaded ESP system, the more dust charged, the higher dust charge density, so that the less free space charges, resulting in a smaller magnitude of corona current. As dust loading increases to a certain degree, the corona current becomes zero and leads to a severe collection performance violation. This phenomenon is corona quenching. Increase in dust loading so that ρ_d also produces an unusual electric field distribution in the region near the collecting electrode, readily triggering sparking.

- ***Back Corona***

Charged particles with high resistivity accumulate on the collecting electrode and act as an insulating layer. The electric field around the discharge electrode is not influenced greatly until the thickness of the insulating dust layer rises to a threshold where the voltage across the layer increases excessively large to cause breakdown to occur. Breakdown leads to generating electron avalanches, which trigger a new corona

discharge phenomenon from the collecting electrode to discharge electrode, and the particle charging process is then deteriorated. This is called back corona and represents one of the most complicated abnormal phenomena in ESP [77-80].

- ***Dust Reentrainment***

Particles deposited on the collecting electrode must be removed regularly to avoid back corona phenomena. A mechanical rapping system is commonly used in the conventional industrial ESPs. However, this rapping process would often disintegrate the dust layer, which would disperse into the gas stream to be treated repeatedly, and have a possibility to escape to the environment [81]. This performance-suppressing phenomenon is rapping re-entrainment.

The excessively high gas velocity, higher than 1-2m/s in industrial ESPs, and corona wind (particle elastic collision with gas molecules – electrohydrodynamically induced secondary flow) can also induce the dust re-entrainment problem.

Sproull [6] made extensive study of the rapping efficiency and re-entrainment research. Bassett, Akutsu and Masuda [81] did more detailed research of continuous reentrainment in a bench-scale precipitator for relatively large particles of various materials and for different polarities of applied corona voltage. Gooch and Marchant [82] reported the bulk of the experimental data and show the structure of the model for rapping re-entrainment. Plaks [83] proposed a precharger design, which can reduce the emission of the submicron and rapping reentrainment particle fractions, especially for high resistivity, by his ESP performance prediction model—ESPVI 4.0a. Zukeran et al. [84]

tested ESP performance with and without a humidifier, experimental results showed that re-entrainment is prevented by humidification that may result from an increase in the adhesive force between captured particles and the collection electrode due to the increase in humidity. However, re-entrainment is still a crucial problem encountered by most conventional industrial ESPs.

- ***Influence of Electrohydrodynamics (EHD) Force***

The ESP system under operation with particles and bulk of ions is far beyond a complicated situation, due to the interaction of neutral gas stream with ions and charged particles. The study of the general interaction between charged species and the neutral gas is Electrohydrodynamics (EHD) [6,85]. If considering ions only, the motion of the gas that results form the ion drag force is also so called "corona wind or electric wind".

The velocity of corona wind can be several meters per second, may far beyond the neutron particle effective migration velocity. It could make the mixing of particles and ions more even, so that it increase the chances for particle collision with ions to be charged, and the excessive high velocity can drive or push particles (charged and uncharged) migrating to the collection electrode. From this point of view, corona wind is positive for improving ESP performance. However, in the region near the collecting electrode, corona wind would form a strong vortex flow to bring more deposited particles back to the centre of discharging channel. This would prevent or even stop the dust collecting process. The pressure drop within discharge channel would also increase by this violent flow disturbance.

Yamamoto and Velkoff [85], Leonard et al. [86], and Okubo et al. [87] have numerically modeled the EHD flow without the effects of particulate space charge. Atten et al. [88] examined the EHD interaction of the charged particles with the gas and concluded that particles below about 5μm in diameter are strongly coupled to the gas that their motion is the primary cause of turbulence in the ESP. An EHD number (or Conductive Electric Rayleigh Number) is modified from the original classical EHD number by Yamamoto et al. [85] for evaluating the EHD effects in a specific ESP system, which can be expressed by [89],

$$Ehd = \frac{I_0 L^3}{\rho_f v_f^{\ 2} \mu_i A} \tag{2.27}$$

Another important dimensionless number is the Masuda number (or Dielectric Electric Rayleigh Number), expressed by [50],

$$Md = \frac{\varepsilon_0 E_0^{\ 2} L^2}{\rho_f v_f^{\ 2}} \tag{2.28}$$

The EHD induced secondary flow is not neglectable when the ratio of *Ehd* (or *Md*) and Re^2 is greater than unity for fluid flow [90].

2.4 GAS-SOLID TWO-PHASE FLOW AND THE SEPARATION

The analysis of a gas-solid two-phase flow system is of great complexity, due to the difficulties in assessing the dynamic responses of each phase and the interactions between the phases. In some special cases, the gas-solid mixture can be treated as a single

pseudo-homogeneous phase in which general thermodynamic properties of a gas-solid mixture can be defined. Analysis on the characteristics of each phase and their interaction is the prerequisite for the separation processes.

Similar with the gas-liquid two-phase flow, the gas-solid two-phase flow can be classified into various flow regimes based on the solid motion under different gas velocity, such as fixed bed, particulate fluidization, bubbling fluidization, slugging fluidization, fast fluidization, dilute transportation, etc. The flow regimes are characterized mostly on the dense-phase situation. Only if the gas velocity exceeds a certain amount of value, could the dilute flow appear. There are several criteria commonly employed to evaluate dense flow in contrast to dilute flow, such as, (1) mass flow ratio of solids to gas, [91]; (2) volumetric concentration of solids in the pipeline; (3) particle-particle interaction in comparison with the particle-fluid interaction, [92]; etc. The third one is more convenient for analysis on the gas-solid system with submicron and ultrafine size level particles phase. Consider a particle traveling a distance with τ_{rp} (particle relaxation time) before it stops, if this distance is greater than the particle-particle collision distance, we can consider the system as dilute. A dimensionless factor, called the two-phase interaction number ($\sum_{2\phi}$), for evaluating phase interaction is derived by Chang [89], expressed as follows:

$$\sum_{2\phi} = \frac{N_t K L}{\rho_f U_0} \tag{2.29}$$

where N_i is the particle (neutral particles, charged particles, ions, electrons, etc.) number density; L is the characteristic length of the fluid channel; ρ is the gas density at the entrance; U_0 is the gas velocity at the entrance; K refers to the gas-solid interfacial drag number, defined as $K = 3\pi\mu_g$. By comparing the particle-fluid drag effect with the gas phase continuity, the degree of the gas-solid two-phase dilution can be determined. When $\sum_{2\phi} \ll 1$, the gas-solid can be treated as a single pseudo-homogeneous phase system.

The existing gas-solid separation mechanisms mostly depend on the principles of centrifugation, electrostatic effects, filtration, gravitational settling, and wet scrubbing. Separations applying these principles are rotary flow dust separators, electrostatic precipitators, filters, settling chambers and scrubbers. Each of the mechanisms is briefly discussed in Chapter 1 (except the electrostatic precipitator, discussed in section 2.3).

CHAPTER 3

EXPERIMENTAL FACILITIES

The natural gas combustion test loop has been constructed to investigate the DFS-ESP. The test loop consists of a natural gas combustor, DFS-ESP section, exhaust section, and sampling points. The experimental instrumentation consists of the following:

- Condensation nucleation particle counter (CNPC) for measuring the particle number density;
- Optical particle counter (OPC) for measuring the particle mass density;
- Flow rate measurement;
- Thermocouples;
- Pressure drop cell;

In addition, it is possible to insert carbon tape samples to capture dust particles for ESEM (Environmental Scanning Electron Microscope) analysis.

3.1 DUST FLOW SEPARATOR TYPE ELECTROSTATIC PRECIPITATOR

Schematic configuration of the dust flow separator type electrostatic precipitator (DFS-ESP) used in this experiment is shown in Figure 3.1. The basic structure of the DFS-ESP consists of several section of Pyrex glass sleeve tubes (O.D. 90mm, I.D. 76mm and 254mm long), with a Stainless Steel pipe (I.D. 63.5mm and 760mm long) in the main branch as the flow separator, and an Aluminium pipe (I.D. 63.5mm and 430mm long) in the ESP branch as the collection electrode of the wire-pipe ESP.

Figure 3.2 shows the schematic of the experiment loop. There are three sampling ports, MP1, MP2, and MP3, representing upstream of, downstream of, and middle of the main branch of DFS-ESP, for the purpose of particulate matter sampling, pressure and temperature monitoring, and flow profile detection in the main branch and ESP branch under different test conditions. There is a small heat exchanger located directly before the particle sampling instruments, which could eliminate most of the condensate in the sample stream, and cool down the temperature of sample stream, for the reason to ensure the CNPC and OPC instruments are working properly.

The optional heat exchanger is placed at upstream of DFS-ESP, for the purpose of temperature control; and an optional hot air line is injected at the inlet of DFS-ESP, for the purpose of dilution.

Figure 3.3 is a photograph of DFS-ESP and shows the laboratory layout.

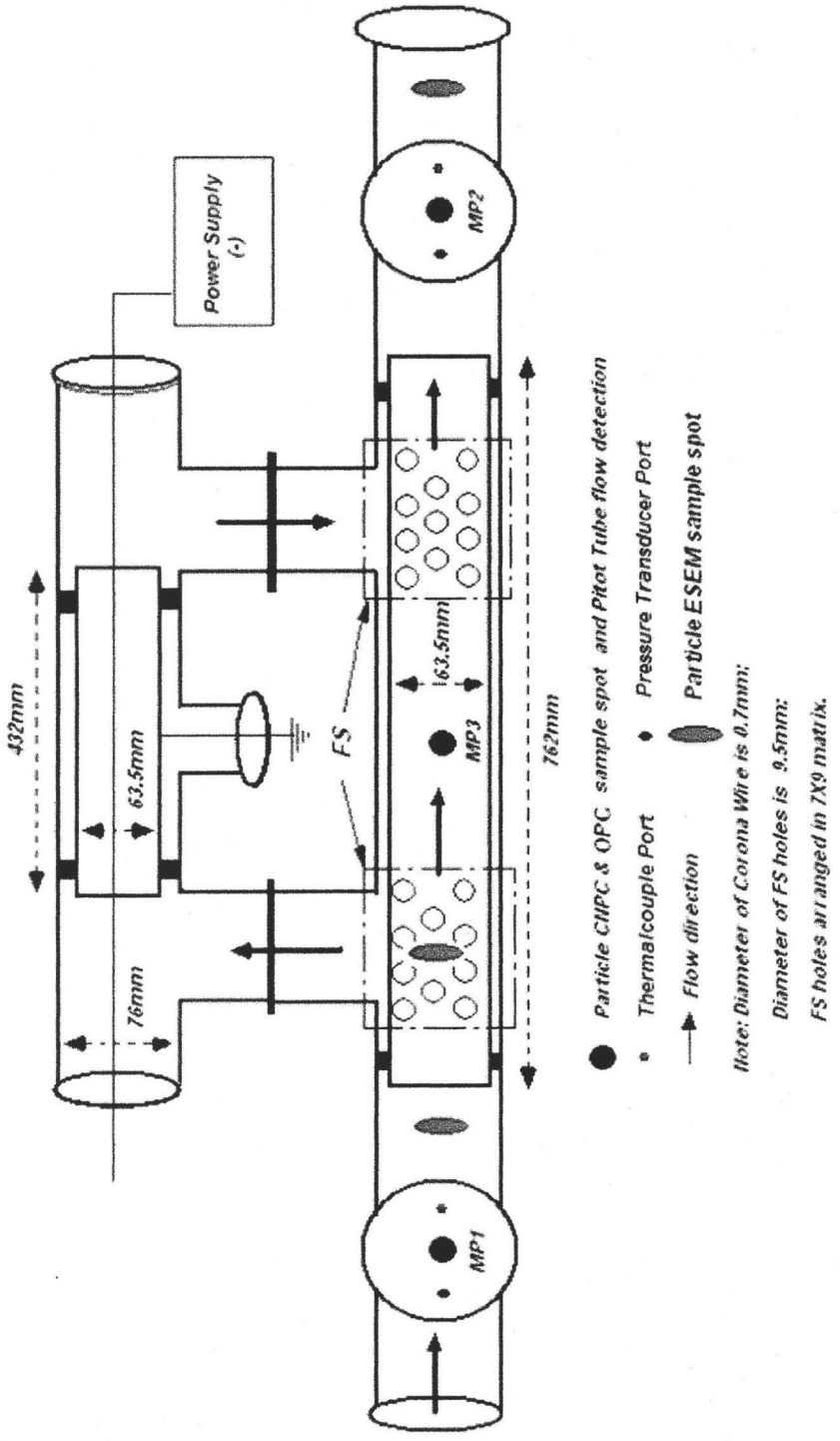

Figure 3.1 Schematic of DFS-ESP

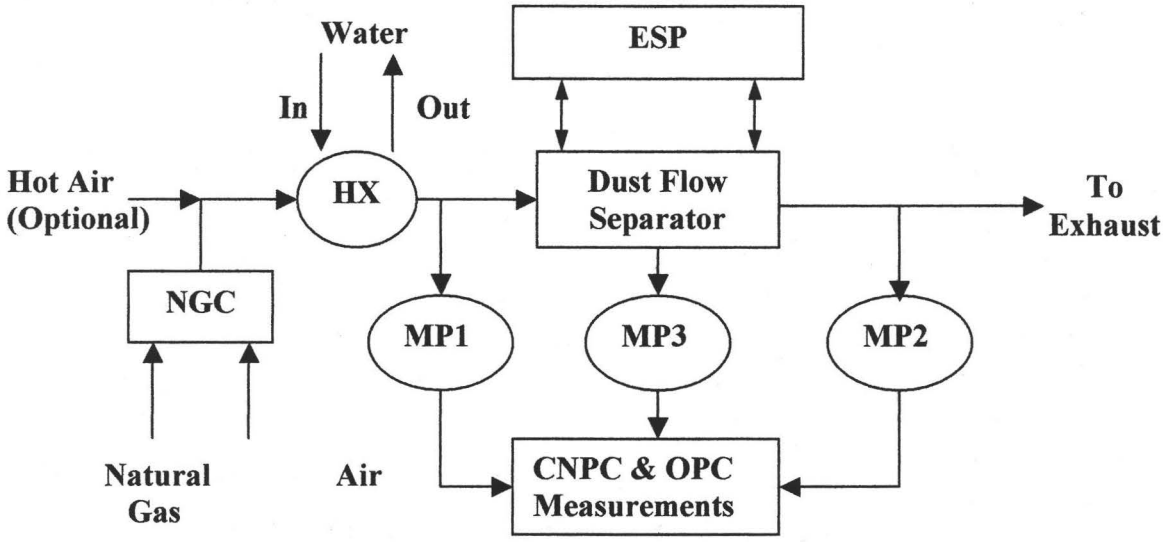

LEGEND

CNPC & OPC	Condensation Nucleation Particle Counter - TSI Optical Particle Counter – HazDust III		
NGC	Natural Gas Combustor	ESP	Electrostatic Precipitator
MP	Measuring Points 1, 2 & 3 PM, Temperature, Pressure	HX	Heat Exchanger

Figure 3.2 Schematic of experimental loop

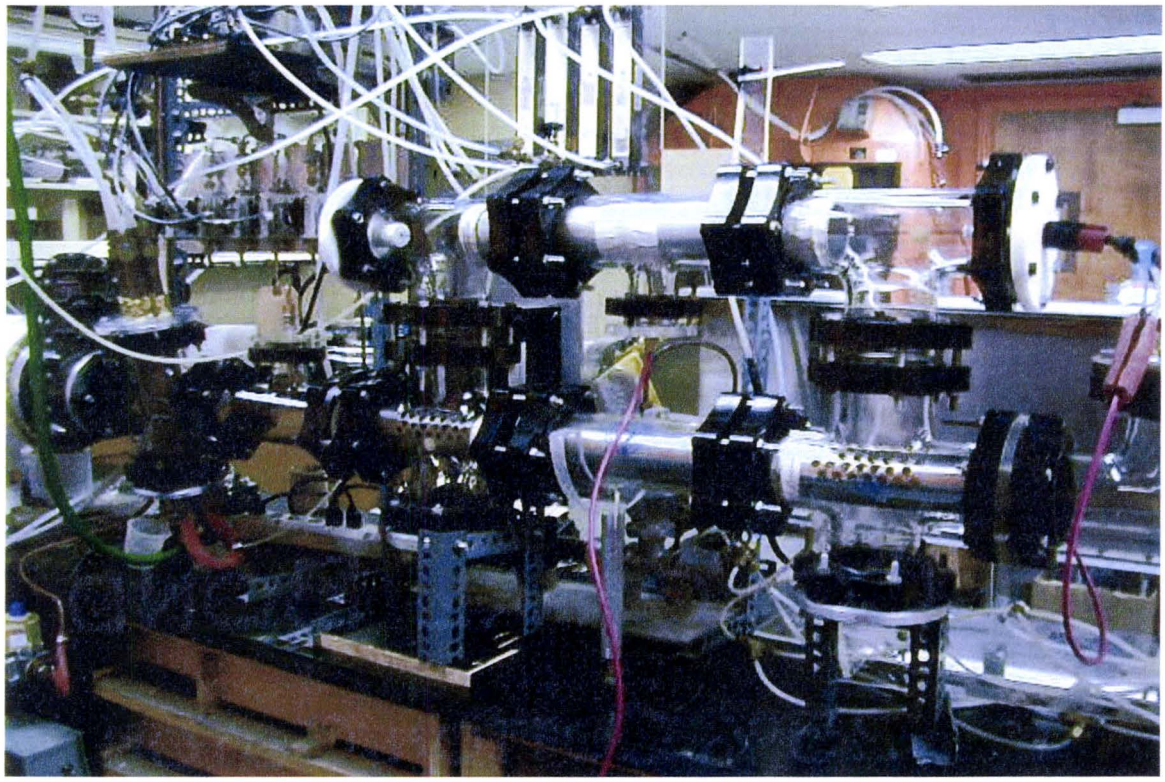

Figure 3.3 Photograph of the experimental DFS-ESP

3.1.1 Characterization of Particles

Characterization of particles emitted from natural gas combustion is conducted. Particulate matters created during natural gas combustion have been sampled from various locations (MP1, MP2 and MP3) within the loop and characterized by using Environmental Scanning Electron Microscopy (ESEM) and Condensation Nucleation Particle Counter-Particle Size Selectors (CNPC-PSS). Measurement locations for particle size sampling are shown in Figure 3.4.

- ***ESEM Method***

A square piece of glass slide held by Teflon support was positioned in the centre of the flow channel both upstream (MP1) and downstream (MP2) perpendicular to the flow. Deposited particles were removed from the glass slices using a sticky carbon tape to be further analyzed by ESEM. Another location for particle characteristic analysis was chose at the inner walls of the flow separator. The particles were sampled for about 5 minutes at a relatively stable temperature to avoiding particle stack up or agglomeration, which would bias the accuracy of particle size and concentration analysis. Images taken by ESEM were analyzed by HLImage++ 98 software.

By removing deposited/collected PM with carbon tape, it was difficult to obtain a sample that has enough number of separate particles. Since the images showed mainly agglomerates of PM, an additional filtering of images ("sobel" edge detector filter in this case) in combination with the "blob" function from HLImage++98 software was used to clarify separate particles from agglomerates.

- ***CNPC-PSS Method***

CNPC-PSS was used to determine the PM number density and size distribution. The particles of size in diameter ranging from 17 to 160nm were obtained by inserting various number of particle size selection screens (1 to 15). Samples were taken from MP1, MP2 and the center location of the main stream (MP3). Experiments were performed with and without two specially designed inserts (Figure 3.5), symmetrically placed at both upstream and downstream of the flow separation section with various high voltages applied to the ESP as indicated in the Figure 3.4.

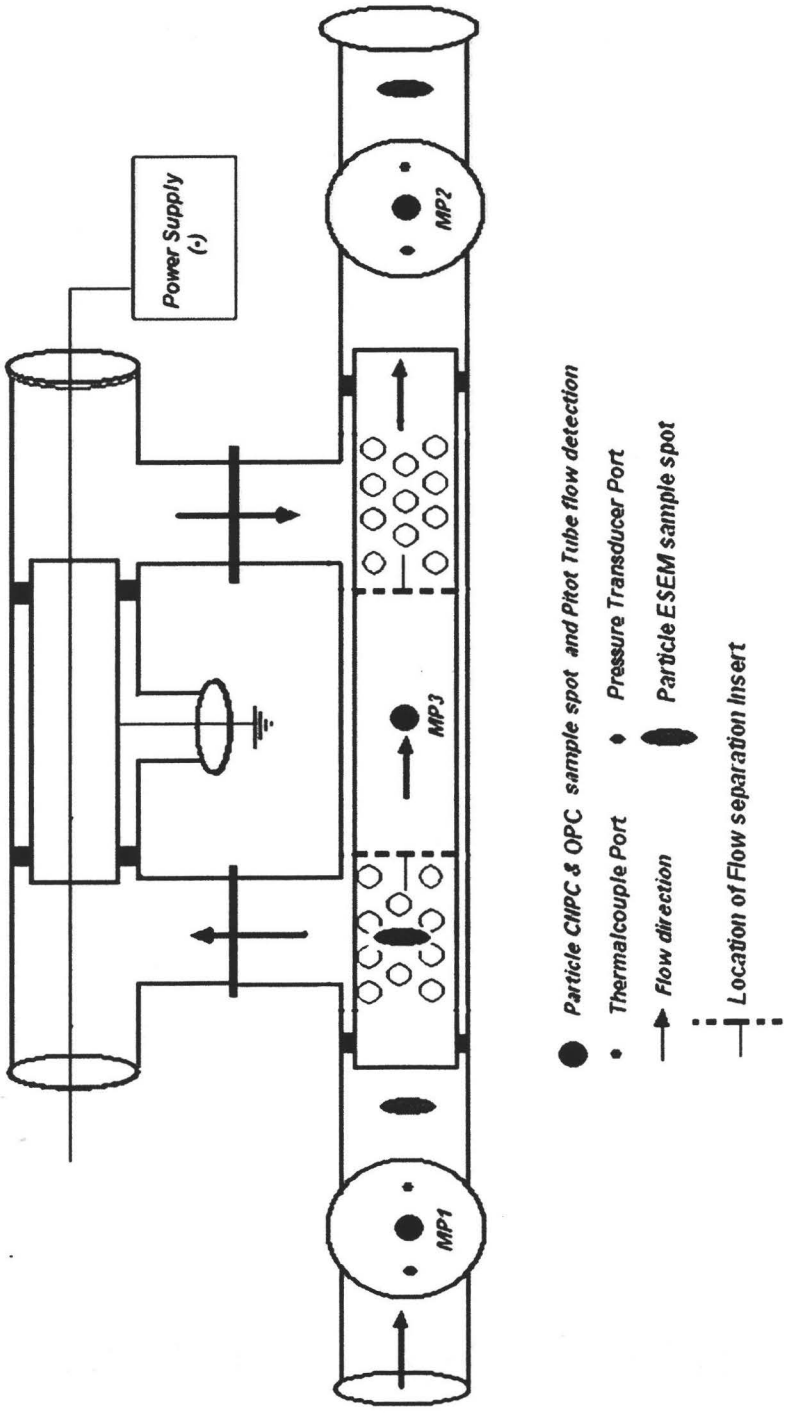

Figure 3.4 Measurement locations for particle size sampling

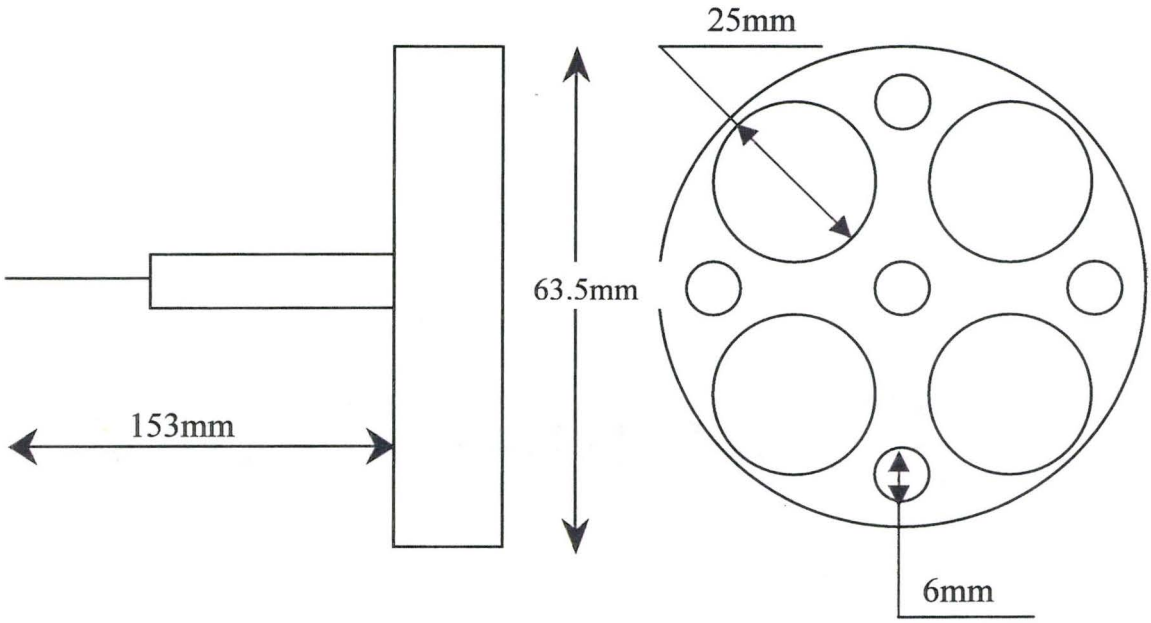

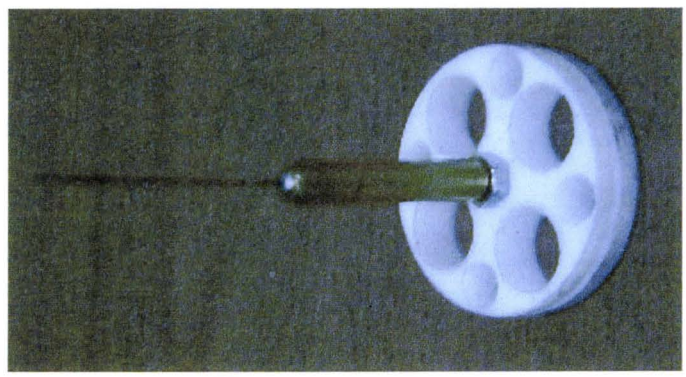

Figure 3.5 Schematics and photograph of flow separator insert

3.1.2 Experiment on Characteristic of the Dust Flow Separator

The dust flow separator is designed to achieve separating most of the fine particles from exhaust flow to ESP branch, while maintaining most of the gas flow in the main stream, for the purpose of improving ESP working efficiency. Therefore, characteristics of the dust flow separator were conducted by local flow profile and particle separation efficiency measurements.

The schematics and a photograph of the dust flow separator are shown in Figures 3.6 and 3.7.

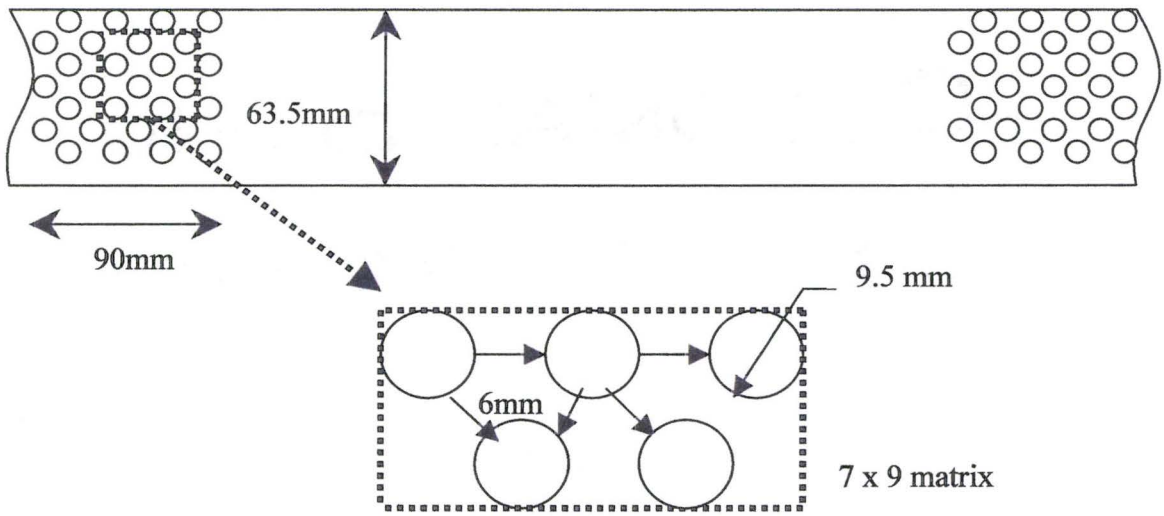

Figure 3.6 Schematics of dust flow separator

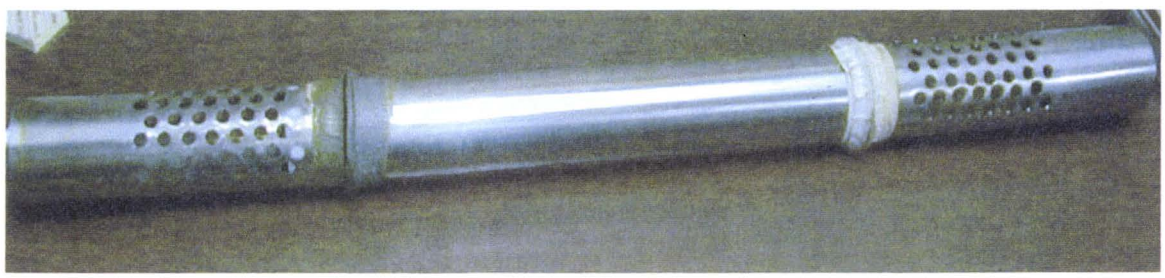

Figure 3.7 Photograph of dust flow separator

- ***Flow Profile Measurement***

A Pitot tube is used for the local flow profile measurement at MP1, MP2 and MP3, as shown in Figure 3.8.

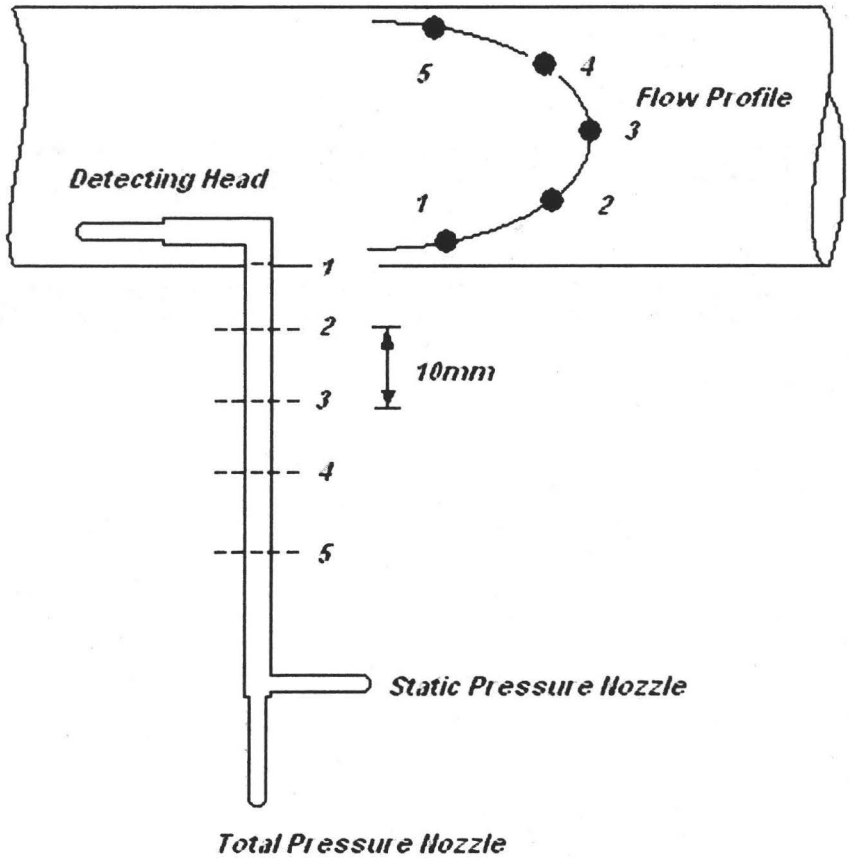

Figure 3.8 Schematics of Pitot tube experiment where #3 located at the center of tube

Total flow rates employed in the experiments are 5, 7 and 8.5 Nm^3/h, so that the corresponding Reynolds number at sampling ports range approximately from 1640~3110. This means that the flows within the experiment system range from laminar to transition flow. By examining the flow velocities at 1~5 notated in Figure 3.8, the flow profile can

be determined. Furthermore, the flow rate at the main stream and the branch stream can also be determined. To achieve this goal, the pitot tube is marked for 5 locations; each one represents one specific flow velocity examining location on the profile. The distance from one to another is around 10mm. The arrangement of these marks and their relationship with flow profile is as indicated in Figure 3.8.

- ***Particle Separation Measurement***

Particle separation diagnosis is performed by measuring the number of particle densities at MP1, MP2, and MP3 by using CNPC, and partial separation efficiency for specific particle size range is detected by using CNPC-PSS. Isokinetic sampling methodology is taken into consider in this application. The schematic of experimental set-up is the same as in Figure 3.4.

3.1.3 Characterization of the ESP

In this experiment, the dimensions of the ESP are optimized for the existing experiment loop by MESP modeling. A detailed schematic of the wire-pipe ESP is shown in Figure 3.9. An aluminium pipe with 63.5mm diameter and 432mm length is horizontally placed as a collecting electrode, while the corona wire with 0.7mm diameter is the discharge electrode. Another wire with 0.23mm diameter was also tested to mainly analyze the EHD effect on the particle collection efficiency. The discharge electrode is connected to a negative dc high-voltage power supply, while the collecting electrode is grounded. Two pieces Teflon flanges are coupled on both ends of the ESP as the system

closure heads and insulators. Several specially designed screws and nuts are symmetrically arranged to help center and fix the corona wire on the Teflon flanges.

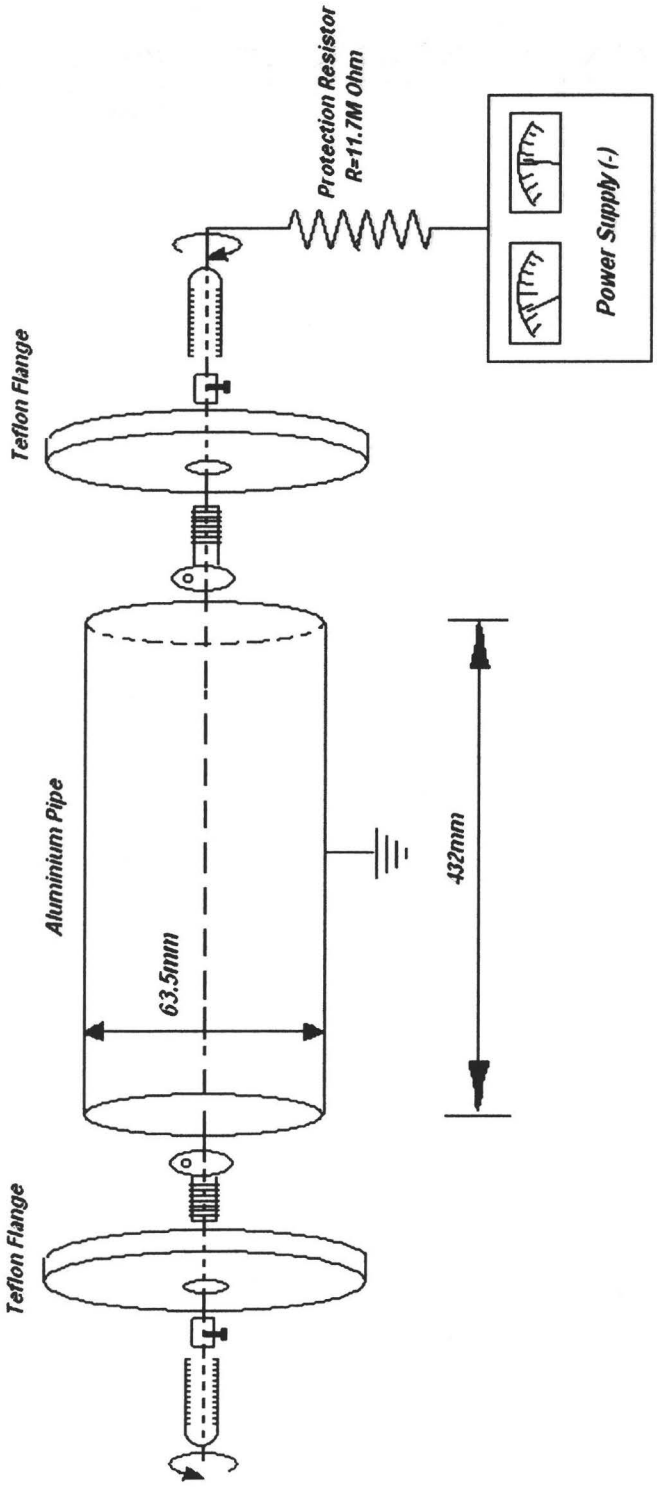

Figure 3.9 Schematic of the electrostatic precipitator

3.1.4 Isokinetic Sampling

The particle collection efficiency is examined by both CNPC and OPC methods for determination of the number and mass concentration, respectively. During this process, an essential element is the ability to collect representative samples for analysis, which must reflect the particle concentration accurately. For this purpose, the methodology of isokinetic sampling is taken into concern. *Isokinetic sampling* is a procedure to ensure that a representative sample of aerosol enters the inlet of a sampling tube when sampling from a moving aerosol stream. Sampling is isokinetic when the inlet of the sampler is aligned parallel to the gas streamlines and the gas velocity entering the probe is identical to the free stream velocity approaching the inlet. [6] This way, there is no distortion of the streamlines in the neighbourhood of the inlet, and there is no particle loss at the inlet regardless of particle size or inertia, as shown in Figure 3.10.

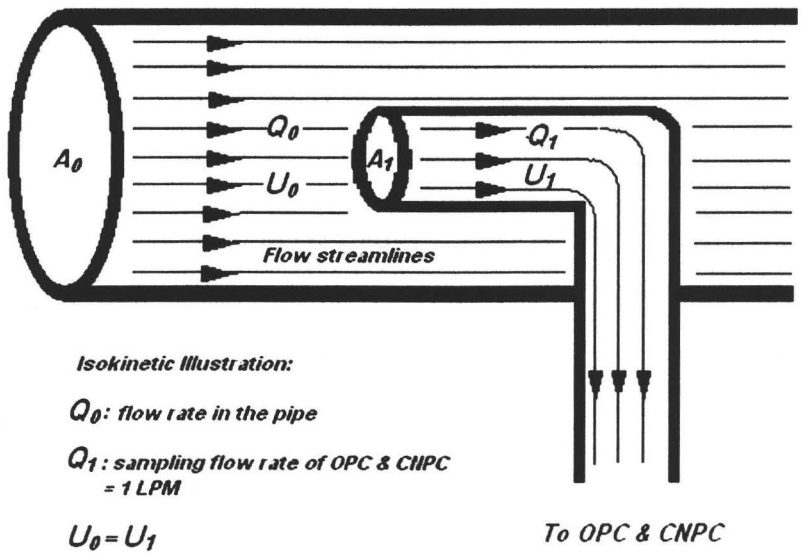

Figure 3.10 Illustration of isokinetic sampling

In this case, Q_0 is the flow rate at examining spots (MP1 or MP2) under the experiment conditions of high temperature corresponding to various inlet flow rates under standard conditions (20°C & 1atm), Q_1 is the sampling flow rate of CNPC and OPC that equals to 1 LPM according to the devices' setting, and U_0 and U_1 are the flow velocities in the pipe and sampling probe respectively, which can be determined by the ratios of the flow rates and their respective cross-sectional areas. The isokinetic condition for a properly aligned probe is:

$$U_0 = U_1 \tag{3.1}$$

To meet this condition, the flow rates in the duct and sampling probe have to be proportional to their cross-section areas, from which, the unknown diameter of sampling probe can be determined by:

$$d_1 = \sqrt{\frac{Q_1}{Q_0}} \cdot d_0 \tag{3.2}$$

where d_0 and d_1 are representing the diameters of the pipe and sampling probe, separately. The corrected flows for different test temperature and their corresponding sampling probe sizes are listed in detail in table of Appendix C as reference.

3.2 NATURAL GAS COMBUSTION SYSTEM

A natural gas combustor, using a Bunsen burner with air feeding from the bottom, is placed at the upstream of the experimental loop to generate submicron and ultrafine particulate matter. Natural gas feeding is approximately 0.45~0.75Nm^3/h. Air feeding for

all experiments ranges in 5~8.5Nm^3/h. Therefore, the air-to-fuel ratio is in between the range of flammability.

3.3 INSTRUMENTATION

Important parameters monitored during experiments include:

- ESP corona current and voltage;
- Flow rate;
- Temperature;
- Pressure drop

3.3.1 Current Measurement

Time-averaged corona current is measured by the electrometer, (Keithley Model 600B). The technical specification is as below:

- Range: 10^{-14} A – full scale to 0.3A in twenty eight 1x and 3x ranges.
- Accuracy: $\pm 2\%$ of full scale on 0.3 to 10^{-11}A ranges using the smallest available multiplier switch setting; $\pm 4\%$ of full scale on $3x10^{-12}$ to 10^{-14} A ranges.
- Meter noise: less than $\pm 3x10^{-15}$A.

3.3.2 Flow Rate Measurement

Flow rates of feeding air, total flue gas, and mainstream gas are monitored by two types of flow meter: rotameter (Dakota Instruments.) and pitot tube (type PA).

- *Rotameter*

A rotameter is based on the drag effect. The mass flux can be obtained by

$$\dot{m} = A\sqrt{\rho(\rho \cdot u^2)} \tag{3.3}$$

where A is the cross-section area; u is the gas velocity, which is a function of the drag coefficient; and $\rho = \sqrt{(\rho_{float} - \rho_{fluid}) \cdot \rho_{fluid}}$, where ρ_{float} and ρ_{fluid} are the densities of the float and fluid monitored respectively.

Equation 3.3 is based on air calibration at standard conditions, which is 14.7psi (1atm) pressure and 70 deg F (21.1 deg C) temperature. Certain correction factors should be taken into account to provide precise flow rate. These correction factors include:

- Pressure factor (f_1): $f_1 = [14.7/(14.7+P)]^{1/2}$

, where P is the pressure indicated on the pressure gauge on the rotameter.

- Temperature factor (f_2): $f_2 = [(273+T)/273]^{1/2}$

, where, T is the temperature at the location where flow rate is investigated.

- Specific gravity factor (f_3): $f_3=1$

So that, the real flow rate at specific spot should be corrected as the equation below:

$$Q = Q_{indicated}/(f_1 \cdot f_2 \cdot f_3) \tag{3.4}$$

Furthermore, the declared instrument standard error of 5%, a reasonable reading error and an inlet gas pressure variation during the experiment are also considered.

- *Pitot tube*

For precise measurement of flow rate at the mainstream, a Pitot tube can be used. It measures total and static pressures at the same point in a moving fluid. From the

Bernoulli equation, $P+\frac{1}{2}\rho \cdot u^2 = P_0 \equiv total\ pressure$. Therefore, velocity can be obtained as following:

$$u = [2(P_0 - P)/\rho]^{1/2} \tag{3.5}$$

where velocity can be determined from the pressure difference, from which the flow rate could be obtained from integrating velocity radial profiles.

The shape of the probe measuring tip determines the sensitivity of the pitot-static probe to flow angularity (yaw and pitch angle error) caused by flow not parallel to the head, which is the large of error in this type of instrument. According to the manufacture [93], the Prandtl type Pitot tube can compensate the errors in total and static pressure, so the probe yields velocity and weight flow readings accurate up to 2% for an angle of attack less than 30°. Besides, the length of the head governs sensitivity to Mach number errors: the longer the head, the more accurate the reading over a wide flow range. Based on above consideration, the modified Prandtl type with a head of 14 probe diameters long Pitot tube is used.

In the experiment, the Pitot tube is calibrated by a manometer.

3.3.3 Temperature Measurement

T type—Copper versus Copper-Nickel alloy thermocouple is used for temperature measurement, ranging from about 370°C down to –249°C.

The working principle of thermocouple is based on the wires of different materials joined and subjected to a temperature gradient, generating a net electromotive

force (EMF). The net EMF is the sum of the EMF's generated in each individual wire, and only those portions of the wires experiencing a temperature gradient affect the EMF.

The output of thermoelectric voltage is shown on an Analog/Digital multimeter, according to the ITS-90 [94], corresponding temperature can be determined. The multimeter used is Fluke 89 series IV, with 0.025% basic dc accuracy and 50,000-count resolution.

ASTM standard E230-87 in the 1992 Annual Book of ASTM Standards [95] specifies that the initial calibration tolerances for type T commercial thermocouples be $\pm 1^{\circ}C$ or $\pm 0.75\%$ of reading (whichever is greater) between $0^{\circ}C$ and $350^{\circ}C$.

3.3.4 Pressure Drop Measurement

Pressure drop across the DFS-ESP is measured by the differential pressure transducer (Validyne DP15TL) with accuracy of $\pm 0.1\%$ of full-scale reading.

Process pressure is transmitted through isolating diaphragms to a sensing diaphragm in the center of the cell. The sensing diaphragm deflects in response to the differential pressure across it. The position of the sensing diaphragm is detected by capacitor plates and the differential capacitance between these plates is converted electronically to an electric current output signal. The maximum frequency response is about 100Hz, for the sake of which, they are not well suited for rapid transient. The transducer can be adapted to many different pressure ranges by changing the thickness of the isolating diaphragm, in this case, the diaphragm ranging of 0 to 3.5kPa is chosen, which means it is optimized for pressure differences of up to 3.5kPa.

3.4 PARTICULATE MATTER SAMPLING AND ANALYSIS

The number and mass density of particulate matter are some of the key parameters being monitored during the entire experiment process, which are performed by condensation nucleation particle counter (CNPC) and optical particle counter (OPC), respectively.

In addition, for the purpose to study the size and shape of generated aerosol particles, environment scanning electron microscopy (ESEM) is used.

3.4.1 Optical Particle Counter (OPC)

Optical particle counter (OPC) is utilized for mass particle density measurement. Its working principle is based on one of the particles' optical effects—scattering of light. The smallest sensitive particle ranges from 0.1 to 25 μm, for which the Mie scattering is applicable, where the particle diameter (d) is equal to the incident light wavelength (λ).

It is the change in scattered light intensity that is obtained and transferred to a digital signal for particle density measurements. Based on the previous research [24]-[28], the scattered light intensity is a function of the wavelength of incident radiation, the refractive index and the size of the particles, and the scattering angle with respect to the incident beam. Utilizing these factors, some designs of these instruments are a unique feature of the size distribution detection.

There are three major sections in an OPC (i) the airflow system, (ii) the optical system, and (iii) the electronics system. A laser illuminated optical system allows single particle sampling by collecting the scattered light from each particle with a solid-state

detector. Electronics provides amplification of the low level signals received from the photodetector and converts each scattered light pulse to a corresponding size category (depending on the pulse height), which is then accumulated in a data logger. Each scattered pulse corresponds to a particle count, and this is incremented in the appropriate size category to obtain particle concentration in a given size interval. In this study OPC system (HazDust model III) is used for the fine aerosol particle collection efficiency investigation.

The HAZ-DUST III real-time personal dust monitor uses the principle of near-forward light scattering of infrared radiation to immediately and continuously measure the concentration in mg/m^3 of airborne dust particles. HAZ-DUST III displays and records respirable, thoracic, or inhalable particulate mass using an internal microprocessor and interchangeable sampling heads. The near-forward light scattering principle utilizes an infrared light source positioned at a 90-degree angle from a photodetector. As the airborne particles enter the infrared beam, they scatter the light. The amount of light received by the photodetector is directly proportional to the aerosol concentration. Unique signal processing internally compensates for noise and drift. It contains an internal pulsation dampened pump, data logger, and communications software. The optional HazComm computer software provides data plots for detailed graphical analysis and allows statistical analysis and mathematical correction of particle characteristics (density and refractive index) when aerosol is significantly different from calibration dust. The data easily imports into spreadsheet programs or saves to disk.

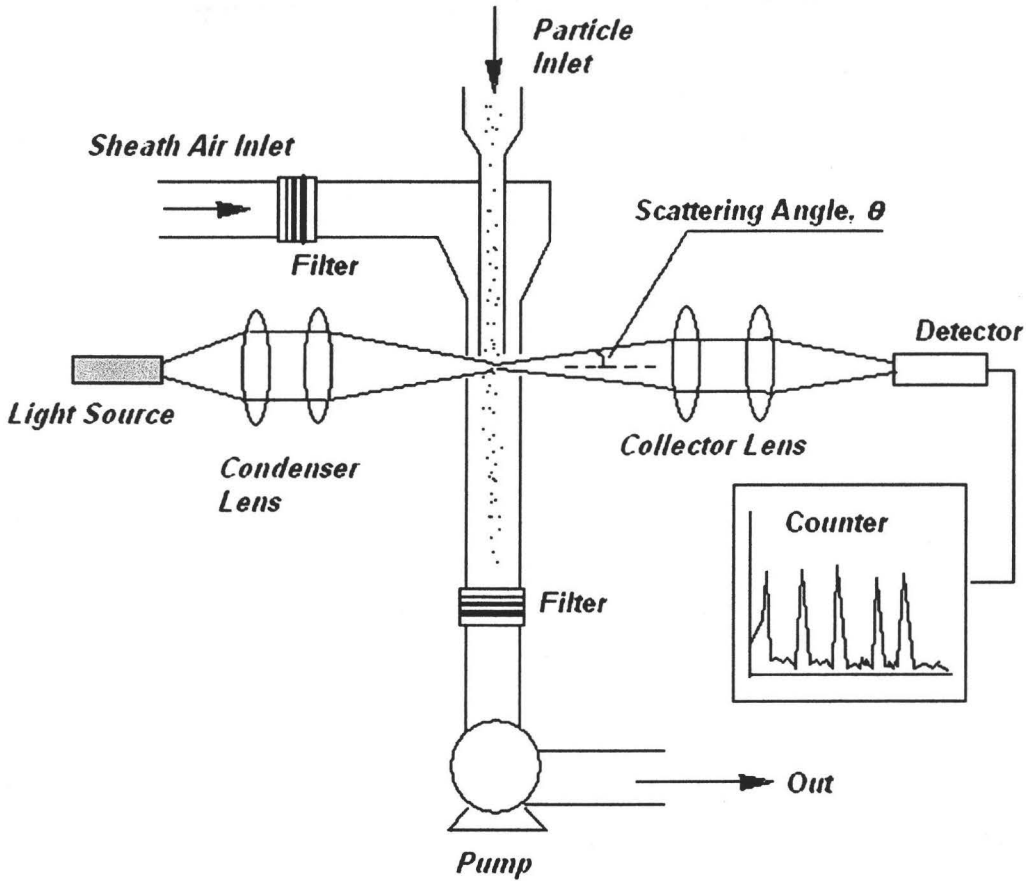

Figure 3.11 Schematic of an Optical Particle Counter

(Modified from the OPC by Hinds [6])

3.4.2 Condensation Nucleation Particle Counter (CNPC)

Condensation nucleation particle counter (CNPC) (model 3010 made by TSI Inc.), is employed to count particle number density at upstream and downstream of the DFS-ESP system for different experiment conditions. The characteristics of this device are shown in Table 3.1.

The schematic of a CNPC is shown in Figure 3.12. The operating principle of CNPC is similar with OPC. Sizes of the particles captured into CNPC are enlarged by a condensating vapour—Butonel to form easily detected size droplets [96]. As soon as the vapour surrounding particles reaches a certain degree of supersaturation, the vapour begins to condense onto the particles. When supersaturation is high enough, condensation would take place even if there is no particle existing. Molecules of the vapour form clusters due to natural motion of the gas and attractive Van der Waals forces to form nucleation sites.

CNPC contains a microprocessor to control all the functions, which utilizes built-in analog to digital convertors to monitor temperatures, voltages, and pressure drop of the CNPC. A counter is built into the microprocessor, and it tracks particle pulses detected by the photo detector. There are also several particle selectors used by CNPC to determine the size of particles working based on the dynamic momentum principle. The particle selector is actually a metal net, several selectors (with the same dimension of holes) piled up together correspond to a mechanical resistance, so that the particles with greater momentum can penetrate and be counted.

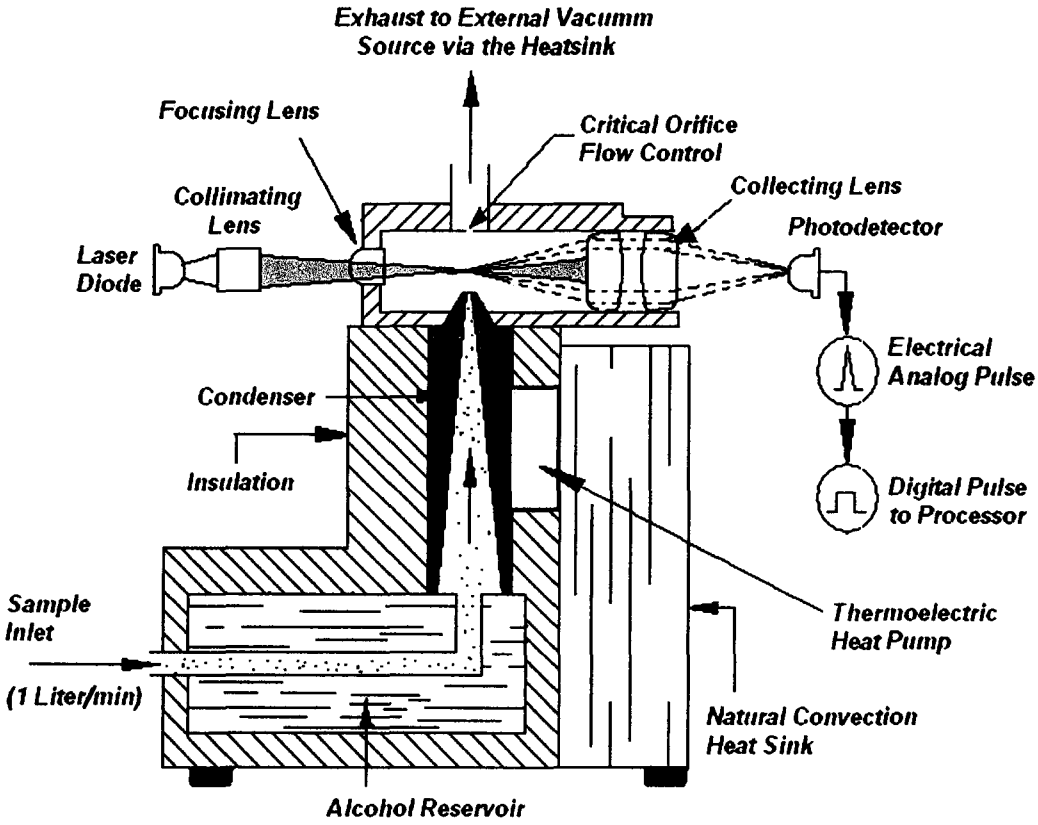

Figure 3.12 The schematic of CNPC, Model 3010, TSI Inc.
(Modified from TSI specification)

Table 3.1 Characteristic of CNPC Model 3010

Model	*3010*
Particle size Range [nm]	*≥ 10*
Sample flow rate [L/min]	*1.0*
Upper concentration limit [pt/cm^3]	*10^5*
False background count [pt/cm^3]	*<0.0001*
Time response [sec to 95% in high flow mode]	*<5*
Temperature [°C]	*10~35*
Humidity	*0~90%RH*
Vacuum source	*External*

3.4.3 Environmental Scanning Electron Microscope (ESEM)

ESEM is applied in the particle shape and size distribution analysis throughout the experiment. It is a special type of scanning electron microscope (SEM) developed in 1980s. There are two significant improvements within ESEM comparing SEM:

- It is not necessary to make nonconductive samples conductive in ESEM, i.e., working under its "wet" mode. Hence materials don't need to be coated by gold-palladium as do in SEM, so that the original characteristics of samples may not be destroyed, and it is possible to examine specimens in their natural state.
- ESEM can be operated under poor vacuum environment, while SEM would not work without a good vacuum. Water vapor, as one of the imaging gases in ESEM, can be added as much as 1.3kPa to the specimen chamber.

The environment in an ESEM can be selected from among water vapor, air, N_2, Ar, O_2, and etc based on the sample material. Dynamic characterization of wetting, drying, absorption, melting, corrosion, and crystallization can be performed using ESEM by choosing the correct environment for the sample [97].

ESEM model 2020 is used in the present work. The smallest particles at nanometer range can be detected at specific ESEM operating environment. Accelerating voltage ranges from 0 to 30keV in 100-volt steps. The working distance of sample to detector is from 2.6 to 50mm.

CHAPTER 4

EXPERIMENTAL RESULTS

4.1 FUNDAMENTAL CHARACTERISTIC OF COMBUSTION TEST LOOP

Particle characteristics from a natural gas combustor are measured by methods as described in Chapter 3.

ESEM images of deposited particles sampled from upstream (MP1), downstream (MP2) of DFS-ESP, and the upstream flow separator wall, and their corresponding size distribution analysis are shown in Figures 4.1 to 4.6. The ESEM images indicated that the majority of the deposited fine particles are agglomerated structures of the near spherical shape. The size distribution determined by ESEM image analysis shows that particles sampled from three different locations have the same distribution trends and particle sizes range mostly from 50 to 100nm. The mean particle diameter is estimated approximately 84nm, 96nm, and 85nm for locations MP1, MP2 and the upstream flow separator wall respectively. The details of this procedure have been described in [98], and an alternate procedure using reversed indices has been shown by Fuchs [15].

Particle size distributions at different locations sampled and analyzed by CNPC-PSS method are shown in Figures 4.7 and 4.8. The size distribution determined by CNPC-PSS method has a bimodal distribution with peaks for particle groups in the range from 17 to 41nm and 132 to 162nm in diameter, at MP1; and the size distribution at MP3 shows a similar bimodal distribution with the peaks for particle groups in the range from

41 to 72nm and greater than 162nm. The total particle number density varies with the combustion situation (sufficient combustion/ insufficient combustion), approximately ranging from 5×10^{8} #particles/m^3 to 5×10^{9} #particles/m^3, taking into account changes in inlet air flow rate, exhaust temperature, and pressure drop across the system. Figure 4.9 shows the change of particle number density with inlet air flow rate at MP1.

Characteristic numbers of particles from natural gas combustion loop analyzed by ESEM and CNPC methods are compared and summarized in Table 4.1.

Table 4.1 Particle environment for natural gas combustion exhaust tube

	d_{ave} [μm]	D_p [m^2/s]	Kn	Sc	Re_t	$ScRe_t$	$\sum_{2\phi}$
ESEM	0.05~0.3	$9X10^{-9}$	0.2~1.3	10^3~$4X10^4$	$3X10^3$	1.5E+7	10^{-4}
CNPC	0.017~0.16	$9X10^{-9}$	0.4~4	10^3~$4X10^4$	$3X10^3$	5.2E+6	10^{-4}

Note: Re_t is the Reynolds number inside tube

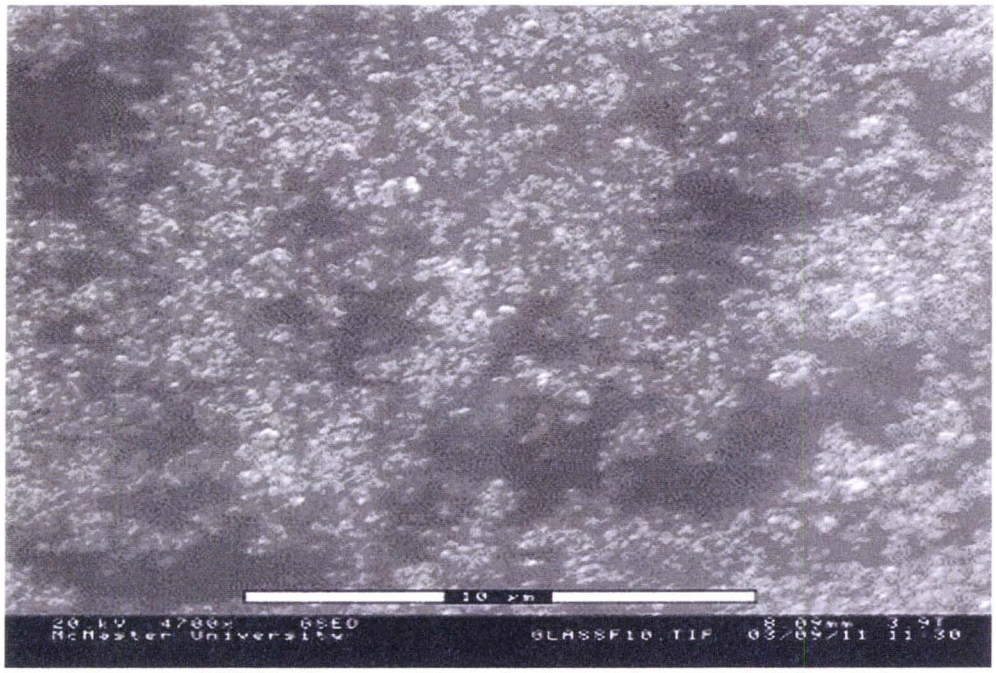

Figure 4.1 Typical ESEM image of deposited particles sampled from tube center at MP1 (upstream of DFS-ESP)

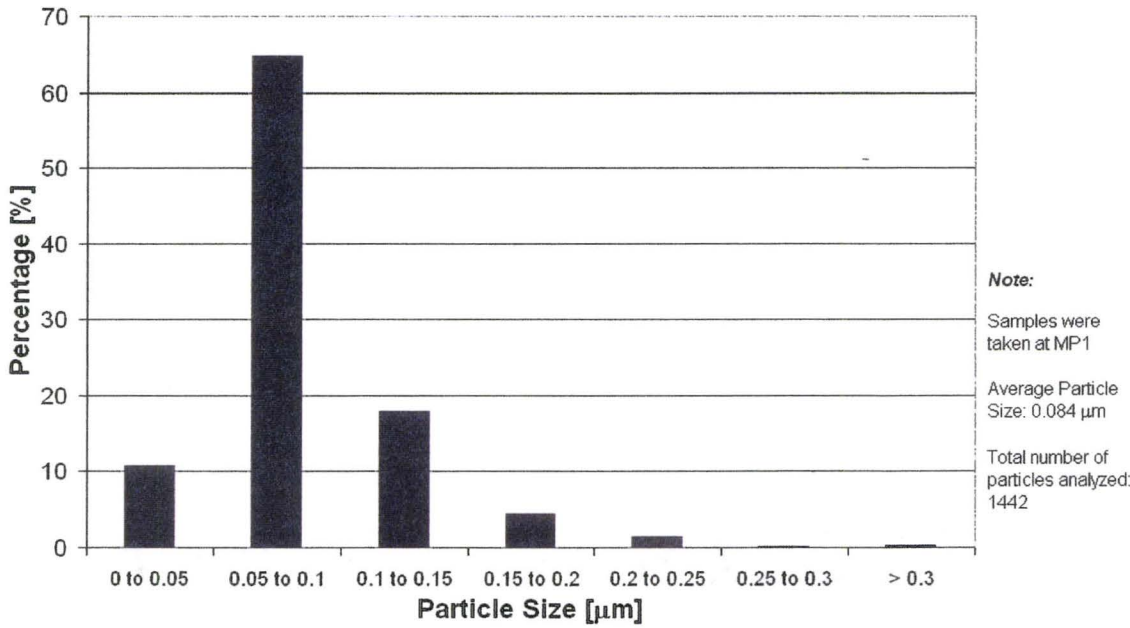

Figure 4.2 Size distribution analysis of deposited particles sampled from tube center at MP1 (upstream of DFS-ESP) for Q=7Nm^3/h, T=160°C, and sampling time=5 minutes

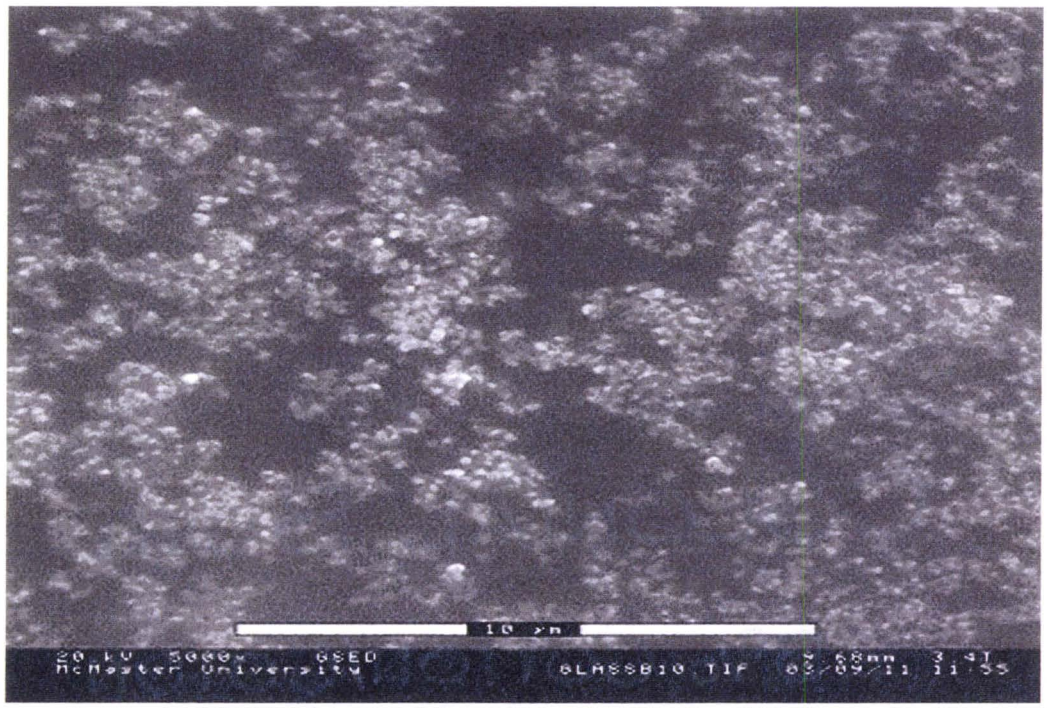

Figure 4.3 Typical ESEM image of deposited particles sampled from tube center at MP2 (downstream of DFS-ESP)

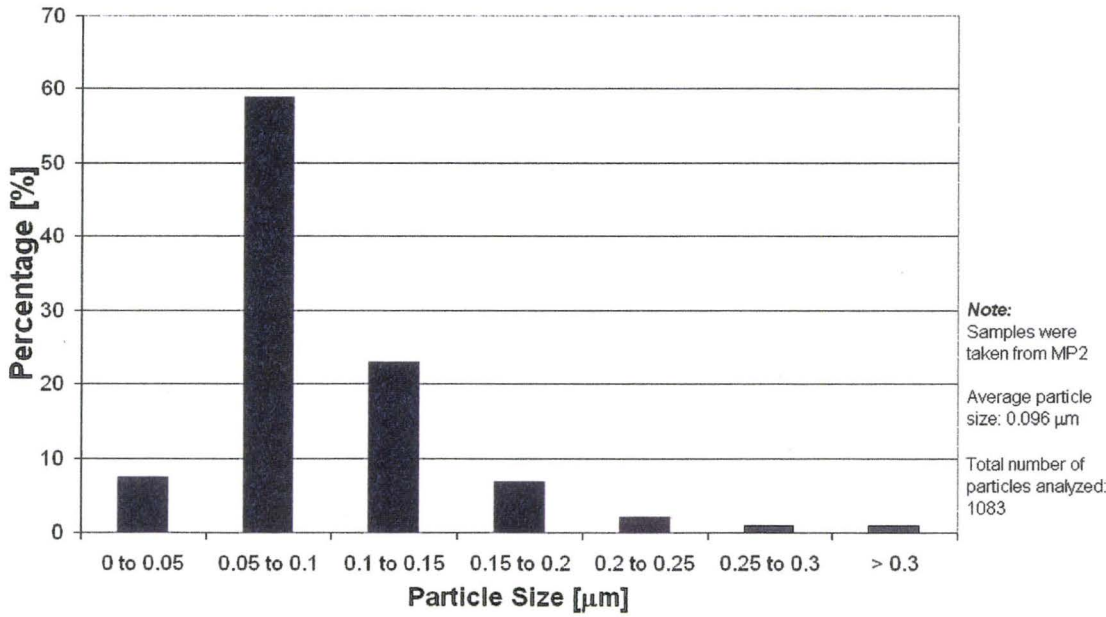

Figure 4.4 Size distribution analysis of deposited particles sampled from tube center at MP2 (downstream of DFS-ESP) for Q=7Nm^3/h, T=100°C, and sampling time=5 minutes

Figure 4.5 Typical ESEM image of deposited particles sampled at tube walls of upstream flow separator (MP1)

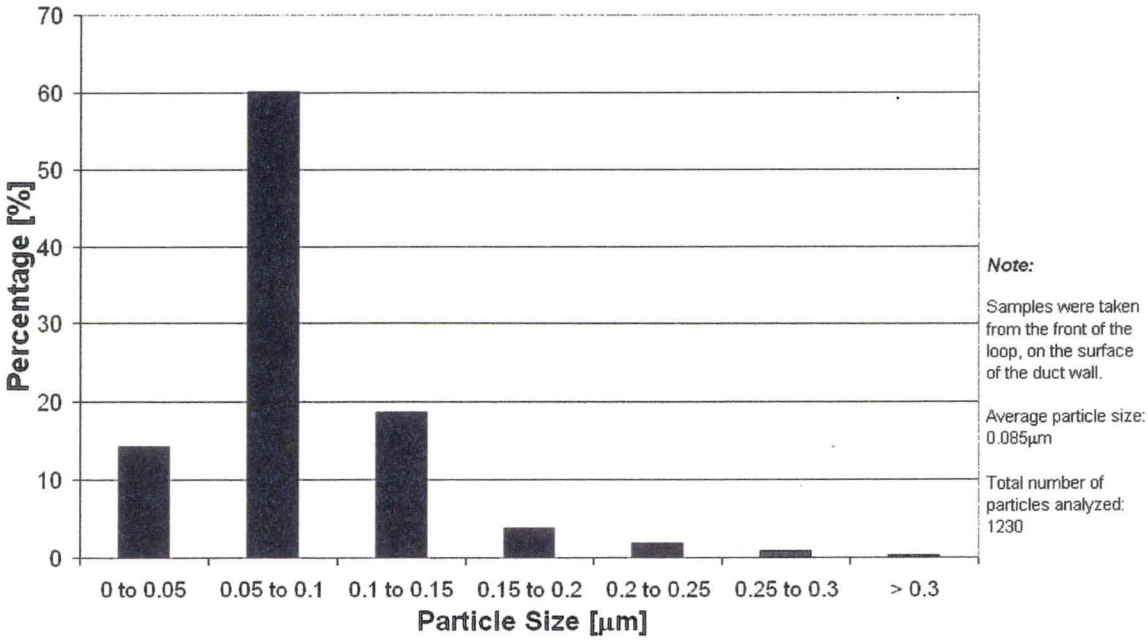

Figure 4.6 Size distribution analysis of deposited particles sampled at walls of upstream flow separator (MP1) for Q=7Nm^3/h, T=160°C, and sampling time=5 minutes

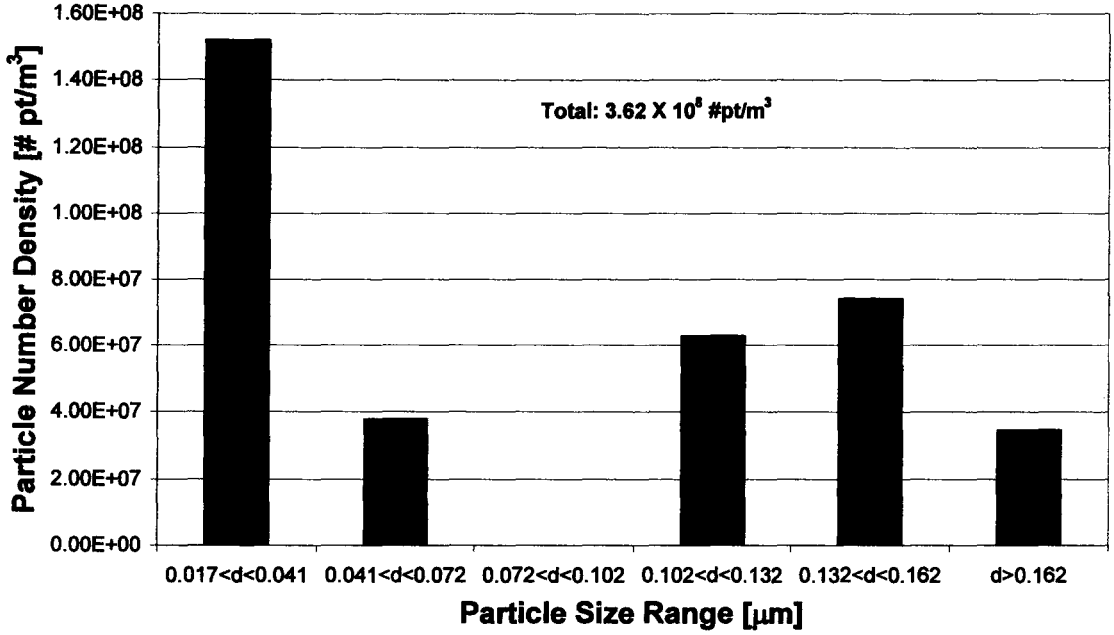

Figure 4.7 Particles size distribution at MP1 (upstream of DFS-ESP) for 5Nm^3/h and 0kV by CNPC-PSS without Insert

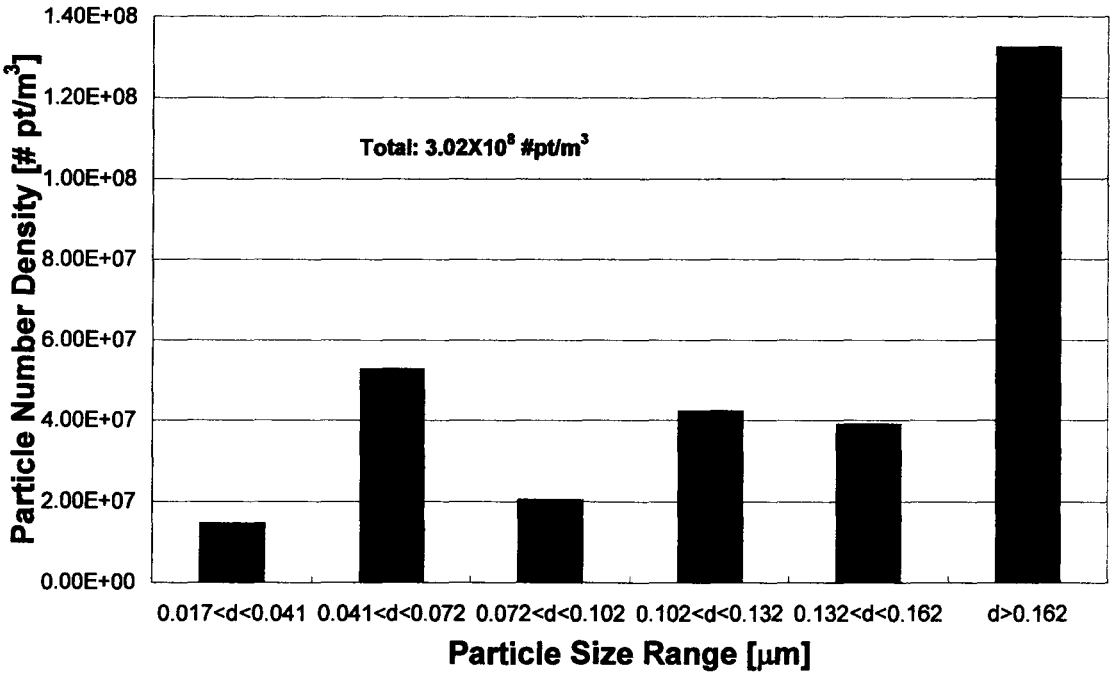

Figure 4.8 Particle Size Distribution for MP3 (middle of the main channel) at 8.5Nm^3/h and 0kV by CNPC-PSS, without Insert

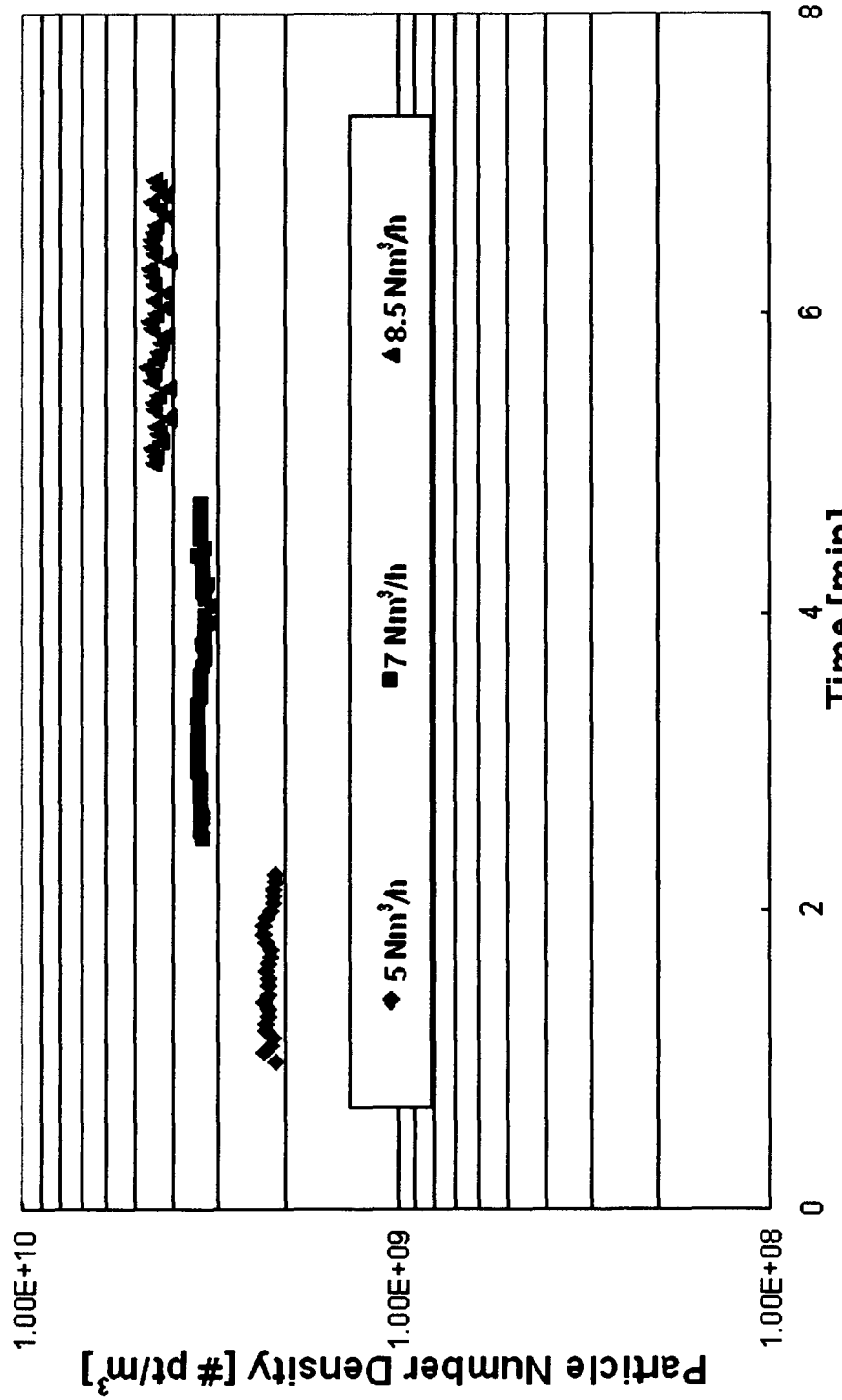

Figure 4.9 Particle number density vs. total inlet air flow rate measured at MP1 (upstream of DFS-ESP)

4.2 FUNDAMENTAL CHARACTERISTICS OF DUST FLOW SEPARATOR

The objective of dust flow separator is to separate most of the fine particles from the exhaust flow to ESP branch, while maintaining most of the flow in the main stream. Hence, characterizing the dust flow separator, flow profile and particle separation were conducted.

4.2.1 Flow Separation Characteristics

Experiments are performed under a cold test (without combustor on) and a hot test (with combustor on). During the hot test, the ESP influence on the flow separation is also tested. The experiment matrix is shown in Table 4.2.

Experimental results and the corresponding FLUENT predictions for cold test without operating ESP are compared in Figures 4.10 and 4.12, where FLUENT code simulation for DFS-ESP was conducted by Park et al. [102] and details are provided in Appendix A. Experimental radial flow distribution results for the hot test with 0kV ESP voltage is shown in Figure 4.13. The ESP effect on flow distribution is also tested, and the results are shown in the Figure 4.14 for time averaged flow velocity at upstream (MP1) versus ESP voltage at various Pitot tube locations for Q at 8.5Nm^3/h. For completeness, the results for the other test conditions are also given in Appendix B. All the results for the hot test (higher gas temperature) condition are normalized to standard conditions, i.e. 20°C and 1atm.

By comparing the difference between the cold air and hot combustion test conditions, it can be observed that the amount of natural gas flow rate is approximately 0.55~0.75Nm^3/h.

Table 4.2 Experiment matrix for flow profile diagnosis

Flow Rate (Nm^3/h)	Cold test (25°C)	Hot test (150~170°C)					
	V_{ESP}=0kV	0kV	10kV	15kV	20kV	25kV	27kV
5	√	√	√	√	√	√	√
7	√	√	√	√	√	√	√
8.5	√	√	√	√	√	√	√

Figures 4.10 to 4.13 show gas velocity profiles for the cold air test condition, where the X axis is the velocity in normal meter per second, and Y axis represents the velocity measurement radial locations on the flow profile shown in Figures 4.10 to 4.12. Examining the velocities at MP1, MP2 and MP3, the values are almost identical, which means only a small portion of the flow is separated to the ESP branch for 5, 7 and 8.5 Nm^3/h inlet total flow rates. Experimental measurements agree quantitively and qualitatively with the FLUENT predictions [102]. A similar trend is also observed on Figure 4.13, which shows the gas velocity profile for the hot combustion test condition. Results for MP1, MP2 and MP3 are indicated in Figure 4.13.

Measured velocities at different locations (1, 2, 3, 4 and 5) are integrated and averaged. This average velocity is used for quantitive analysis of flow separation ratio using Equation 4.1.

$$Q = \bar{u} \cdot A \tag{4.1}$$

By subtracting the flow rate at middle of main channel (MP3) from that at upstream (MP1), the flow rate in the ESP branch is determined. The comparison for flow rates between ESP branch and mainstream is shown in Figure 4.15. Since the flow rate in the ESP branch is relatively small, the real value is scaled 10 times to be shown in the Figure, for the purpose of trending. From Figure 4.15, the main flow increases and branch flow decreases as increasing total inlet flow rate. This demonstrates less flow is separated to the ESP branch as the total inlet flow increases. Flow separation efficiency is determined by:

$$\eta = (Q_{MP1} - Q_{MP3}) / Q_{MP1} \tag{4.2}$$

Hence for the different total inlet flows — 5, 7 and 8.5Nm^3/h, the flow separation efficiencies are approximately 3%, 2% and 1% respectively. The flow separation ratio is compared between experimental results and FLUENT predictions [102] in Figure 4.16, which as well shows a fair quantitive and good qualitative (trends) agreement.

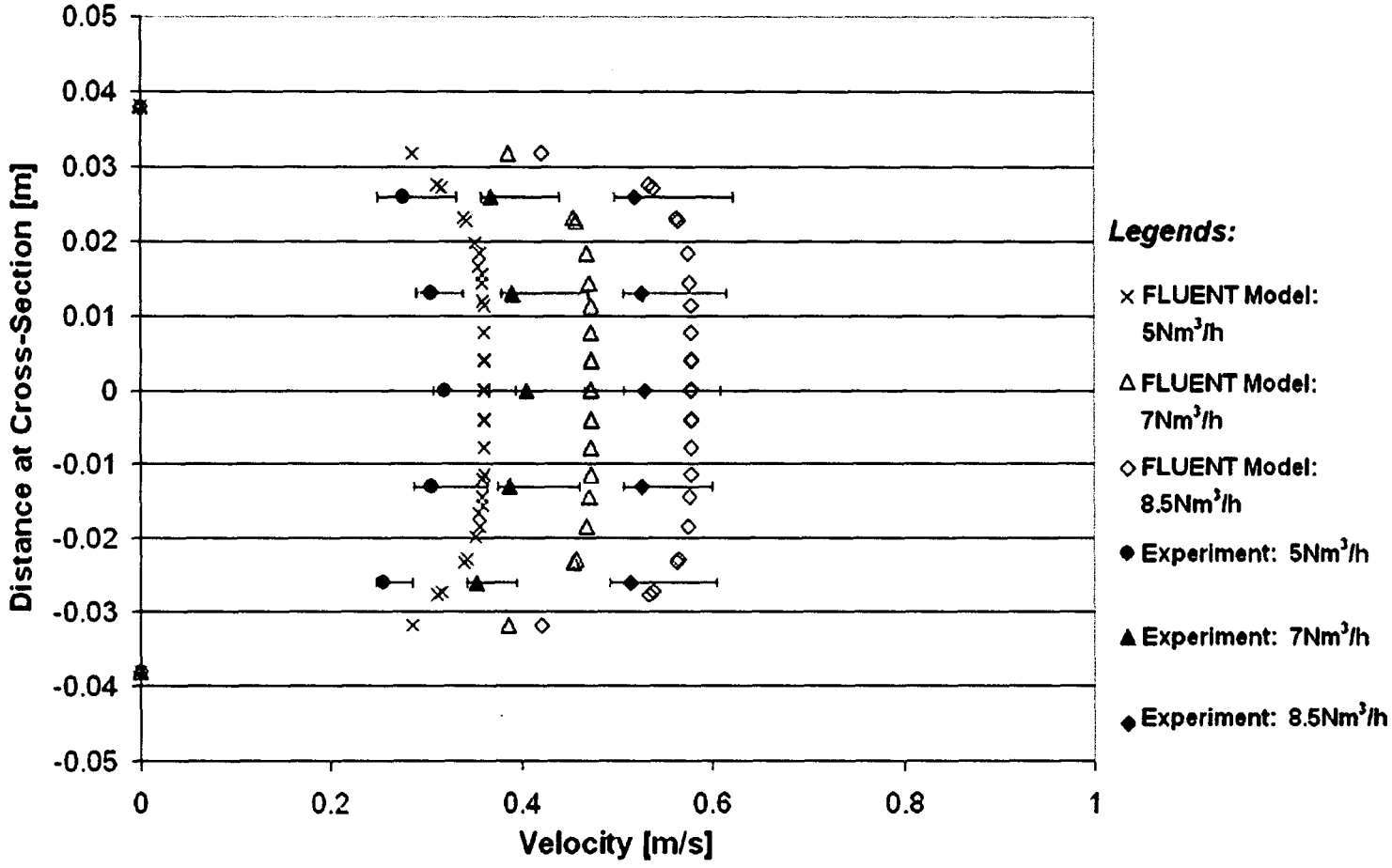

Figure 4.10 Comparison of gas velocity profile for upstream (MP1) at 5, 7 and 8.5Nm^3/h total inlet flow rate between experiment and FLUENT prediction [102] — Cold test

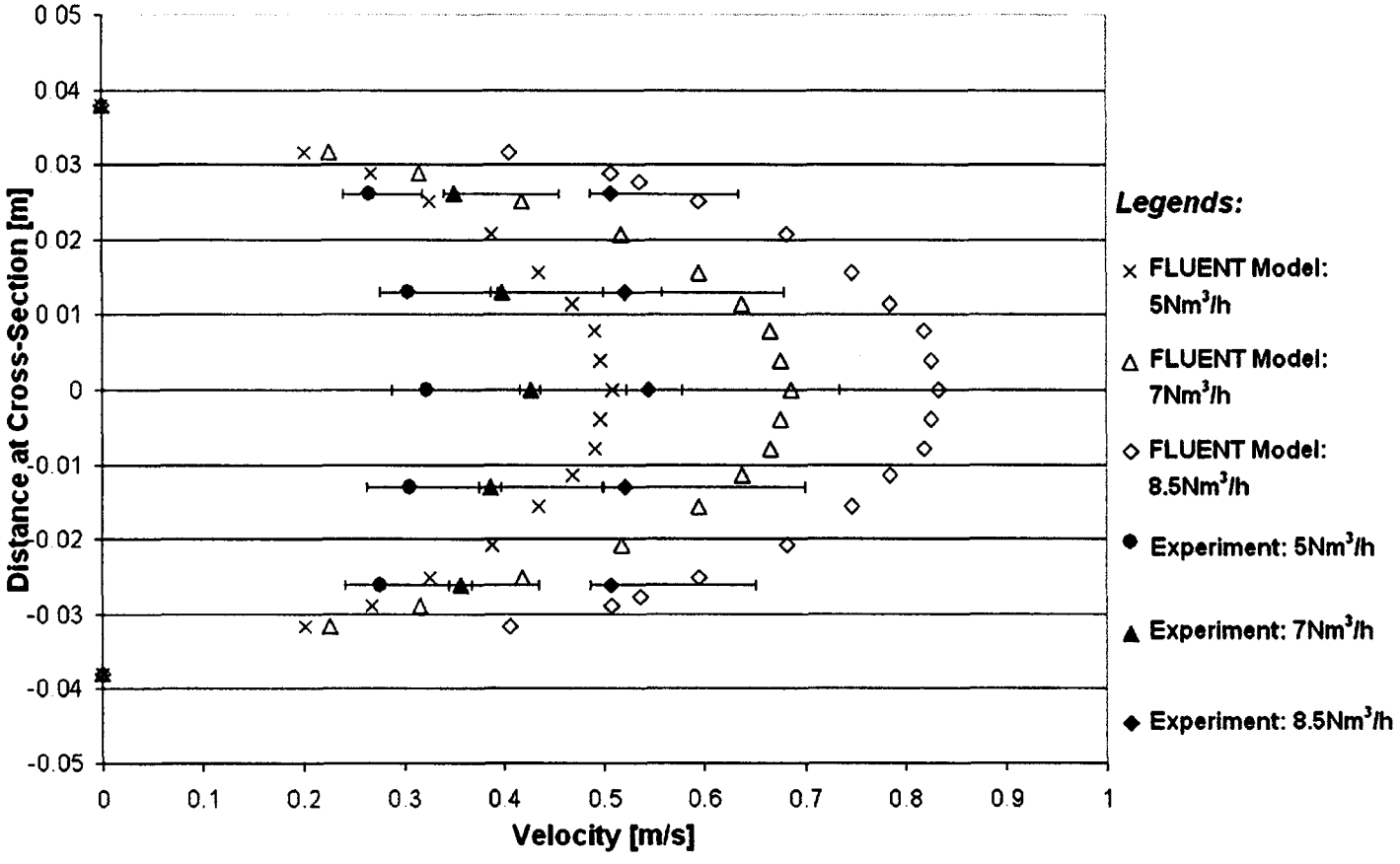

Figure 4.11 Comparison of gas velocity profile for downstream (MP2) at 5, 7 and 8.5Nm^3/h total inlet flow rate between experiment and FLUENT prediction [102] — Cold test

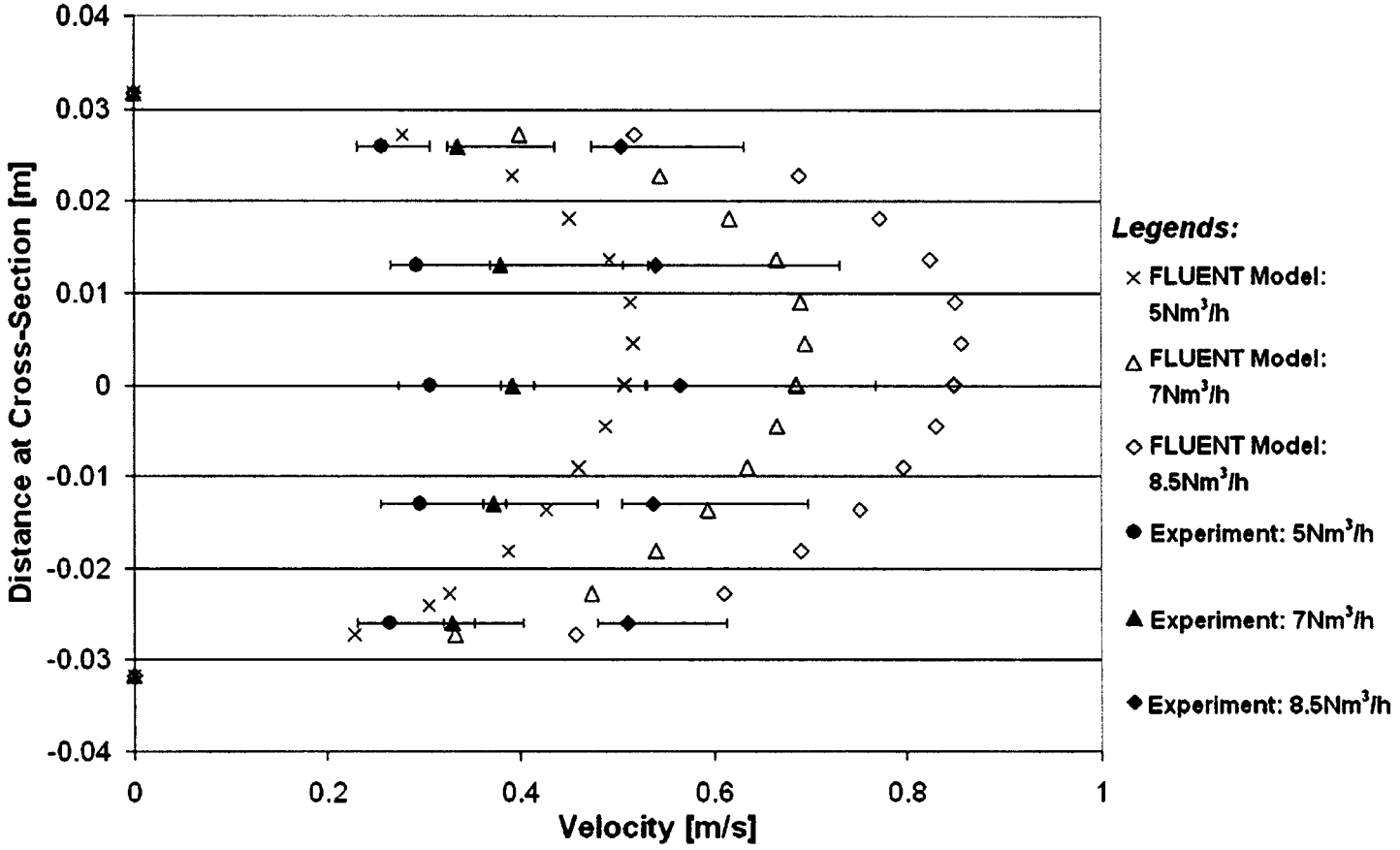

Figure 4.12 Comparison of gas velocity profile for middle of main channel (MP3) at 5, 7 and 8.5Nm^3/h total inlet flow rate between experiment and FLUENT prediction [102] — Cold test

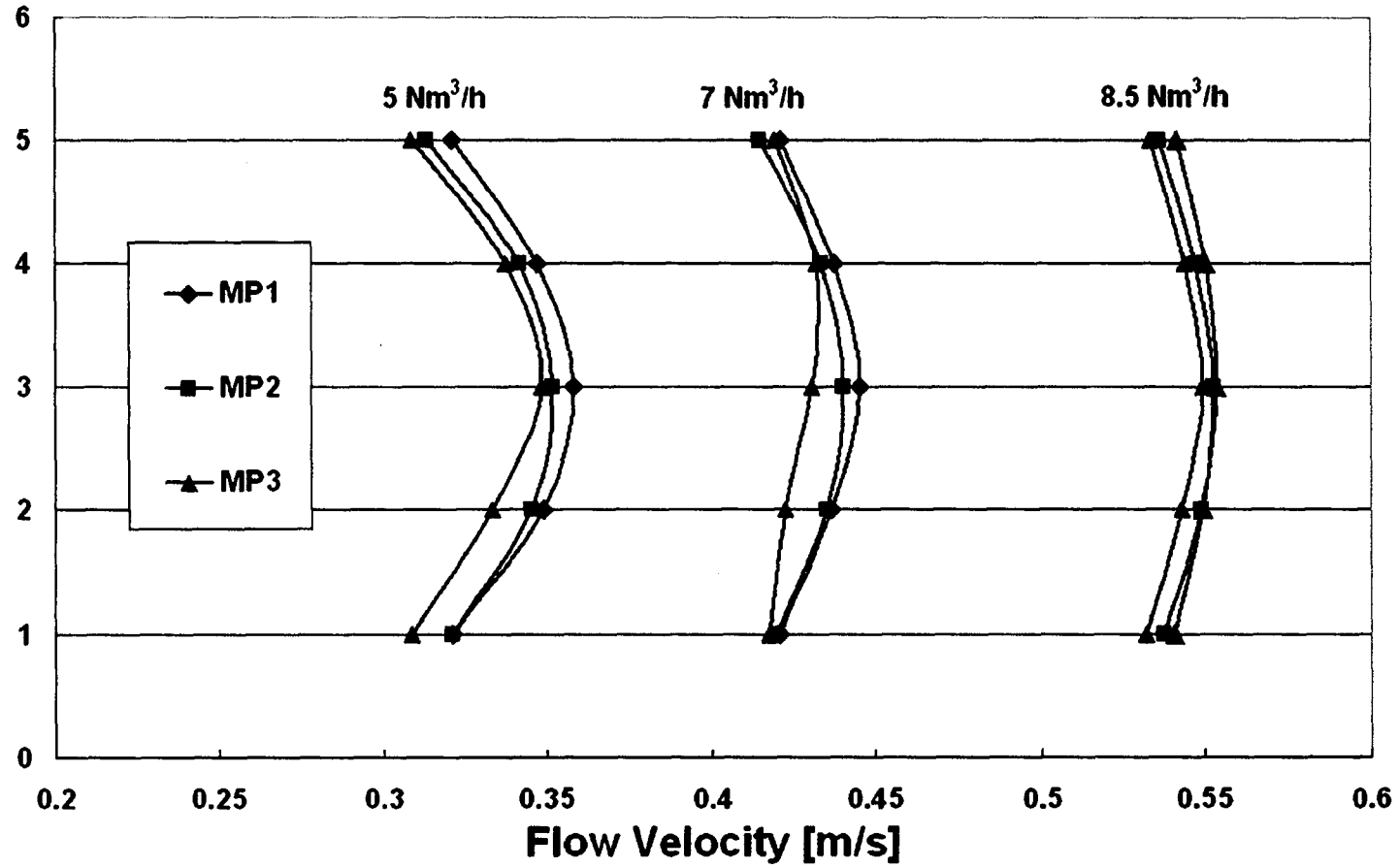

Figure 4.13 Mean gas flow profile for MP1, MP2, and MP3 – Hot test with 0kV ESP voltage

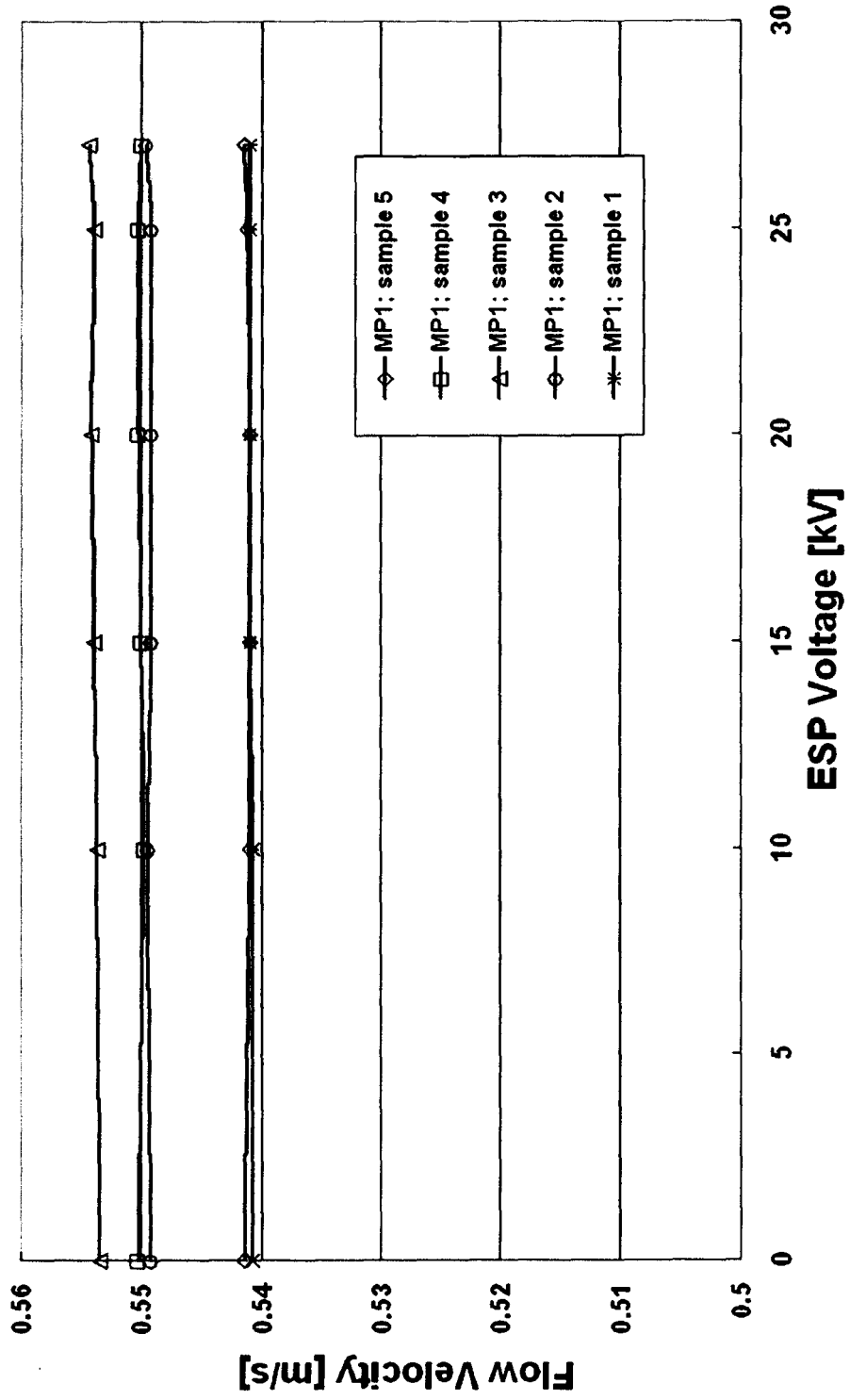

Figure 4.14 Time averaged flow velocity at upstream (MP1) vs. ESP voltage at various Pitot tube locations for Q at 8.5 Nm^3/h

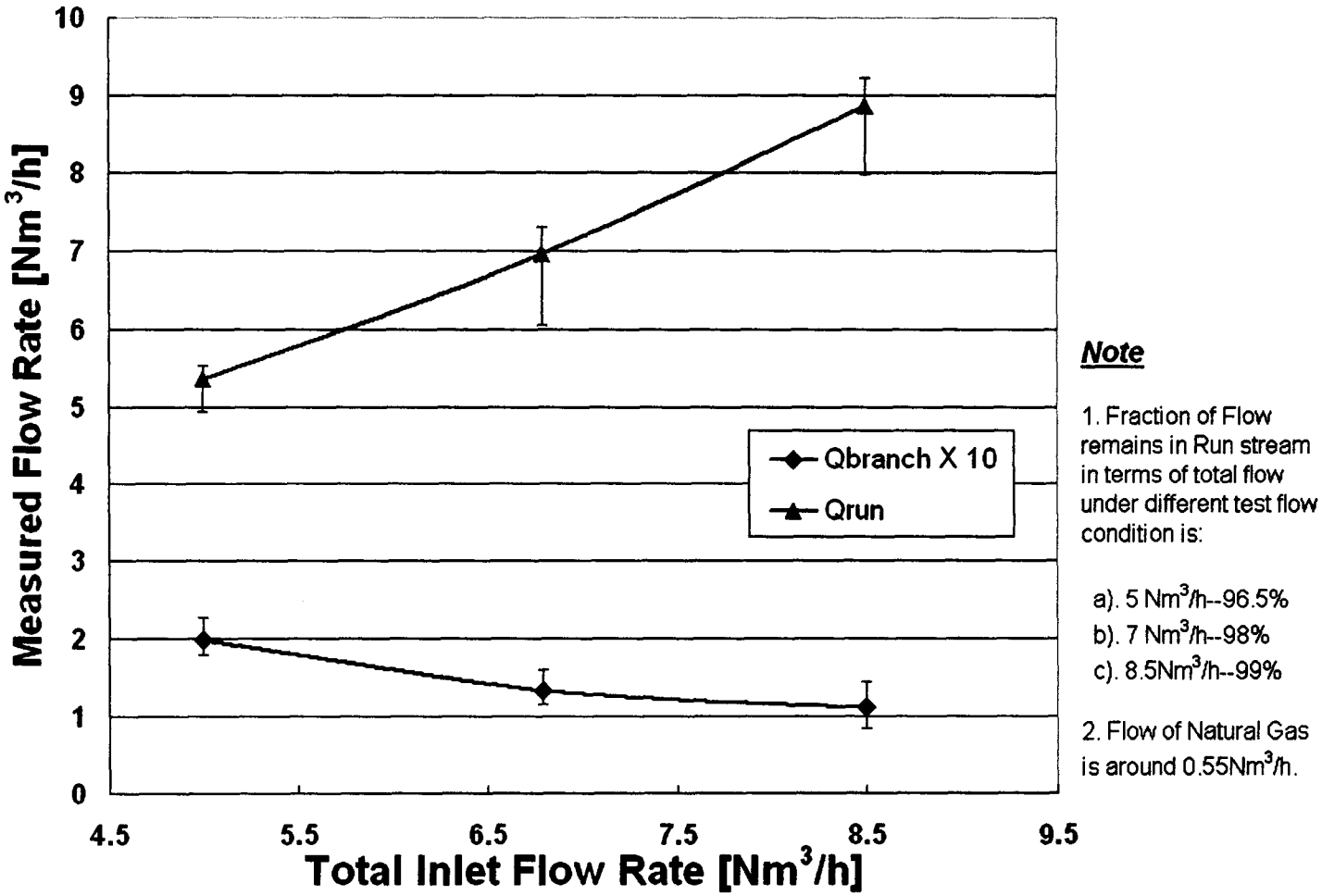

Figure 4.15 Flow rate at branch and run channel vs. total inlet flow rate

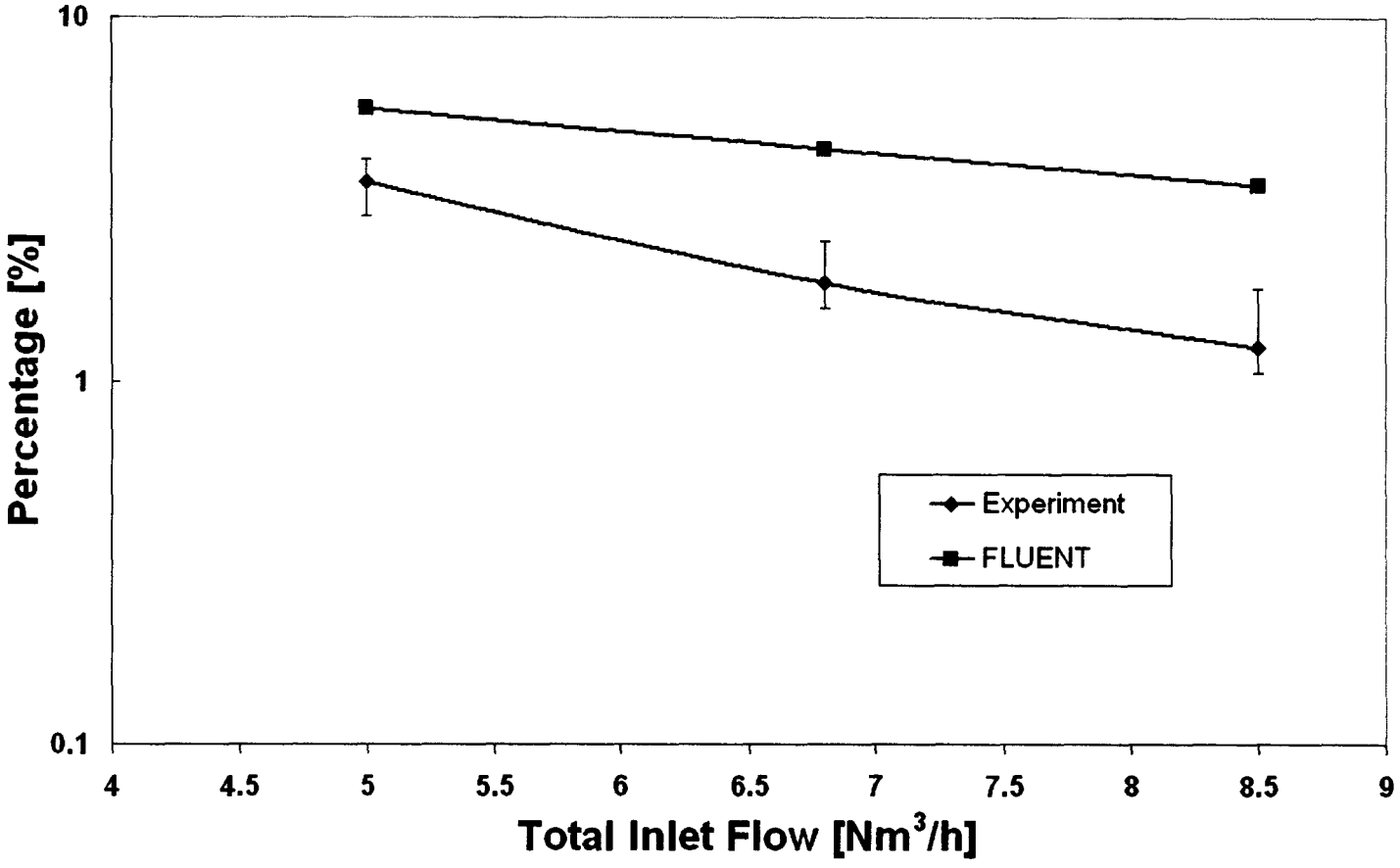

Figure 4.16 Comparison of flow separation ratio (Q_{branch}/Q_{total}) between experiment and FLUENT prediction [102]

4.2.2 Results for Particle Separation

Experiment matrix for DFS particle separation examination is shown in Table 4.3.

Table 4.3 Experiment matrix for particle separation diagnosis

Conditions \ Sampling Ports		*MP1*	*MP2*	*MP3*
5.0 Nm^3/h	CNPC	√	√	√
7.0 Nm^3/h	CNPC	√	√	√
	CNPC-PSS	√	√	√
8.5 Nm^3/h	CNPC	√	√	√

Experimental results of the particle number density versus different total inlet flow rate at upstream (MP1) and middle of main channel (MP3) are shown in Figure 4.17; and the corresponding size distribution for MP1, MP2 and MP3 at 7Nm^3/h is shown in Figure 4.18.

Figure 4.17 shows that the particle number density increases with increasing total inlet flow at upstream (MP1), and decreases at main channel (MP3), which demonstrates that more particles are separated at higher inlet flow.

Figure 4.18 shows the particle size distribution at MP1, MP2 and MP3 for total inlet flow at 7Nm^3/h. First of all, finer size particles (17~41nm) range at MP1 (upstream)

and MP2 (downstream), is approximately 15% difference, which most likely is the function of deposition of the whole DFS-ESP system. Secondly, particles with size range larger than 162 nm occupy most of the portion at MP3. From the above observations, we can also extrapolate that particles with smaller size range are separated at DFS section, especially effective with 17nm to 41nm size range; and particles show the trend of agglomeration at MP2 and MP3 at higher size range.

Furthermore, the separation efficiency can be computed by,

$$\eta = \frac{(N_{MP1} - N_{MP3})}{N_{MP1}} \times 100\% \qquad (4.3)$$

So that, separation efficiency for 17~41nm size range particles is 99.4%, and overall separation efficiency is around 90%.

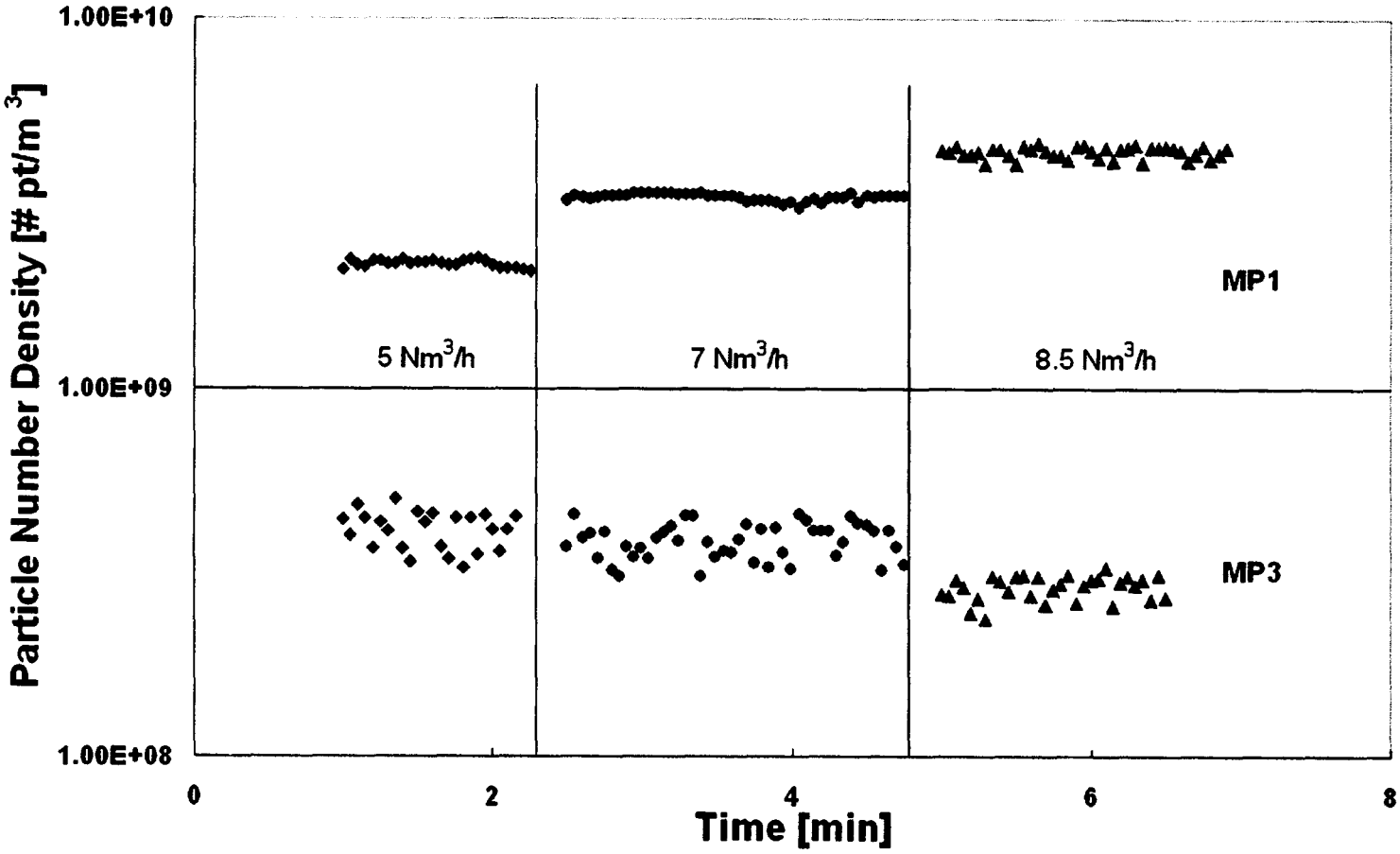

Figure 4.17 Comparison of particle number density for different total inlet flow rate at upstream (MP1) and main flow channel of DFS-ESP (MP3)

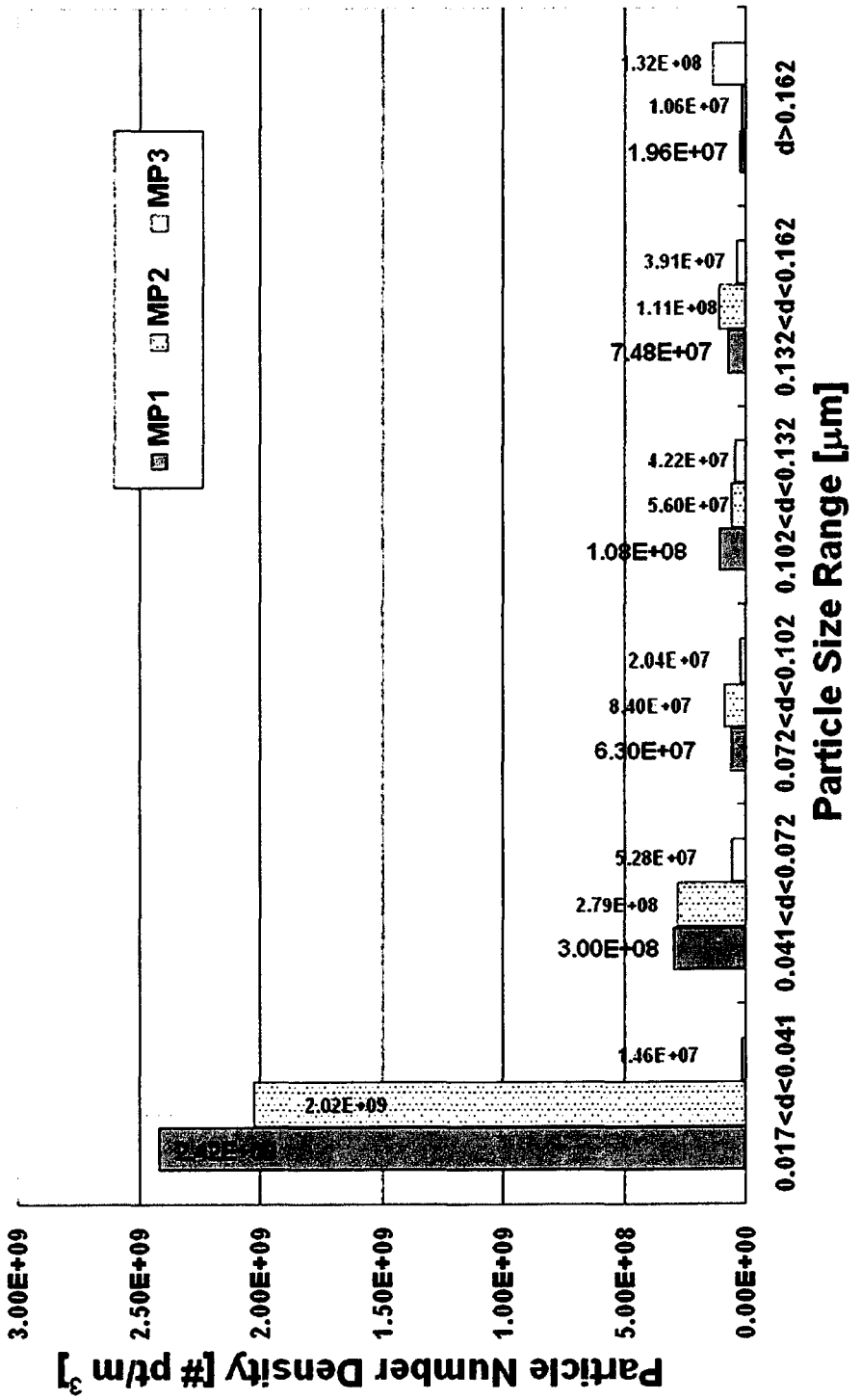

Figure 4.18 Size distribution comparison for MP1, MP2, and MP3 at 7Nm3/h and 0kV by CNPC-PSS with 30nm increment

4.3 FUNDAMENTAL CHARACTERISTICS OF ESP

Generally speaking, the efficiency of an electrostatic precipitator relies on the relationship between the applied high voltage and the resulting corona current. ESP sensitivity analysis using MESP code [99] also shows that those dimensional parameters affect the ESP collection efficiency, such as ESP pipe length, characteristic length, and corona wire diameter. For instance, changing the pipe characteristic length or the distance between corona electrodes, the electric flux field will be changed, inevitably modifying the current-voltage characteristic. The experiment conditions also influence ESP performance, such as exhaust temperature, and flow rate. It is well known that an interrelationship existing between the electric current and the flow field does induce secondary flows and change the turbulence structure. Therefore, the electric operation conditions coupling with the flow field would definitely influence the particle transportation; hence the collection efficiency is affected.

4.3.1 Current-Voltage Characteristic of ESP

The time-averaged current-voltage characteristic of the experimental ESP without particles for different inlet flow rates is shown in Figure 4.19. Particle density effects would not cause significant changes to the corona discharge behaviour, since the particle density emitted from the present natural gas combustion system is relatively low [38]. The results are presented in the format of applied voltage (kilovolts) versus square root of the current per unit length. Figure 4.19 shows that the corona-onset voltage decreases as the inlet flow rate increases under the same temperature and pressure condition. The

slopes of these curves are relatively similar, and the tested results agree with those predicted by MESP numerical simulations.

The time-averaged current-voltage characteristics for different diameters of corona wires are compared in Figure 4.20. The comparison is performed under the same experiment condition at $0Nm^3/h$ total inlet flow rate, and 20^oC ambient temperature. It is concluded from Figure 4.20 that corona-onset voltage increases with increasing corona wire diameter.

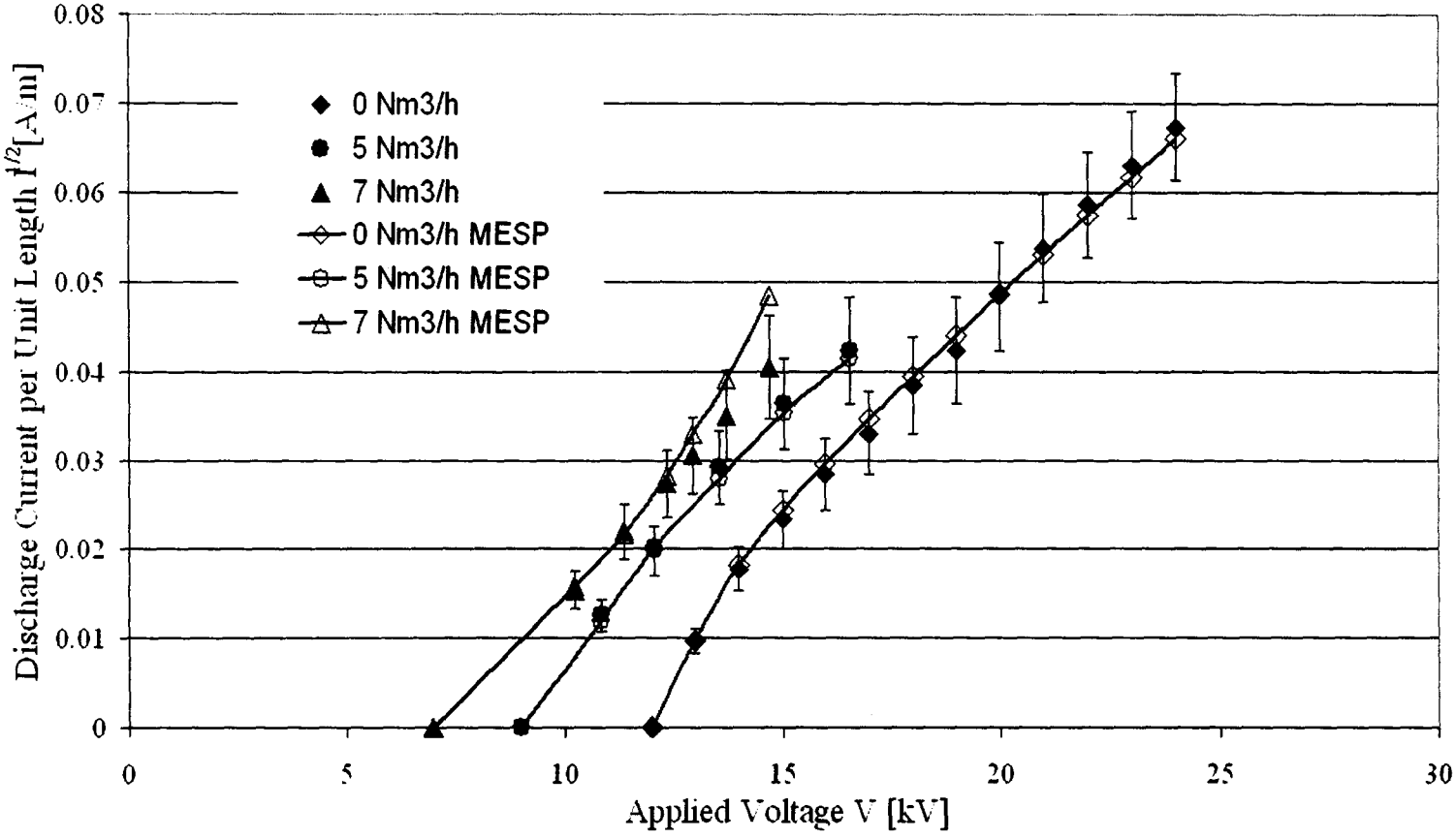

Figure 4.19 The time-averaged current-voltage characteristic of ESP for various total inlet flow rates from experiment and MESP code simulation

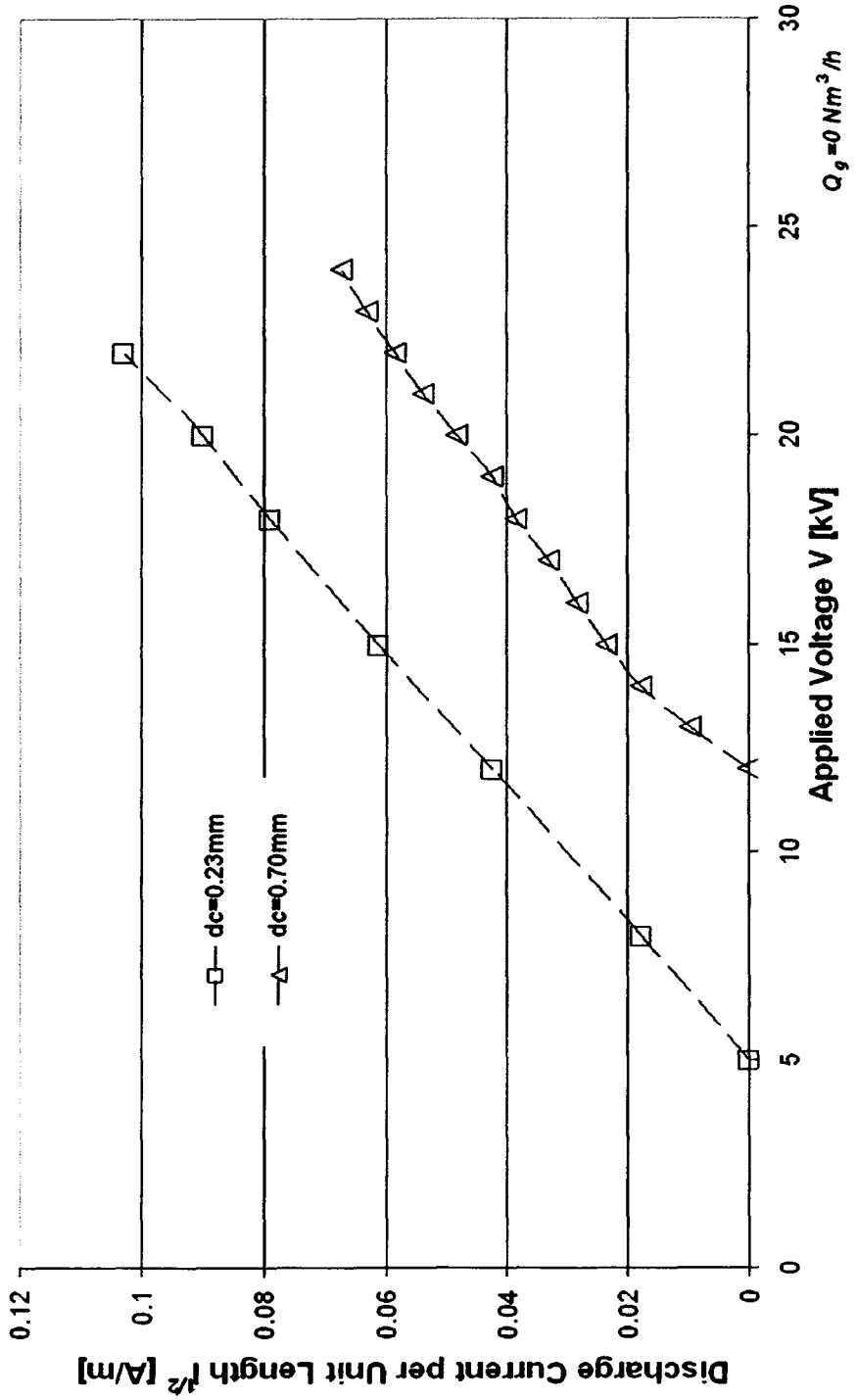

Figure 4.20 Time-averaged current-voltage characteristics for various corona wire diameters

4.3.2 Pressure Drop of the FS-ESP System

Measurement of the DFS-ESP system pressure drop is performed by a differential pressure transducer, between MP1 and MP2 as shown in Figure 4.21.

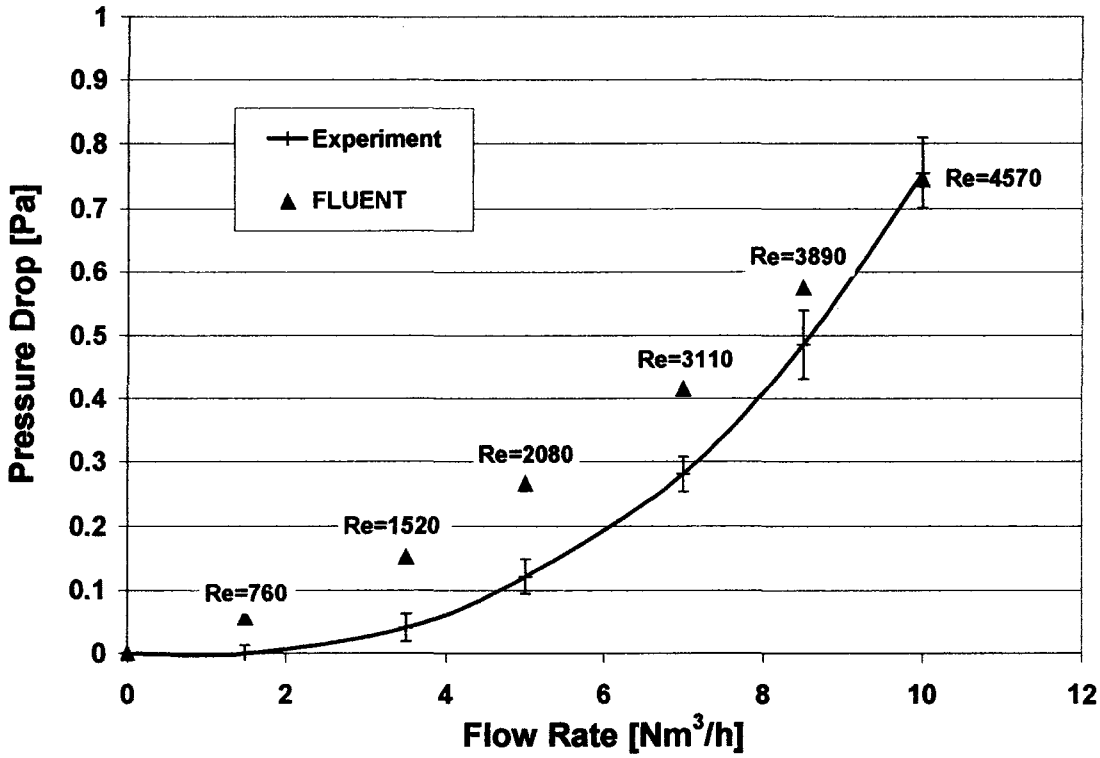

Figure 4.21 The comparison of experimental and numerical pressure drop of DFS-ESP vs. total inlet flow rate for the conditions without insert, particle flow, and ESP voltage

The system pressure drop increases as the total inlet flow rate increases as expected. The maximum pressure drop is less than 1Pa at the maximum reachable inlet flowrate tested for the DFS-ESP. FLUENT simulation [102] agrees quantitatively and within a factor of two with experimental measurements.

4.4 DFS-ESP COLLECTION EFFICIENCY OF PARTICLES

DFS-ESP system particle collection efficiency is analysed by both number and mass particle concentrations, as varying the corona wire diameters, gas flow rates, ESP applied voltages, and with/without insert. The experimental matrix is shown in Table 4.4.

Table 4.4 Experiment matrix for particle collection efficiency analysis

	CNPC [Number concentration]			OPC [Mass]
	0.7 mm [wire diameter]		0.23 mm [wire diameter]	0.7mm [wire diameter]
	With insert	Without insert		
2.5 Nm^3/h			√	
5.0 Nm^3/h	√	√		√
7.0 Nm^3/h	√	√		√
8.5 Nm^3/h				√

Note: Results of experiments with 0.23 and 0.7mm corona wire are compared and analyzed in Appendix B.

Particle collection efficiency based on number density is determined by:

$$\eta_d = \frac{N_{in} - N_{out}}{N_{in}} \times 100\% \qquad (4.4)$$

where N_{in} and N_{out} stand for the particle number density measured at upstream (MP1) and downstream (MP2) respectively.

Figure 4.22 shows the CNPC experimental results without the special designed insert structure for gas flow rates of 5 and 7Nm^3/h. Temperature at upstream (MP1) is 165°C, and 125°C at downstream (MP2). Total particle number density is in the range of 2 ~ 4x10^9 #pt/m^3. From the flow rate analysis in section 4.2, the ESP branch flow rates are approximately 0.20 and 0.14Nm^3/h for 5 and 7Nm^3/h total inlet gas flow rates. Using all of the above information as inputs for the MESP code, the results of numerical simulation are calculated and compared with the experimental results. Figure 4.22 shows that collection efficiency increases with increasing total inlet gas flow rate and ESP applied voltage, where the relatively low collection efficiency before corona-onset voltage may be due to the diffusion and thermophoresis effects within the entire system. The experimental results and MESP prediction agree qualitatively and quantitatively for above 20kV ESP voltage and 7Nm^3/h gas flow rate, where quantitative analysis shows that about 95% particle collection efficiency based on the number concentration can be obtained at 7Nm^3/h and ESP voltage above 20kV.

Figures 4.23 and 4.24 are the comparison with and without insert under the same experiment conditions. The locations of inserts are as indicated in Figure 3.4. Figure 4.23 shows the comparison for 7Nm^3/h gas flow rate, and Figure 4.24 shows the results for 5Nm^3/h. Both Figures 4.23 and 4.24 show that the collection efficiency is reduced when the insert is applied in the system. The dependence of particle collection efficiency versus gas flow rate is reversed compared with Figure 4.22 (i.e., without the insert). The reason for reducing collection efficiency by inserts is unclear, however it might be due to the

flow separation to the branch may decrease due to extra pressure increase in the inlet section of the main channel with the insert system due to unoptimized location placed.

Results for particle mass concentration based collection efficiency are presented in Figure 4.25. The maximum particle gross mass detected by OPC is around 1.05mg/cm^3. Mass particle collection efficiency is determined as the same as Equation 5-10 if replacing the N to M (mass density measured at both upstream (MP1) and downstream (MP2)). Comparing with the number particle collection efficiency, particle mass based collection efficiency is small, where the highest value is around 76%. The reason might be due to the particle agglomeration at the exit of ESP, since the particle number density is reduced while the mass density is not affected due to agglomeration. Beside, the detection limit of the instrument used for mass density ($\pm 0.01mg/m^3$) may contain a few percentage error in the present range of measurement.

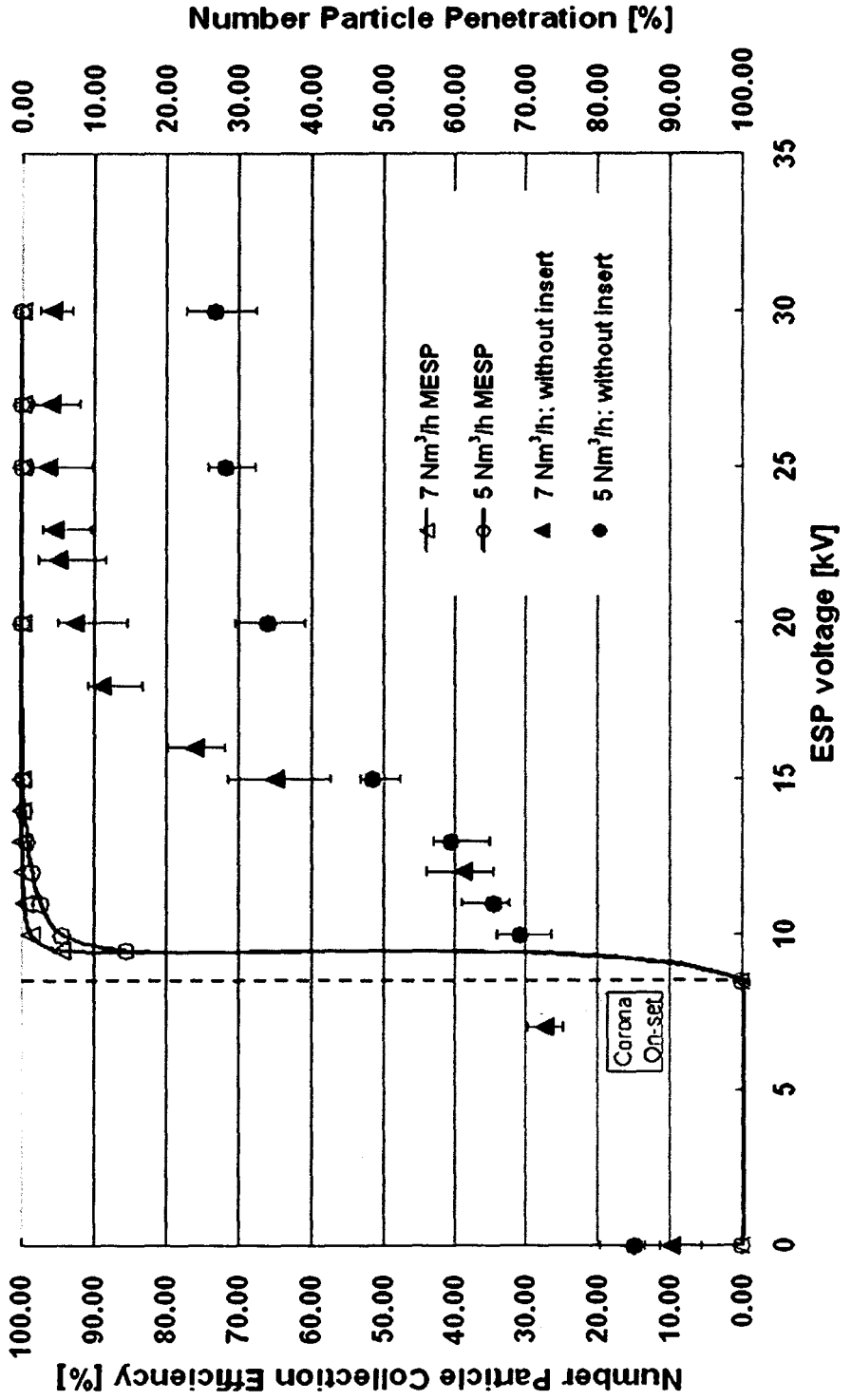

Figure 4.22 Particle collection efficiency based on number density versus ESP voltage for different gas flow rates without insert, compared with MESP modeling results

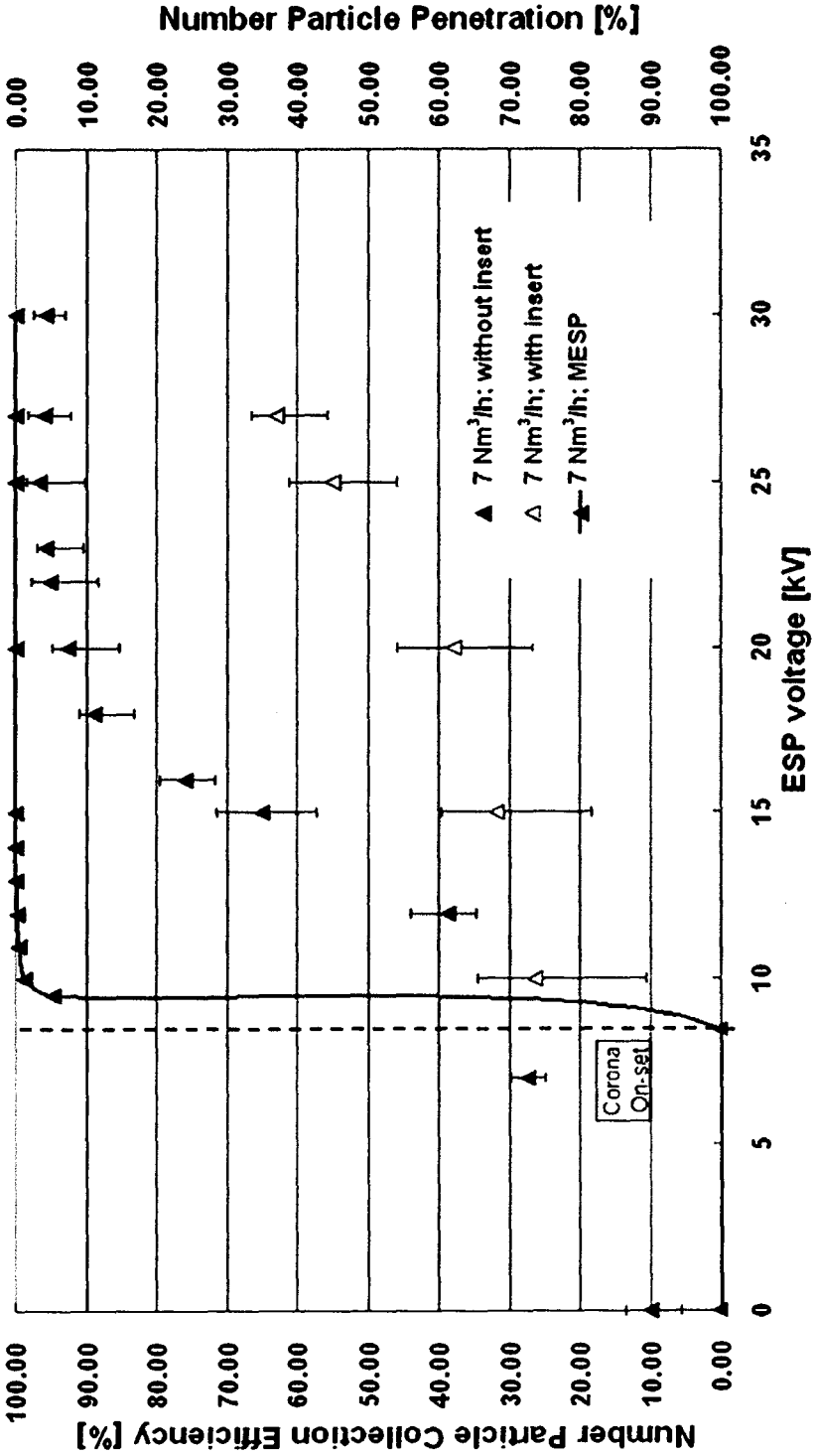

Figure 4.23 Comparison of particle collection efficiency based on number density versus ESP voltage for 7 Nm^3/h gas flow rate with and without insert

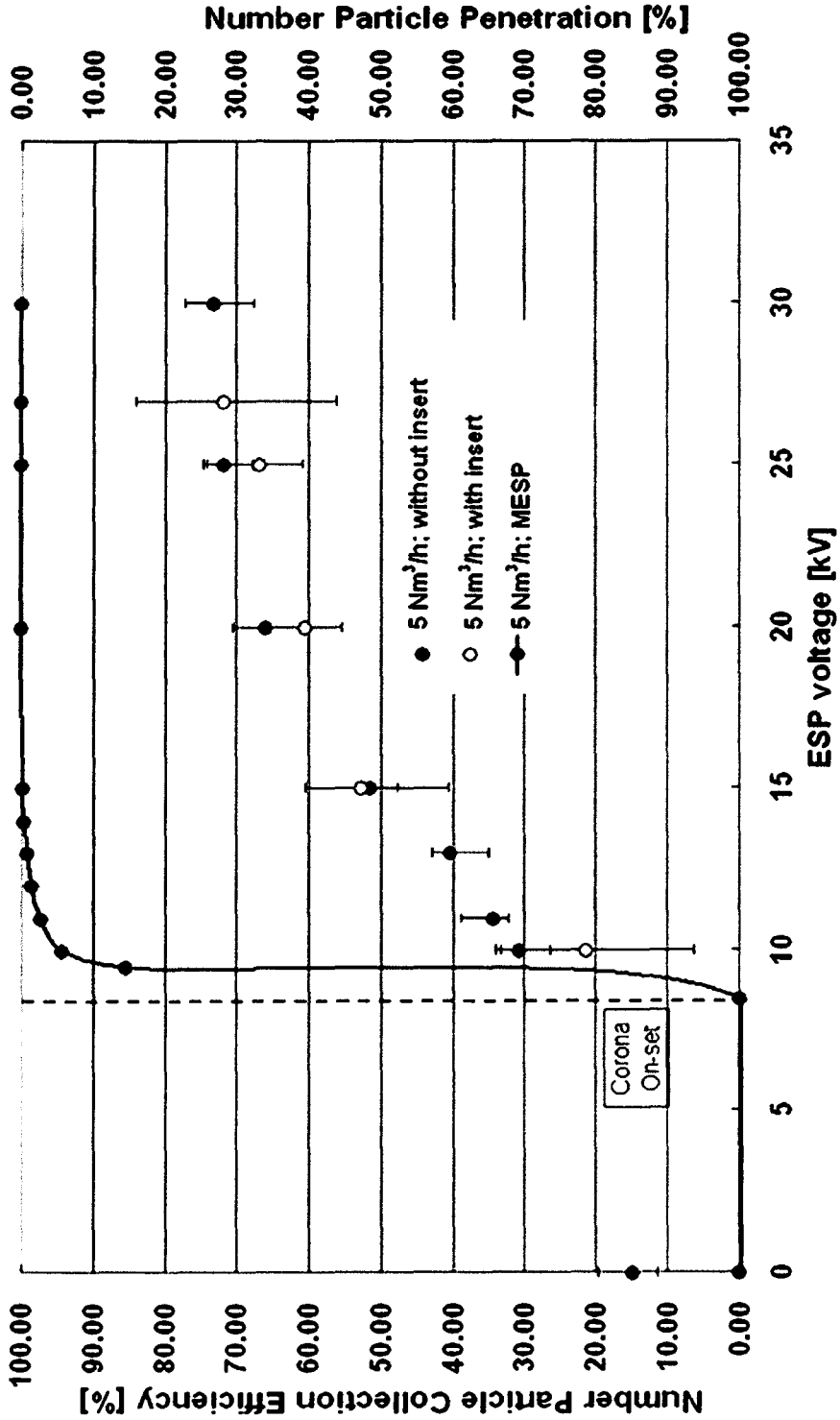

Figure 4.24 Comparison of particle collection efficiency based on number density versus ESP voltage for 5 Nm^3/h gas flow rate with and without insert

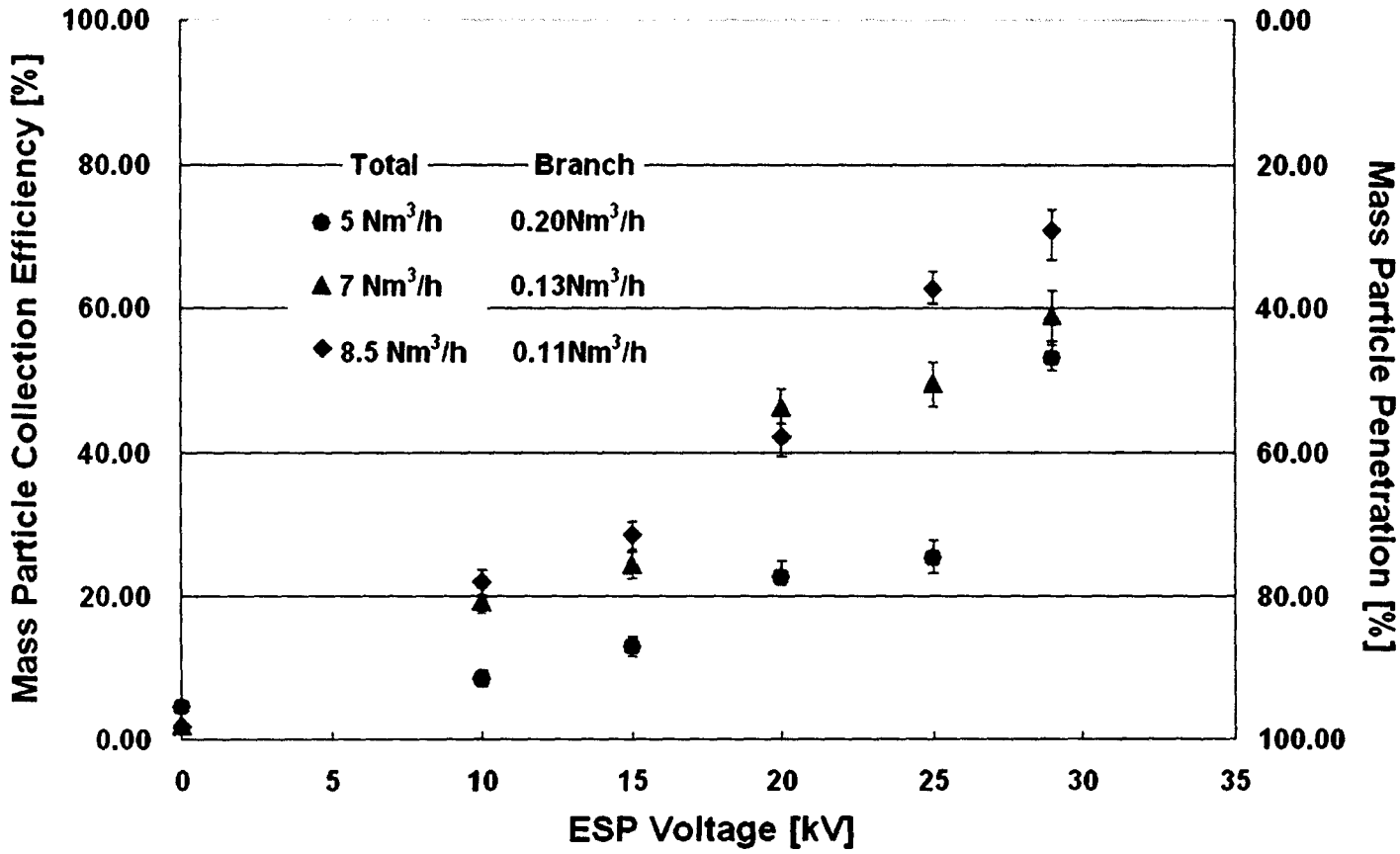

Figure 4.25 Particle collection efficiency based on mass fraction versus ESP voltage for different gas flow rates without insert

Further analysis for partial particle collection efficiency is conduced using CNPC-PSS. Results are shown in Figures 4.26 and 4.27 for the collection efficiency at 20kV ESP voltage, and 5Nm^3/h and 7Nm^3/h gas flow rate separately. It indicates that the most particle number collection efficiency can be obtained for fine particles in the range of 17 to 41nm, which is 86.6% for 5Nm^3/h gas flow rate, and 95.6% for 7Nm^3/h gas flow rate. Agglomeration can be extrapolated for particles' size in the ranges of 72 to 102nm and above 162nm.

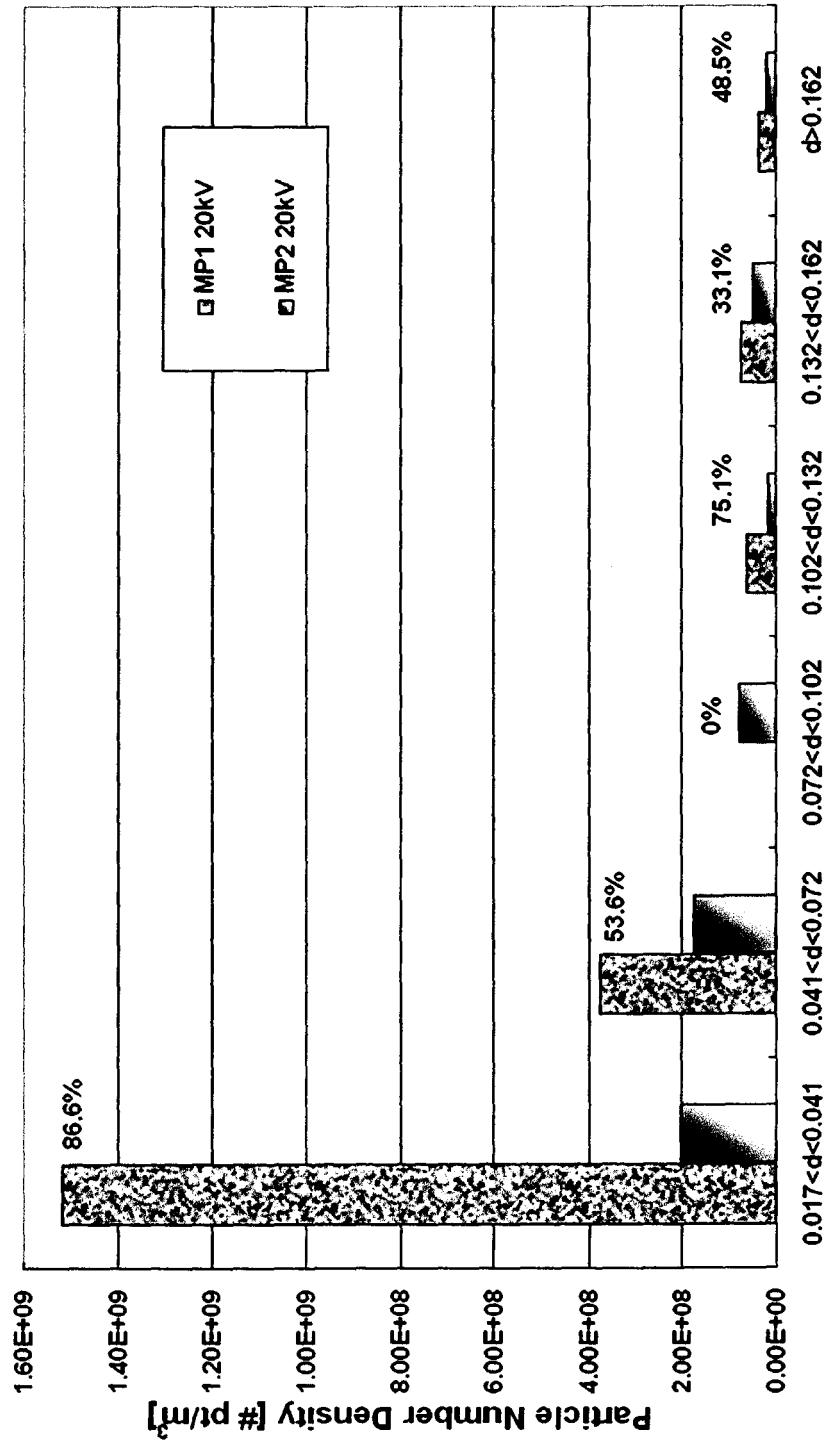

Figure 4.26 Particle collection efficiency based on number density at 20kV ESP voltage and 5Nm^3/h by CNPC-PSS with 30nm increment

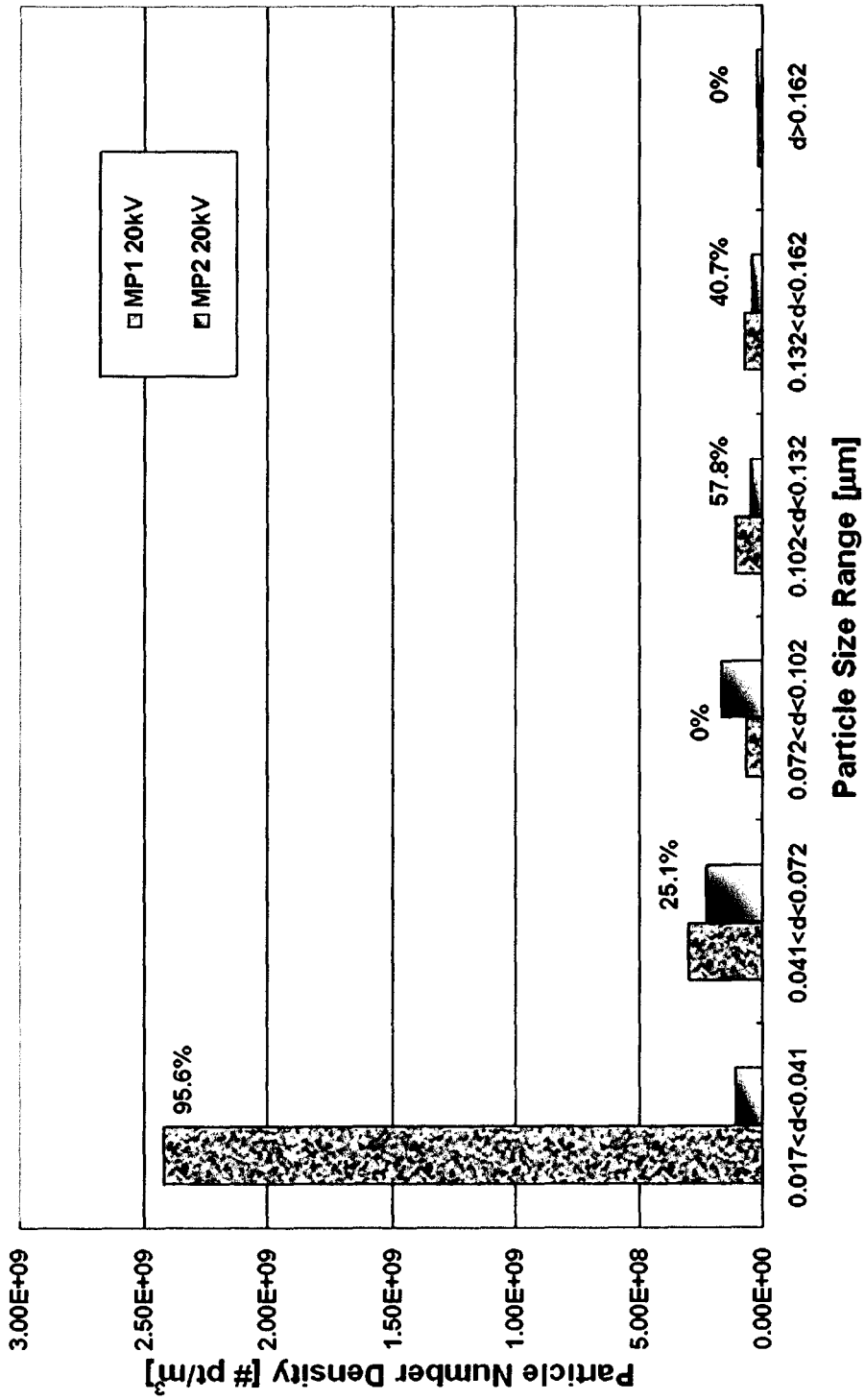

Figure 4.27 Particle collection efficiency based on number density at 20kV ESP voltage and 7Nm^3/h by CNPC-PSS with 30nm increment

CHAPTER 5

CONCLUSIONS

Dust flow separator type electrostatic precipitator for a control of fine particle emission from natural gas combustion was experimentally and numerically investigated, and the following conclusions were obtained:

1. Size of particles from natural gas combustion ranges from smaller than 17 to 300nm, with a maximum particle mass density at 1.05mg/cm^3 and number density approximately at 5x10^8 to 5x10^9 #pt/m^3 depending on combustion conditions.
2. Particle size shows a bimodal distribution by CNPC-PSS method with peaks for particle groups in the range from 17 to 41nm and 132 to 162nm in diameter, at upstream of DFS-ESP; and the size distribution at main flow channel of DFS-ESP shows a similar bimodal distribution with the peaks for particle groups in the range from 41 to 72nm and greater than 162nm.
3. The flow separation efficiencies of the flow separator are approximately 3%, 2% and 1% for 5, 7 and 8.5Nm^3/h total inlet flow rate respectively, while the particle separation efficiencies are 97%, 98% and 99% for 5, 7 and 8.5Nm^3/h total inlet flow rate respectively.
4. The experimental results and MESP code prediction for particle collection efficiency based on particle number density for DFS-ESP without the insert agree qualitatively and quantitatively for above 20kV ESP voltage and 7Nm^3/h gas flow

CHAPTER 5

CONCLUSIONS

Dust flow separator type electrostatic precipitator for a control of fine particle emission from natural gas combustion was experimentally and numerically investigated, and the following conclusions were obtained:

1. Size of particles from natural gas combustion ranges from smaller than 17 to 300nm, with a maximum particle mass density at 1.05mg/cm^3 and number density approximately at 5x10^8 to 5x10^9 #pt/m^3 depending on combustion conditions.
2. Particle size shows a bimodal distribution by CNPC-PSS method with peaks for particle groups in the range from 17 to 41nm and 132 to 162nm in diameter, at upstream of DFS-ESP; and the size distribution at main flow channel of DFS-ESP shows a similar bimodal distribution with the peaks for particle groups in the range from 41 to 72nm and greater than 162nm.
3. The flow separation efficiencies of the flow separator are approximately 3%, 2% and 1% for 5, 7 and 8.5Nm^3/h total inlet flow rate respectively, while the particle separation efficiencies are 97%, 98% and 99% for 5, 7 and 8.5Nm^3/h total inlet flow rate respectively.
4. The experimental results and MESP code prediction for particle collection efficiency based on particle number density for DFS-ESP without the insert agree qualitatively and quantitatively for above 20kV ESP voltage and 7Nm^3/h gas flow

rate, where quantitative analysis shows that about 95% particle collection efficiency based on the number concentration can be obtained.

5. The experimental results of DFS-ESP for particle collection efficiency based on particle number density with the extra insert in the main flow channel show that collection efficiency will be reduced.

6. The collection efficiency based on particle mass density increases with increasing ESP voltage and total inlet gas flow. However, compared with those based on particle number density, the collection efficiency is lower with a maximum achievable value of 76% for 8.5Nm^3/h inlet flow and 30kV ESP voltage.

7. The maximum pressure drop across the DFS-ESP is lower than 1Pa at the present range of inlet flow rate tested and agree with CFD code simulations.

CHAPTER 6

FUTURE WORK

Further analysis should be performed in a few different aspects of this work.

For the numerical modeling of the DFS-ESP, the following aspects should be considered:

1. The prediction of particle separation by DFS is recommended to be completely analyzed using the FLUENT code. Prediction results should be compared with the present experimental results.
2. MESP 3D model should be developed to predict the detailed behavior of particle distribution in the ESP section.

Based on the experimental results, the particle collection efficiency based on mass density is relatively low using the present DFS-ESP. Essentially, the fine particles are being collected or agglomerated and the large particles (high mass) are not being collected. For improving the particle collection efficiency, the mechanism of particle movement inside DFS-ESP should be further analysed, such as the temperature effects (thermophoresis). It is suggested to perform a particle distribution analysis by ESEM of the cross-section profile at different locations (such as upstream of the DFS-ESP, the far- and near-region of the DFS, and downstream of DFS-ESP).

The natural gas combustion should be well controlled to obtain a stable fine particle source. A flow meter is recommended to be installed in the natural gas feeding line, for achieving a relatively fixed air-to-fuel ratio.

In the future, the removal of collected particles in the DFS-ESP should be considered. It could be oxidized by plasma or incinerated by electrical heat for eliminating re-entrainment problem as proposed in design objectives. The suggested locations for plasma soot incineration system are proposed at the entrance and exit of ESP section.

After all above analysis is done, a small scale DFS-ESP suited for the real natural gas industrial application would be tested.

REFERENCES

1. J.S.Chang, *Next generation integrated electrostatic gas cleaning systems*, J. of Electrostatics, Vol. 57, 273~291, 2003.
2. Mark Z. Jacobson, *Aerosol particles in smog and the global environment*, Atmospheric pollution: History, science, and regulation, Cambridge University Press, pp.116~143, 2002.
3. *Task group on lung dynamics*, Health Physics, Vol. 12, 173, 1966.
4. Guangda Ma, *The harm of aerosol pollution and its removal*, Atmosphere Pollution Control, Chinese Environment Science Press, pp.3~13, 1985.
5. J. M. Marchello, *Particle control equipment*, Control of air pollution sources, New York: Marcel Dekker, Inc., pp.119~184, 1976.
6. Masuda and Hosokawa, E*lectrostatic precipitation*, Handbook of electrostatic processes, Editors: J.S.Chang, A.J.Kelly, and J.M.Crowley, Marcel Dekker, Inc., New York, Ch.21, pp.441~479, 1995.
7. D. Brocilo, L. Guan, G. D. Harvel, and J. S. Chang, *Characterization of particle emission from nature gas combustion*, J. Aerosol Science, S., 877~878, Abstract of European Aerosol Conference, Volume II, Hungary, Sept. 6-10th, 2004.
8. M. Medici, *Gas properties*, The Natural Gas Industry, London: Newnes-Butterworths, Ch.3, pp.60~77, 1974.
9. U.S. Environment Protection Administration, *Natural gas combustion*, Emission factors, Section 1.4, 1.4-1~1.4-10, 1998.
10. D. Leith, and W. Licht, *The collection efficiency of Cyclone type particle collectors: A new theoretical approach*, AIChE. Symp. Ser., Vol. 68(126), 196, 1972.
11. R. G. Dorman, *Filtration*, Aerosol Science, Editor: C. N. Davies, New York: Academic Press, 1966.

12. C. N. Davies, *Air Filtration*, London: Academic Press, 1973.

13. A. Ogawa, *Separation of Particles from Air and Gases*, Boca Raton II., Fla.: CRC Press, 1984.

14. Kefa Jin, *Principles and Technology of Gas-solid Separation*, Zhejiang University Press, 1999.

15. N. A. Fuchs, Mechanics of Aerosols, London: Pergamon Press, 1964.

16. W. C. Hinds, *Aerosol Technology—Properties, Behavior, and Measurement of Airborne Particles*, New York: John Wiley & Sons Publication, 1982.

17. A. Einstein, *On the Kinetic Molecular Theory of Thermal Movements of Particles Suspended in a Quiescent Fluid,* Ann. Physics, Vol. 17, 549~60, 1905. [English translation, A. Einstein, *Investigations on the Theory of Brownian Movement,* R. Furth (Ed.), translated by A. D. Cowper, Dover, New York, 1956]

18. H. E. Hesketh, *Fine Particles in Gaseous Media*, Ann Arbor: Ann Arbor Science, 1977.

19. L. Waldmann, and K. H. Schmitt, *Aerosol Science*, Editor: C. N. Davies, London: Academic Press, 1966.

20. L. Talbot, R. K. Cheng, R. W. Schaefer, and D. R. Willis, *Thermophoresis of particles in a heated boundary layer*, J. Fluid Mech., Vol. 101 (4), 737~758, 1980.

21. G. Nishio, S. Kitani, and K. Takahashi, *Thermophoretic deposition of aerosol particles in a heat exchanger pipe*, Ind. Eng. Chem, Process Des. Development, Vol. 13 (4), 408~415, 1974.

22. R. L. Byers, and S. Calvert, *Particle deposition from turbulent streams by means of thermal force*, I & EC Fundamentals, Vol.8 (4), 646~655,1969.

23. F. J. Romay, S. S. Takagaki, D. Y. H. Pui, and B. Y. H. Liu, *Thermophoretic deposition of aerosol particles in turbulent pipe flow*, J. Aerosol Science, Vol.29 (8), 943~959, 1998.

24. J. Stier and M. Quinten, *Simple refractive index correction for the optical particle counter PCS 2000 by Palas,* J. Aerosol Sci. Vol. 29, No. ½, 223~225, 1998.

25. R. Friehmelt and S. Heidenreich, *Calibration of a White-light/90° Optical Particle Counter for "aerodynamic" Size Measurements—Experiments and Calculations for Spherical Particles and Quartz Dust,* J. Aerosol Science, Vol. 30 (10), 1271~1279, 1999.

26. Christine S. Sloane *et al., Measurements of Aerosol Particle Size: Improved Precision by Simultaneous Use of Optical Particle Counter and Nephelometer,* Aerosol Sci. and Tech., Vol. 14, 289~301, 1991.

27. Donald J. Holve and G. W. Davis, *Sample volume and alignment analysis for an optical particle counter sizer, and other applications,* Applied Optics, Vol.24 (7), 998~100, 1985.

28. Norman F. Robinson and Dennis Lamb, *On the Calibration of an Optical Particle Counter,* Aerosol Science and Technology, Vol. 5, 113~116, 1986.

29. H. C. Van de Hulst, *Light Scattering by Small Particles,* New York: Wiley, 1957.

30. M. Kerker, *The Scattering of Light and Other Electromagnetic Radiation,* New York: Academic Press, 1969.

31. B. Sachweh, H. Umhauer, F. Ebert, H. Büttner and R. Friehmelt, *In Situ optical particle counter with improved coincidence error correction for number concentrations up to 10^7 #pt/cm^3,* J. Aerosol Science, Vol.29 (9), 1075~1086, 1998.

32. Umhauer and Berbner, *Optical in situ size analysis of particles dispersed in gases at temperatures of up to 1000°C,* PARTEC, 6th European Symp. Particle Characterizations, 327~336, 1995.

33. S. Glasstone, *Textbook of Physical Chemistry,* New York: Van Norstrand and Co., 1946.

34. M. Knudsen, *The Kinetic Theory of Gases*, London: Methuen Publishers, 1934.

35. T.Ito, T.Kubota, A.Zukeran, T.Takashi, K.Shinkai, M.Miyamoto, and T.Yoshimochi, *Collection characteristics of submicron particles on electrostatic precipitator*, J. Inst. Elect. Install, Eng. Japan, Vol. 15 (2), 113~120, 1995.

36. C.Riehle and F.Loffler, *The Effective Migration Rate in Electrostatic Precipitator*, Aerosol Science Technology, Vol. 16 (12), 1288~1296, 1996.

37. M. Raphael, S. Rohani, and F. Soslski, *Isoelectric precipitation of sunflower protein in a tubular precipitator*, Can. J. Chem. Eng., Vol. 73, 470~483, 1995.

38. J.S.Chang, H.Thompson, P.C.Looy, A.A.Berezin, A.Zukeran, T.Ito, S.Jayaram, and J.D. Cross, *Control of trace elements in combustion flue gas by a corona discharge activated conditioning agent and electrostatic precipitators*, Proceedings of the 6th International conference on Electrostatic Precipitators, I.Berta, Ed. Budapest, Hungary: Tech. Univ. Budapest Press, pp.2~7, 1997.

39. A. Zukeran, J.S.Chang, A.A.Berezin, and T.Ito, *Control of ultrafine particles from incense smoke by an air cleaning electrostatic precipitator*, J. Aerosol Sci., Vol.28, suppl. 1, S289~S290, 1997.

40. J.S.Chang, *Electrostatic charging of particles*, Handbook of Electrostatic Processes, Editors: J.S.Chang, A.J.Kelly, and J. M. Crowley, New York: Marcel Dekker, ch.3, pp.39~50, 1995.

41. P. A. Lawless, T. Yamamoto, and Y. Otani, *Modeling of electrostatic precipitators and filters*, Handbook of Electrostatic Processes, Editors: J.S.Chang, A.J.Kelly, and J.M.Crowley, New York: Marcel Dekker, ch.22, pp.481~508, 1995.

42. S. Cristina and M. Feliazni, *Calculation of ionized fields in dc electrostatic precipitators in the presence of dust and electric wind*, IEEE Trans. Ind. Application, Vol.31, 1446~1451, 1995.

43. H. Bai, C. Lu, and C. L. Chang , *A model to predict the system performance of an electrostatic precipitator for collecting polydisperse particles*, J. Air Waste

Manage. Assoc., Vol. 45, 908~916,1995.

44. J. H. Davidson and P. J. McKinney, *EHD flow visualization in the wire-plate and barbed plate electrostatic precipitator*, IEEE Trans. Industrial Application, Vol. 27, 154~160, 1990.
45. L. Enliang, W. Yingmin, and J. A. Raper, *Study of gas velocity distribution in electrostatic precipitator*, Aerosol Science Technology, Vol. 12 (4), 947~952, 1990.
46. J. Somers, P. Caperan, J. Magill, K. Richter, S. Fourcaudot, P. Barranx, P. Lajarge, A. Rier, E. Franco De Sarabia, and N. Seyfert, *Verbesserung der Effektivetaet von elektrostatischen Abscheidern mittels Akustischer aerosol-Vorbehandlund*, Staub Reinhalt Luft, Vol. 54 (12), 451~454, 1994.
47. J. Silc and M. Tuma, *The influence of ultrasound on the agglomeration of fly-ash in exhaust*, Staub Reinhalt Luft, Vol. 54 (5), 183~185, 1994.
48. H. Aoyoma, J. S. Chang, T. Nakane, and K. Seya, *Effects of high intensity ultrasonics on the performance of electrostatic precipitators*, Proceedings of Japanese Sound Soc. 1993 Meeting, pp.1065~1066, 1993.
49. T. Watanabe, F. Tochikubo, Y. Koizumi, T. Tsuchida, J. Hautanen, and E. I. Kauppinen, *Submicron particle agglomeration by an electrostatic agglomeration*, J. Electrostatics, Vol. 34, 367~383, 1995.
50. J. Kildeso, V. K. Bhatia, L. Lind, E. Johnson, and A. Johansen, *An experimental investigation for agglomeration of aerosol in alternating electric fields*, Aerosol Science Technology, Vol. 23 (4), 603~610, 1995.
51. A. Zukeran, T. Ito, T. Takahashi, and H. Kawakami, *Effect of water on agglomeration and collection efficiency in electrostatic precipitator*, J. Inst. Elect. Install. Eng. Jpn., Vol. 16 (12), 1288~1296, 1996.
52. P. Shambaugh, and J. Todaro, *Natural gas and the environment*, Natural Gas 1998: Issues and Trends, Energy Information Administration (EIA) USA, 49~71,

1999.

53. J. S. Chang, *Theory of aerosol particle thermal deposition on an arbitrarily shaped body*, J. Aerosol Sci., Vol. 17 (3), 423~425, 1986.

54. J. S. Chang, K. Jogan, C. A. McLinden, P. C. Looy, and A. A. Berezin, *Unipolar charging of high resistive fly ash particles by a quadrupole cold*, J. Aerosol Science, Vol. 23, suppl. 1, S787~S790, 1992.

55. S. Yokawa, T. Shibata, and K. Nagakura, *Wet type electrostatic precipitator for iron and steel industries*, Proc. Inst. Electrostatics Jpn., Vol. 18 (5), pp.404~409, 1994.

56. T. Misaka, *Recent electrostatic precipitator technology*, Proc.IESJ96-1-4 Conf., pp.25~34, 1996.

57. T. Yagyu, Y. Tsuchiya, S. Onishi, and H. Katayama, *Recent electrostatic precipitation technology*, J. Mitsubishi-Juko-Giho, Vol. 35 (1), 70~73, 1996.

58. S. Jayaram, G. S. P. Castle, J. S. Chang, A. A. Berezin, P. C. Looy, R. Mangal, and M. S. Mozes, *Semipilot plant pulse energized coldprecharger electrostatic precipitator test for collection of moderately high resistivity fly ash particles*, IEEE Trans. Ind. Application, Vol. 32, 851~857, 1996.

59. G. Dinelli, V. Bogani, and M. Rea, *Enhanced precipitation efficiency of electrostatic precipitators by means of impulse energization*, IEEE Trans. Ind. Application, Vol. 27, 323~330, 1991.

60. P. Arendt and H. Kallman, *über den mechanisms der aufladung von nebelteilchen*, Z. Phys., Vol. 35, 421~441, 1925.

61. H. J. White, *Particle charging in electrostatic precipitation*, AIEE Trans., Vol. 70, 1186~1191, 1951.

62. R. Gunn, *Diffusion charging of atmospheric droplets by ions, and the resulting combination coefficients*, J. Meteorol., Vol. 11, 339~347, 1954.

63. A. T. Murphy, F. T. Adler, and G. W. Penney, *A theoretical analysis of the effects of an electric field on the charging of fine particles*, AIEE Trans., Vol. 78,

of an electric field on the charging of fine particles, AIEE Trans., Vol. 78, 318~326, 1959.

64. G. L. Natanson, *On the theory of the charging of microscopic aerosol particles as a result of capture of gas ions,* Soviet Phys. Tech. Phys., Vol. 5, 538~551, 1960.

65. J. W. Gentry, and J. R. Brock, *Unipolar diffusion charging of small aerosol particles,* J. Chem. Phys., Vol. 47, 64, 1967.

66. B. Y. H. Liu, K. T. Whitby, and H. H. S. Yu, *On the theory of charging of aerosol particles by unipolar ions in the absence of an applied electric field,* J. Colloid Interface Science, Vol. 23, 367~378, 1967.

67. J. W. Gentry, *Charging of aerosol by unipolar diffusion of ions,* J. Aerosol Science, Vol. 3, 65~76, 1972.

68. L. W. Parker, *Field charging theory for electrostatic precipitation of ultrafine particles,* Conference Record of the 68th Air Pollution Control Association, 75-02.2, 1, 1975.

69. J. S. Chang, *Theory of diffusion charging of arbitrarily shaped conductive aerosol particles by unipolar ions,* J. Aerosol Science, Vol. 12, 19~26, 1981.

70. J. R. Brock, *Noncontinuum unipolar charging of aerosols: the role of external electric fields,* J. Appl. Phys., Vol. 41, 1940~1944, 1970.

71. J. R. Brock, and M. S. Wu, *Field charging of aerosol particles,* J. Colloid Int. Science, Vol. 45, 106~114, 1973.

72. J. S. Chang, P. Beckwith, and J. D. Miller, *Unipolar charging of ultra-fine particles under an electric field,* J. Aerosol Science, Vol. 15, 270~273, 1984.

73. M. M. Pauthenier, and M. Moreau-Hanot, *Le charge des particules spheriques dans un champ ionise,* J. Phys. Radium (Paris), Vol. 3, 590, 1932.

74. B. Y. H. Liu, and A. Kapadia, *Combined field and diffusion charging of aerosol particles in the continuum regime,* J. Aerosol Science, Vol. 9, 227, 1978.

75. Matts, S., and Ohnfeldt, *Efficient gas cleaning with SF electrostatic precipitator,* Flakten, 64, 1963.

76. A. Zukeran, P. Looy, A. Chakrabarti, A. A. Berezin, S. Jayaram, T. Ito, and J.S.Chang, *Collection efficiency of ultrafine particles by an Electrostatic precipitator under DC and pulse operating modes*, IEEE transactions on industry applications, Vol.35 (5), 1184~1191, Sept/Oct. 1999.

77. S. Masuda, and A. Mizuno, *Light measurement of back discharge*, J. Electrostatics, Vol. 2, 375, 1976.

78. S. Masuda, and A. Mizuno, *Initiation condition and mode of back discharge*, J. Electrostatics, Vol. 4, 35, 1977.

79. S. Masuda, and A. Mizuno, *Flashover measurement of back discharge*, J. Electrostatics, Vol. 4, 215, 1978.

80. S. Masuda, *Resistivity and back corona*, Proceedings of International Conference on Electrostatic Precipitation, California: Monterey, pp.131~161, 1981.

81. J. D. Basset, K. Akutsu, and S. Masuda, *A preliminary study of reentrainment in an electrostatic precipitator*, J. Electrostatics, Vol. 3, 311, 1977.

82. J. P. Gooch, and G. H. Marchant, *Electrostatic precipitator rapping reentrainment and computer model studies*, FP-792, Electric Power Research Institute, Palo Alto, CA, 1978.

83. N. Plaks, *The SUPER ESP-ultimate electrostatic precipitation*, Ninth Particulate Control Symposium, Williamsburg, Virginia, 1991.

84. A. Zukeran, T. Ito, T. Takahashi, K. Shinkai, *The study of agglomeration and collection efficiency in electrostatic precipitators*, Proceedings of 6th international conference on Electrostatic Precipitation, VI ICESP, Budapest Hungary, pp.359~364, 18-21 June, 1996.

85. Yamamoto T., and H. R. Velkoff, *Electrohydrodynamics in an electrostatic precipitator*, J. Fluid Mechanics, Vol. 108, 1, 1981.

86. Leonard G. L., M. Mitchner, and S. A. Self, *An experimental study of the electrohydrodynamic flow in electrostatic precipitators*, J. Fluid Mechanics, Vol.

127, 123, 1981.

87. Okubo T., H. Yano, K. Nomoto, and T. Adachi, *Analysis of flow for the wire-plate electrode geometry,* Proceedings of the Ninth Annual Meeting of the Institute of Electrostatics, Japan, pp.17~20, 1985.

88. Atten P., F. McCluskey, and A. Lahjormi, *Electrohydrodynamic simulation of electrostatic precipitation,* IEEE Trans. On Industry Applications, IA-23, 705, 1987.

89. IEEE DEIS EHD Technical Committee Standard Subcommittee Report, *Recommended International Standard for Dimensionless Parameters Used in Electrohydrodynamics*, IEEE Trans. Dielectric & Electrical Insulations, Vol. 10, 3~6, 2003.

90. E. Bonjour, J. Verdier, and L. Well, *Electroconvection Effects on Heart Transfer,* Chem. Eng. Progress, Vol. 58, 63~66, 1962.

91. R.D.Marcus, L.S.Leung, G.E.Klinzing, and F.Rizk, Pneumatic Conveying of Solids, New York: Chapman & Hall, 1990.

92. S. L. Soo, Particulates and Continuum: Multiphase Fluid Dynamics, New York: Hemisphere, 1989.

93. Rex Klopfenstein Jr., *Air velocity and flow measurement using a pitot tube*, ISA Transactions, Vol. 37 (4), 257~263, 1998.

94. H. Preston-Thomas, *The international temperature Scale of 1990 (ITS-90),* Metrologia 27, 3-10, 107.

95. E. Wickers, *The history of Pt-67*, Temperature: Its measurement and control in science and industry; Vol. 3, Editor: C. M. Herzfeld, New York: Reinhold Publishing Corp., Part 1, pp.259~262, 1962.

96. TSI Corp., Particle instruments instruction manual: Model 3010 Condensation Particle Counter, P/N 1933010 Revision F, Aug. 2002.

97. Ed Griffith, *ESEM: An introduction and discussion to the technology and its applications.* ESEM Product Forum. Jan. 28. 1999.

applications, ESEM Product Forum, Jan. 28, 1999.

98. H. E. Hesketh, *Understanding and Controlling Air Pollution,* Ann Arbor, Michigan: Ann Arbor Science Publishers Inc., 1974.
99. D.Brocilo, J.S.Chang and R.D.Findlay, *Modeling of electrode geometry effects on dust collection efficiency of wire-plate electrostatic precipitators,* Proceedings of 8th International Conference on Electrostatic Precipitation, Vol. I, pp.1~18, 2001.
100. J. S. Chang and A. Watson, *Electromagnetic hydrodynamics,* IEEE Trans. DEI, Vol. 1, 871~895, 1994.
101. B. E. Launder, and D. B. Spalding, *The numerical computation of turbulent flows,* Computer Methods in Applied Mechanics and Engineering, Vol. 3, 269~289, 1974.
102. S. Park, L. Guan, G. D. Harvel, and J. S. Chang, *Numerical simulation of dust flow separation type electrostatic precipitations,* (to be submitted), 2005.
103 M. Hood, and W. Sweet, *Energy policy and politics in China,* IEEE Spectrum, Vol. 36, 34~38, 1999.
104 Natural Resources Canada, Energy efficiency trends in Canada: 1990-2002, Cat. No. M141-1/2002, ISBN 0-662-68082-0, 2004.

APPENDIX A

THE NUMERICAL ANALYSES OF THE DUST FLOW SEPARATOR TYPE ELECTROSTATIC PRECIPITATOR

It is discovered that the particles emitted from the natural gas combustion is approximately in the ultrafine size range from 0.017μm to 0.3μm [7] based on measurement. It is known that the present existing devices cannot treat particles in this range very efficiently as reviewed in Chapter 2. Therefore, a new type DFS-ESP (dust flow separator type electrostatic precipitator) is proposed and developed for the purpose of improving the collection efficiency of ultrafine particles.

The concept of DFS-ESP is described in this Appendix, followed by the numerical modelling for DFS and ESP by FEMLAB and MESP code respectively, for the purpose of performance estimation and optimization.

1. PRINCIPLE OF DUST FLOW SEPARATOR TYPE ESP

There are two important properties of particles emitted from natural gas combustion based on the discussion in chapter 2:

(a). size distributed in the ultrafine range;

(b). diluted gas-particle exhaust.

Therefore, the conceptual DFS-ESP is proposed, as shown in Figure A.1. Natural gas combustion exhaust with submicron to ultrafine particles enter in the upstream of DFS-ESP, pass through an optional precharger, experience the particle separation in DFS

section, the concentrated PM stream is separated to ESP section to be charged and collected, and clean gas exits the ESP, re-joins in the PM free gas in the main stream, and exhaust to the next device for toxic gas control. Mechanisms with this system are described in Figure A.2.

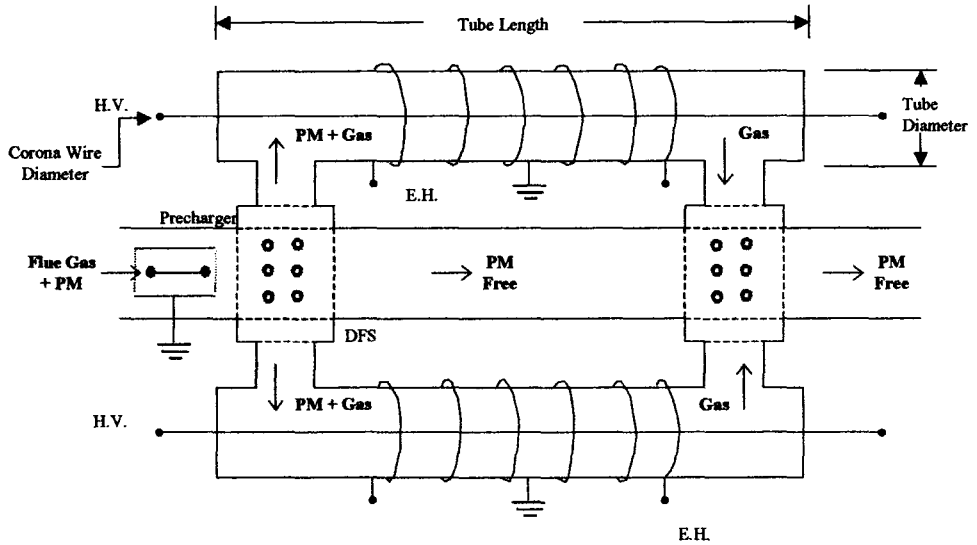

H.V. : High Voltage
E.H. : Electrical Heating
DFS : Dust Flow Separator

Figure A.1 Schematic of the conceptual design of DFS-ESP

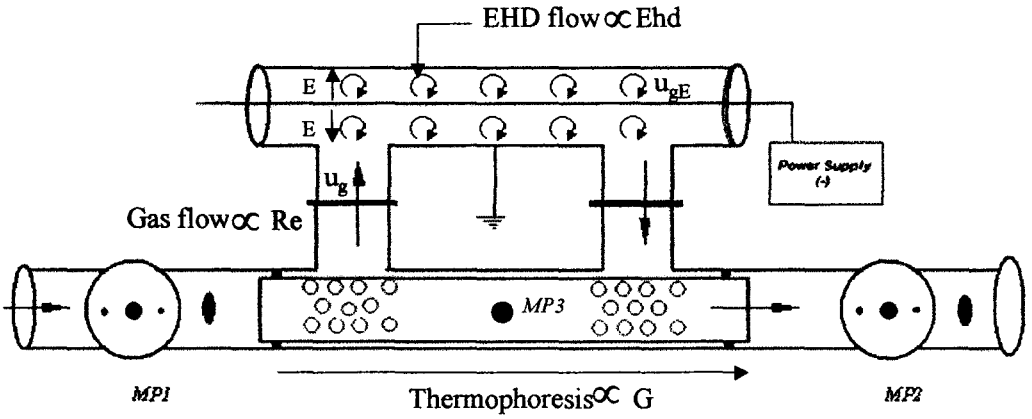

$$Ra\,\vec{u}_g\cdot\tilde{\nabla}n-\tilde{\nabla}^2 n\pm F_E\,\tilde{\nabla}\cdot(n\vec{\xi})-G\tilde{\nabla}\cdot(n\tilde{\nabla}\theta)=0$$

convective *diffusion* *mobility* *thermophoresis*

Figure A.2 Schematic of DFS-ESP and Particle Transportation Mechanism

The dust flow separator allows for a minor flow to pass through the ESP containing a higher concentration of particles than in the original gas, while the remainder of the flow bypasses the ESP with a low particle concentration. The perforations arranged in a regular matrix distribution generate sudden pressure expansion in the region where the ESPs are connected, which might cause turbulence for the inlet flows with low *Re*, and particles transient stagnating and migrating to ESP branch by diffusion, convection, and/or thermophoresis.

Separated particles in the ESP would be further discharged, mainly the diffusion charge mechanism for this size range, and collected to the inner wall of the collecting electrode. An ESP is optimized by MESP code to achieve the highest possible collection efficiency. It would be the oxidization by plasma or incineration by electrical heater that is employed to remove the collected dust.

For such a design, an ESP can work under a less disturbed laminar flow circumstance, so that the traditional heavy dust loading problem could be eliminated; the symmetrical system design could decrease the influence by potential backpressure; and the re-entrainment problem would be furthest controlled by instant particles removing within the system.

For preliminary performance evaluation and optimization of this DFS-ESP, numerical modelling is performed.

2. Numerical Analyses of DFS-ESP

Numerical models are set up for both the flow separator and the ESP independently. The flow and pressure distribution within the whole system are simulated by FEMLAB and FLUENT [102], while the particle collection efficiency versus different operation conditions is simulated by the MESP code [99].

2.1 Flow Modelling

2.1.1 FEMLAB Modelling and Results

A lot of previous research has been done on modeling of the transport of particles in different systems with different geometries. For example, modeling of the transport of radioactive corrosion products in a vertical annular pipe [1], which is used for prediction of particle distribution and design in the primary loop of a nuclear power unit; ESP optimization codes for control of fine particulate in industrial flue gas [2], in which the physical foundations of the fluid flow coupling with electrical parameters such as electrohydrodynamic (EHD) induced secondary flow, onset of turbulence, and charged particle induced secondary flow, and also their coupling with the fine particle transport processes; numerical modeling of diffusion and sedimentation of Aerosol particles from laminar flow in inclined channels developed the theory of the diffusion and sedimentation of aerosol particles from Poiseuille flow in channels [3].

Different with the above works, this project deals with the ultrafine particles distribution in a horizontal system (Figure A.1), therefore, only convection, and diffusion were considered as the particle separation mechanisms for the overall DFS-ESP system

except the ESP electrical effect. In a FEMLAB based environment, modeling work has been done within a proper range, i.e., the dimensionless diffusion Reynolds number (or Rayleigh Number) $Ra<=10^3$. *(Ra=Re*Sc)*

Several assumptions have been made before modeling, which are [1,2,3]:

- The total volume of the particles is much smaller than that of the channel, therefore the interaction between individual particles may be neglected and the Stoke's law of force between the fluid and particles is valid;
- The fluid has constant-property (e.g., viscosity and density) and incompressible (i.e., constant density or $\nabla \bullet V_g = 0$), so that no frictional dissipation exist and is suitable for *Navier-Stokes Equation*;
- Particle inertia can be negligible due to the ultrafine sizes and super small mass of the particles' physical properties;
- The particle size and its mean free path are much smaller than the channel width;
- The thermophoresis of the particles can be neglected;
- System is under steady state and laminar gas flow is used.

Based on above assumptions, the governing equation can be written as [2,4]:

$$U_g \cdot \nabla N_p - D_p \nabla^2 N_p = 0 \qquad (A.1)$$

where $U_g = U_{max} \cdot [1-(\frac{r}{R})^2]$ is the gas flow velocity; D_p is the particle diffusion coefficient; and N_p is the particle density. The first term of above equation corresponds to

a convection transport, while the second term is for particle diffusion. Above particle transportation equation is coupled with the incompressible *N-S equation* in FEMLAB.

$$\rho_g \frac{DV_g}{dt} = -\nabla P + \mu_g \nabla^2 V_g \tag{A.2}$$

Assuming that initially the particle density is uniformly distributed along the radial direction and for $z=0$ (system inlet) we have a source of particle injection in, the boundary conditions as follows:

- n_p=1 at $z=0$ (system inlet) for all radial distance *(r)*;
- n_p=0 for all surface walls;
- $dN_p/dz=0$ at z=1 (system outlet).

where $n_p = \frac{N_p}{N_0}$.

The characterized geometry is set up in FEMLAB as shown in Figure A.3. Optimized geometry results from the modeling are shown in Table A.1.

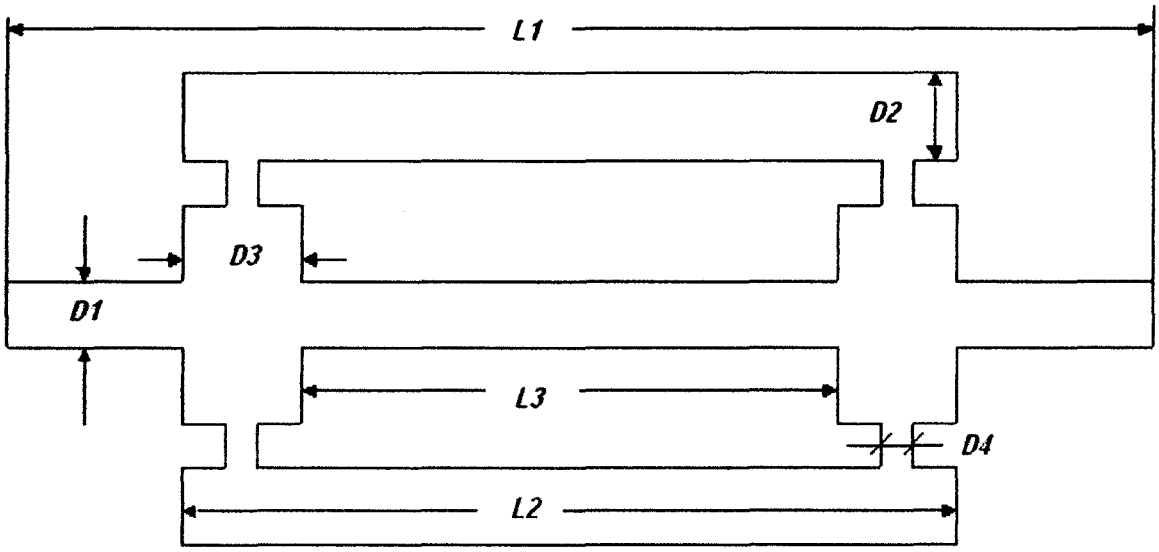

Figure A.3 Geometrical size of FS numerical modeling with FEMLAB

Table A.1 Optimized geometry of DFS-ESP

L1	*L2*	*L3*	*D1*	*D2*	*D3*	*D4*
0.53	0.34	0.027	0.02	0.03	0.035	0.009

Note: all dimensions are in meters

Modeling results for particle separation and system pressure drop are shown in Figures A.4 to A.7. Figure A.4 shows the typical modeling result of particle distribution in such a system when Schmidt number equals to 100 for Reynolds number at 10, which give us a direct impression on the particle separation and gas velocity distribution by DFS. Figure A.5 is the corresponding quantitative analysis result for the velocity distribution along the radial direction for main stream and ESP branch (locations indicated in Figure

A.4) for different total inlet flow (different *Re*), from which we can conclude that more gas flow are separated to branch as increasing inlet total flow rate (*Re*).

Particles separation behavior with *Re* and *Sc* is summarized in Figure A.6. It shows a decreasing trend with increasing Sc number and an increasing trend with increasing Re number, which suggests that particle diffusion is the dominant mechanism for the separation by DFS.

As indicated in Figure A.7, the pressure drop over the system is well distributed and in the order of $6x10^{-4}$ *Pa* for Re=1. This indicates that pressure drop is not expected to be a concern for this device.

Unfortunately, the modeling cannot be performed with either larger Re number (higher than 1000) or larger Sc number due to program convergence issues within FEMLAB. For this reason, the FLUENT code is applied to carry out a much more accurate prediction.

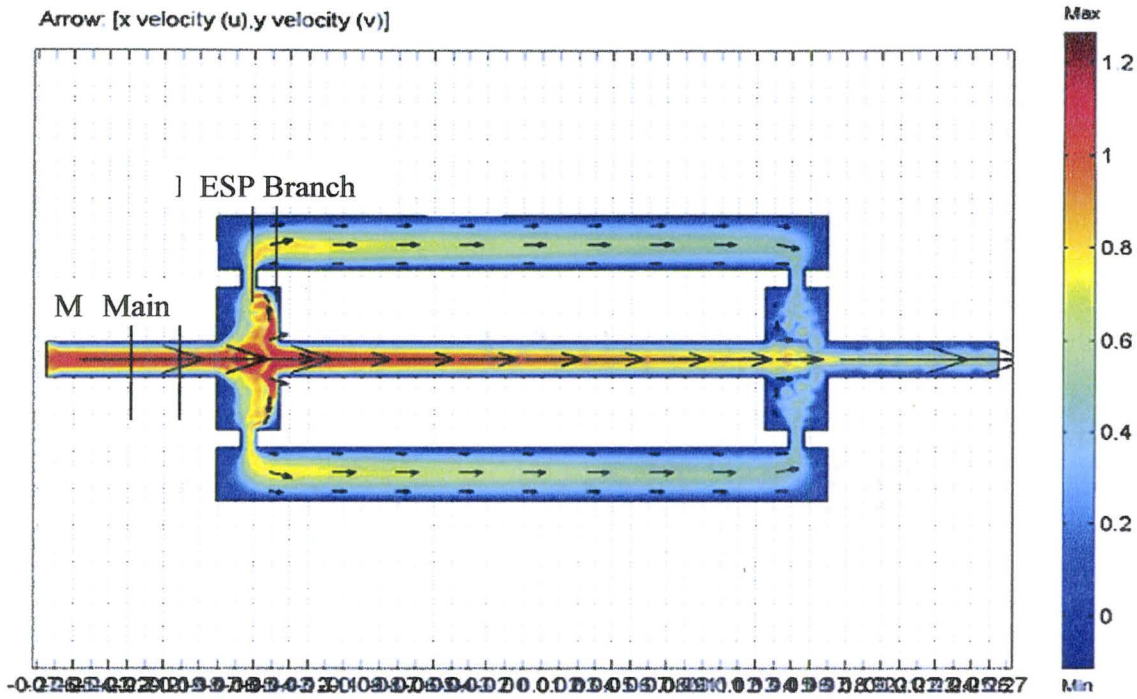

Figure A.4 FEMLAB modelling of particle and velocity distribution in the DFS-ESP for Re=10 and Sc=100

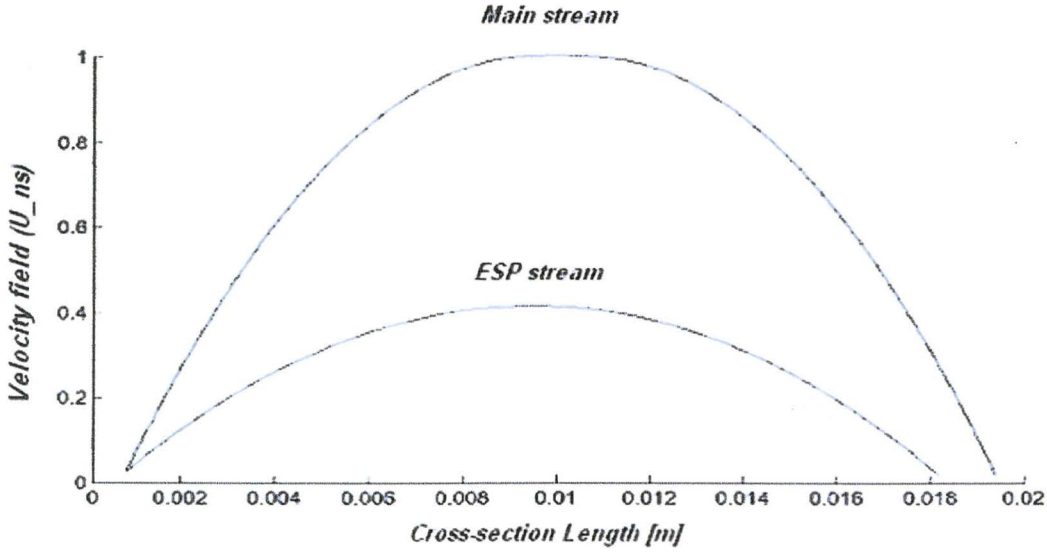

Figure A.5 FEMLAB modelling of cross-section velocity distribution profile For Re=10 and Sc=100

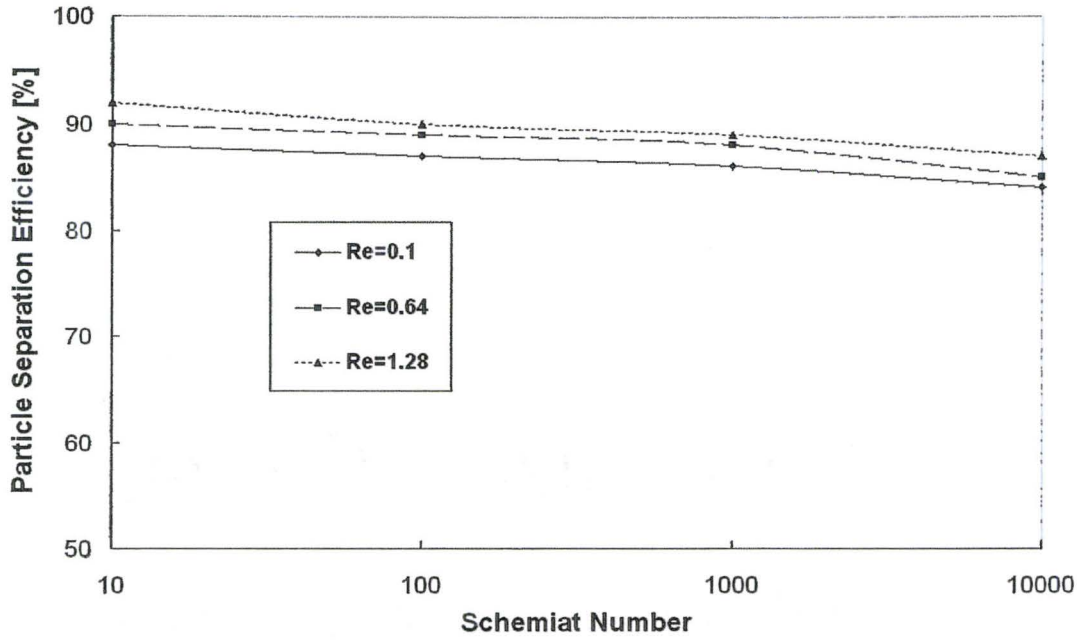

Figure A.6 FEMLAB modeling results of particle separation efficiency as a function of Reynolds number and Schmidt number

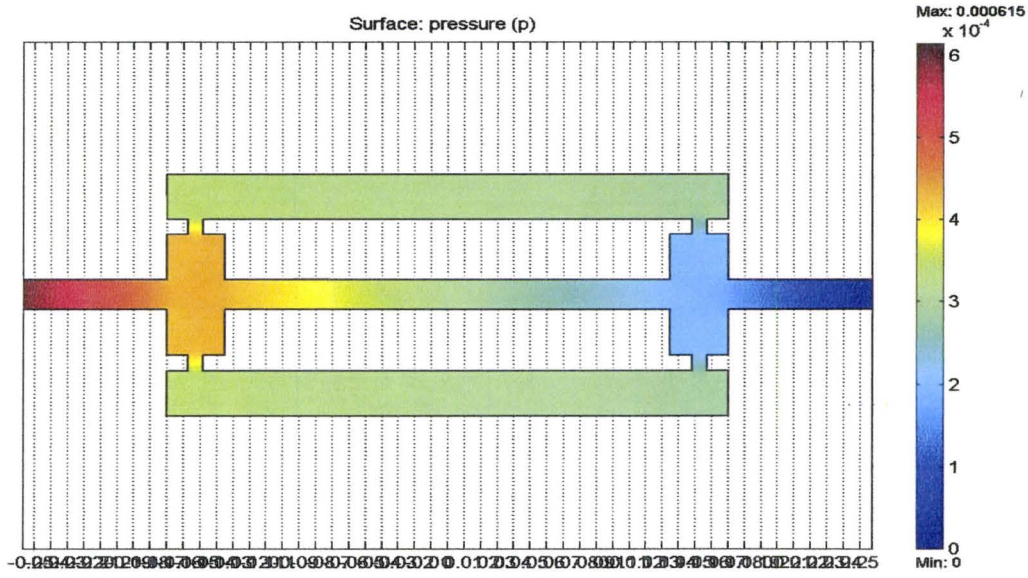

Figure A.7 FEMLAB modelling of the pressure drop over the DFS-ESP system for *Re*=1

2.1.2 Flow Modelling by FLUENT

FLUENT is the world's largest provider of computational fluid dynamics (CFD) software. FLUENT software is used for simulation, visualization, and analysis of fluid flow, heat and mass transfer, and chemical reactions. It is a vital part of the computer-aided engineering (CAE) process for companies around the world and is deployed in nearly every manufacturing industry.

The governing equation used in current DFS-ESP application is Launder and Spalding [101] model (i.e. standard $k-\varepsilon$ model) shown in Equation A.3~A.9 as follows:

$$\partial u_i / \partial x_i = 0 \tag{A.3}$$

$$\frac{\partial \rho u_j u_i}{\partial x_j} = -\frac{\partial p}{\partial x_i} + \frac{\partial}{\partial x_j}[\mu(\frac{\partial u_i}{\partial x_j} + \frac{\partial u_j}{\partial x_i}) - \rho\overline{u_i u_j}] \tag{A.4}$$

$$-\rho\overline{u_i u_j} = \mu_t(\frac{\partial u_i}{\partial x_j} + \frac{\partial u_j}{\partial x_i}) \tag{A.5}$$

$$\mu_t = C_\mu \rho k^2 / \varepsilon \tag{A.6}$$

$$\frac{\partial \rho u_i k}{\partial x_j} = \frac{\partial}{\partial x_j}(\frac{\mu_{eff}}{\sigma_k} \cdot \frac{\partial k}{\partial x_j}) + G - \rho\varepsilon \tag{A.7}$$

$$\frac{\partial \rho u_j \varepsilon}{\partial x_j} = \frac{\partial}{\partial x_j}(\frac{\mu_{eff}}{\sigma_\varepsilon} \cdot \frac{\partial \varepsilon}{\partial x_j}) + C_1 \frac{\varepsilon}{k} G - C_2 \rho \frac{\varepsilon^2}{k} \tag{A.8}$$

$$G = -\rho\overline{u'_i u'_j} \frac{\partial u_i}{\partial x_j} \tag{A.9}$$

where G is generation of turbulent kinetic energy, μ_{eff} is the effective viscosity coefficient, μ_t is the turbulent viscosity, k represents turbulent kinetic energy, and ε the turbulent dissipation. Several constants in equations are as follows: C_μ=0.09; C_1=1.44; C_2=1.92; σ_k=1.0; and $\sigma_\varepsilon = 1.3$.

Boundary conditions are set up as follows:

- Inlet velocity is uniform, i.e., $u_j = u_0$;
- Centerline follows Neumann boundary conditions, i.e., symmetric boundary conditions;
- Exit pressure is set as atmosphere pressure, i.e., 1atm;
- None slip boundary condition is set for all surface walls, i.e., $u = 0$.

The geometry of DFS-ESP FLUENT model is set the same as the real experiment scale to be able to be compared with experiment results. Geometry and grid of model are shown in Figures A.8 and A.9. Figure A.10 shows a typical modeling result for system pressure distribution of DFS-ESP with 7Nm^3/h total inlet flow. The velocity profile for 7Nm^3/h inlet flow within the DFS-ESP is shown in Figure A.11. A detailed examination of flow profile at flow separator section for 7Nm^3/h total inlet flow is shown in Figure A.12. It shows the turbulent flow re-circulation phenomena at flow separator section in Figure A.12. The quantitative analysis of velocity distribution and pressure drop of overall system is performed, and the results are shown in Figures A.13 to A.16. Figure A.17 shows the analyzed results of the ratio of flow separated to ESP branch to total inlet flow

versus total inlet flow. The comparison between experimental results and FLUENT modeling is presented in Chapter 4.

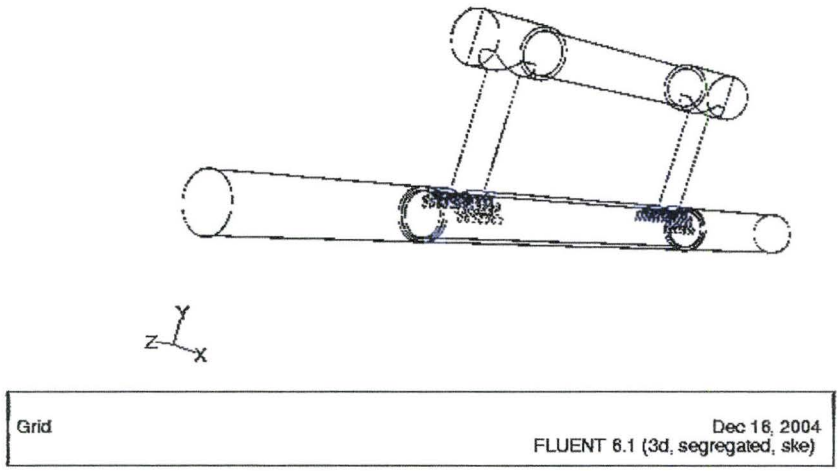

Figure A.8. Geometry set-up of DFS-ESP FLUENT model

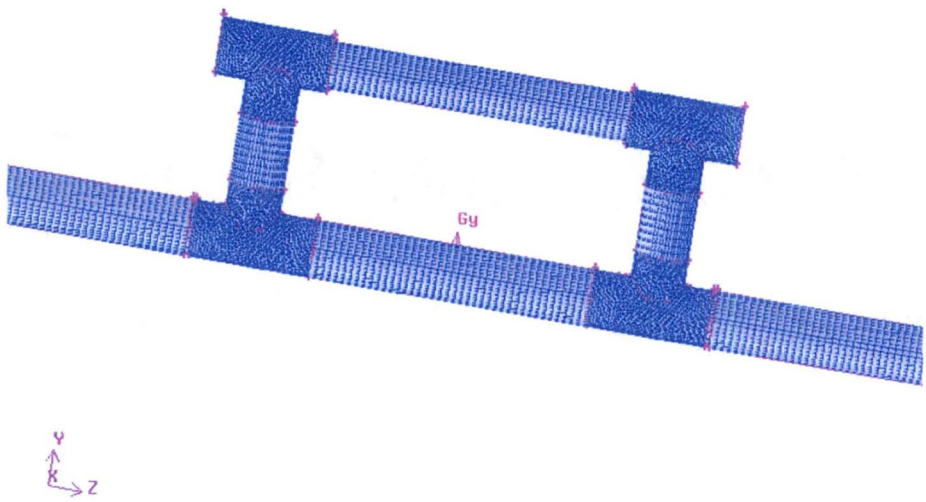

Figure A.9. Meshing of the model

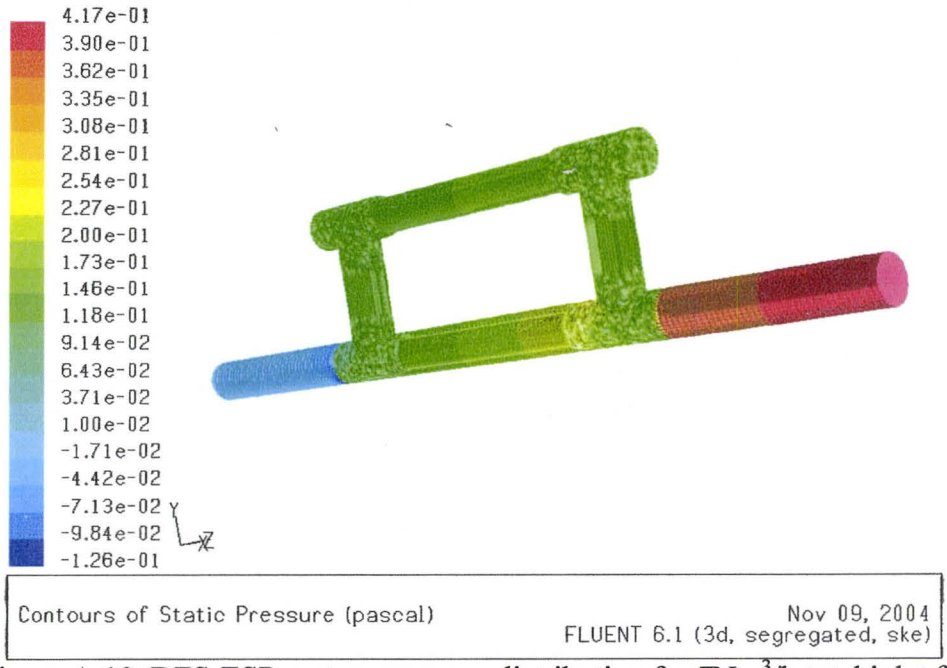

Figure A.10. DFS-ESP system pressure distribution for 7Nm^3/h total inlet flow

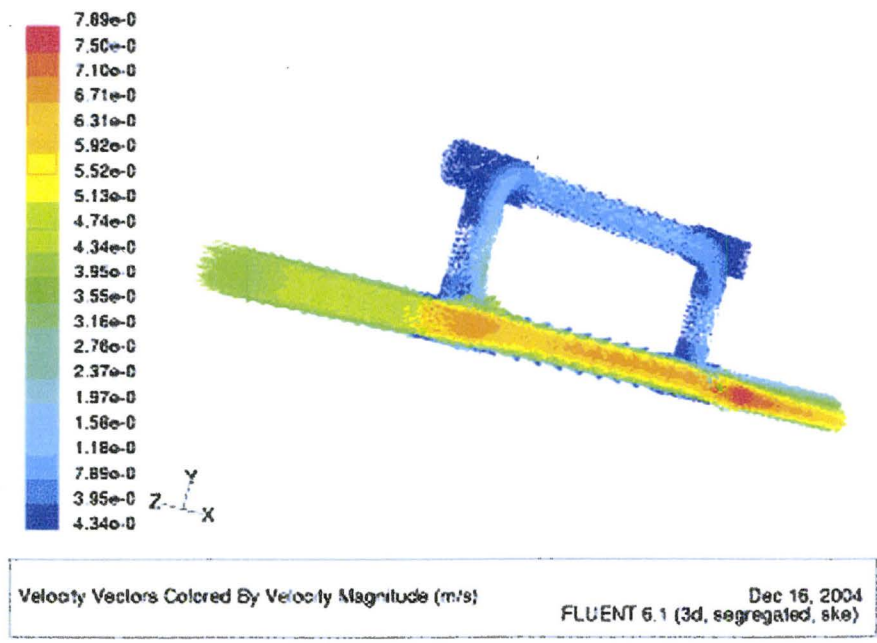

Figure A.11. Velocity profile within DFS-ESP for 7Nm^3/h total inlet flow

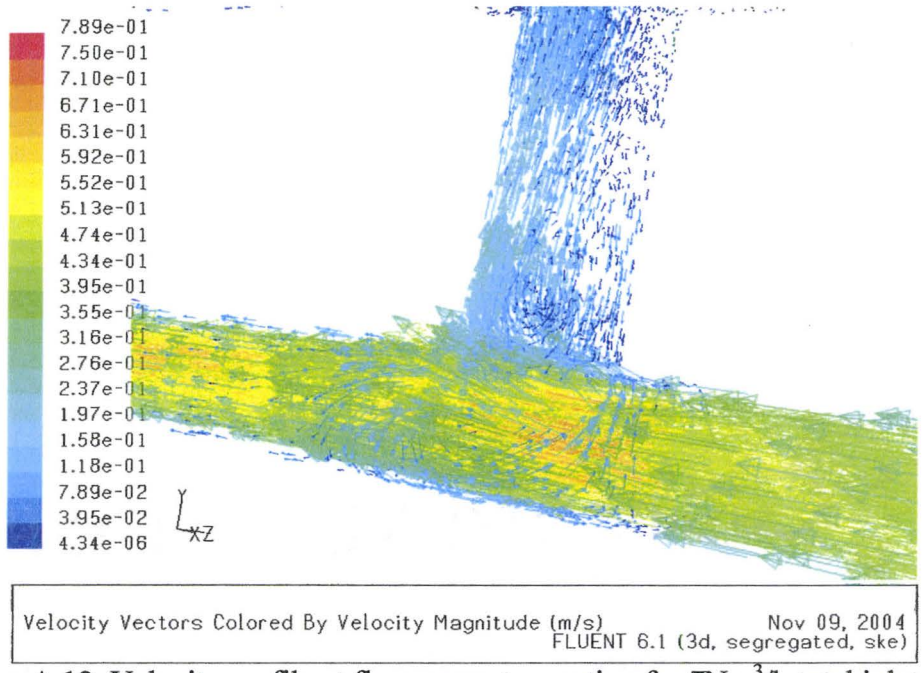

Figure A.12. Velocity profile at flow separator section for 7Nm^3/h total inlet flow

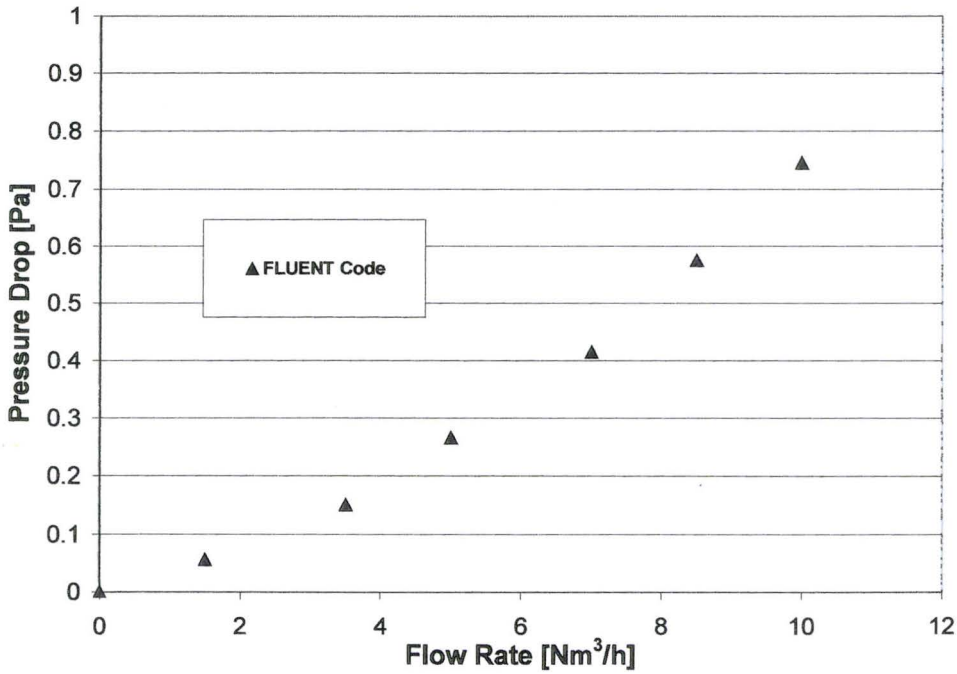

Figure A.13 Pressure drop prediction across the DFS-ESP by FLUENT code without insert

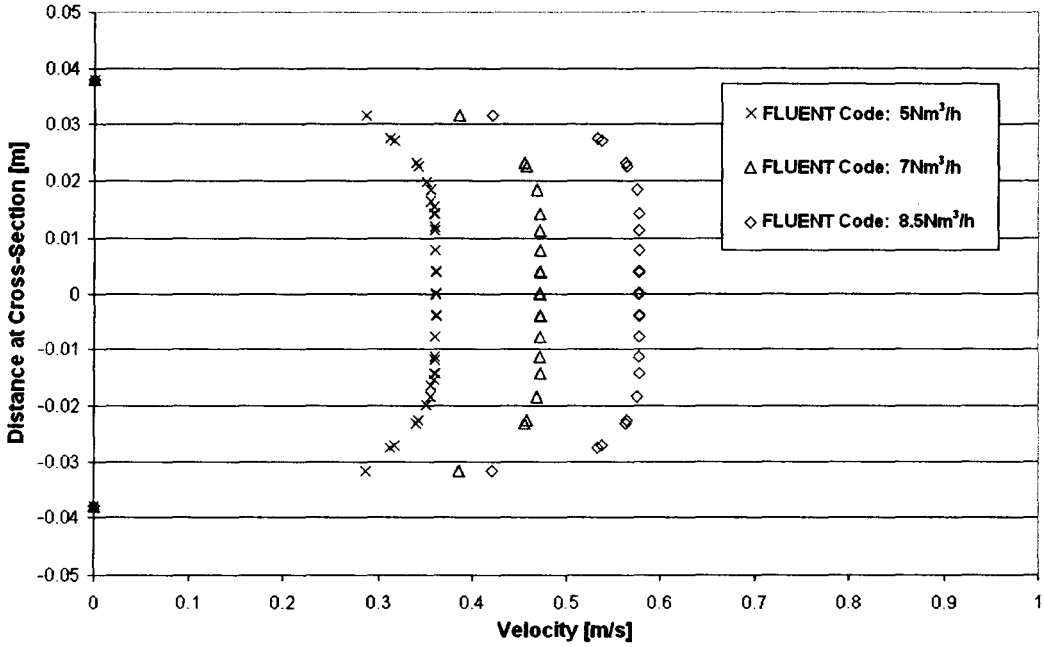

Figure A.14 Prediction of velocity profile for MP1 at 5, 7 and 8.5Nm^3/h total inlet flow by FLUENT code

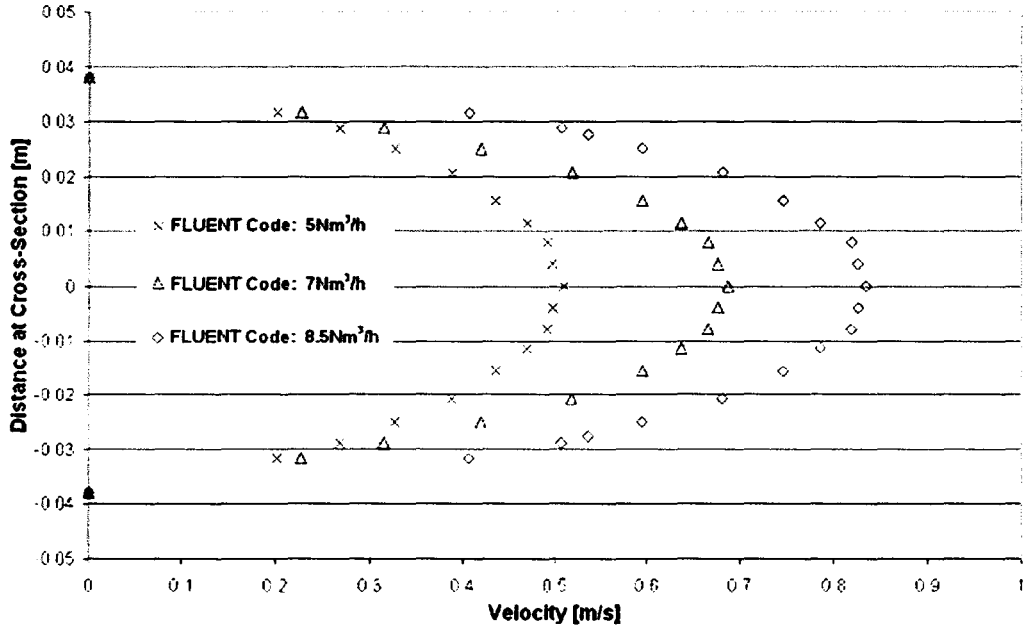

Figure A.15 Prediction of velocity profile for MP2 at 5, 7 and 8.5Nm^3/h total inlet flow by FLUENT code

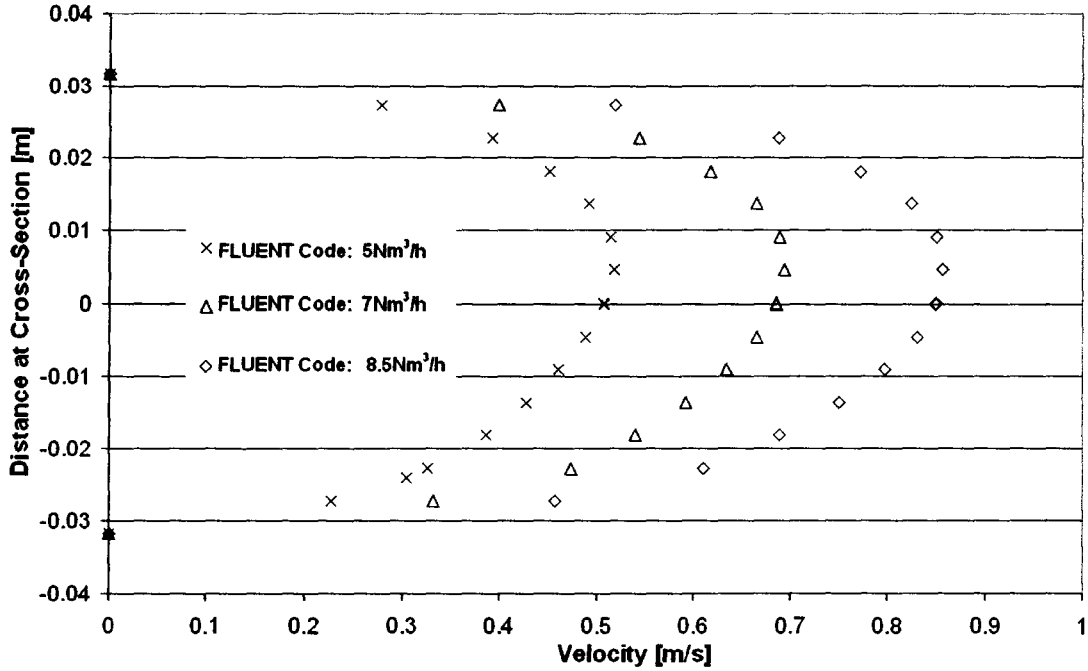

Figure A.16 Prediction of velocity profile for MP3 at 5, 7 and 8.5Nm^3/h total inlet flow by FLUENT code

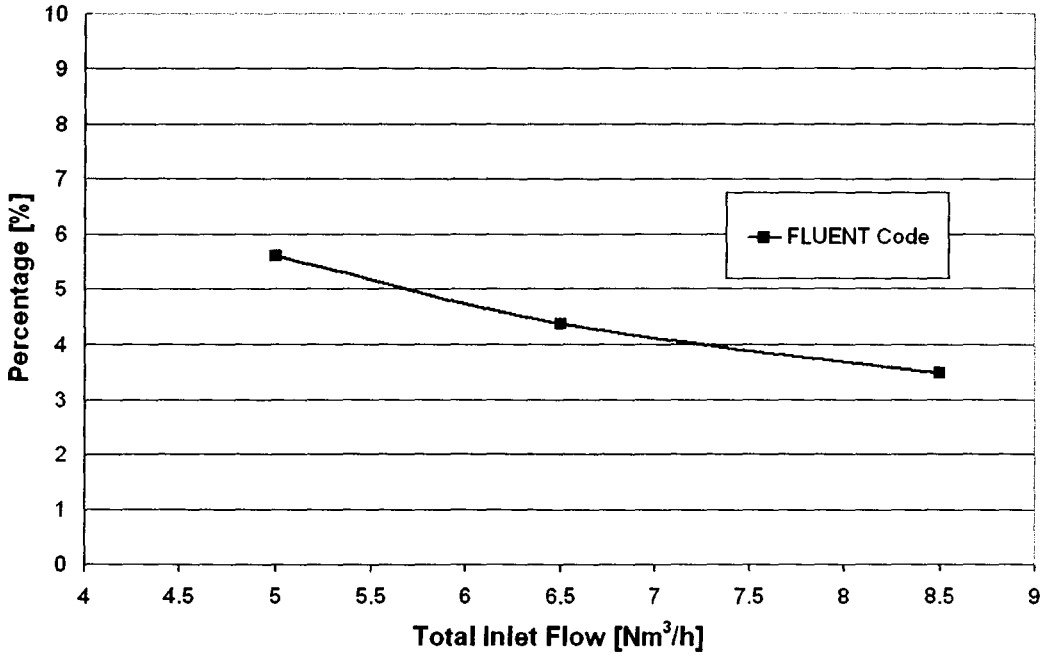

Figure A.17 Prediction of flow separation ratio (Q_{branch}/Q_{total}) by FLUENT code

3.2.2 ESP Optimization with MESP

A prediction of dust particle collection efficiency model by various geometry electrostatic precipitators, was developed by Chang et al., i.e. MESP (Multidimensional ESP) computer code [4]. The wire-pipe and wire-plate type ESP with the various electrode geometry effect can be analyzed for detail current-voltage characteristics, volume-averaged electric field and ion density via multi-dimensional simulation of the electric field and ion density profiles, and the ESP dust collection efficiency. It can solve parameters along the radical direction, and then upwind finite differencing is applied to calculate along the axial direction. The ion and neutral particle density distributions can be obtained by solving the transport equation for desired species, including the convective transport due to the gas flow, transport due to the ion diffusion and ion drift due to the electric field.

$$\overrightarrow{U_g} \cdot \nabla N_j \pm \nabla \cdot (\mu_j N_j \nabla V) - \nabla \cdot (D_j \nabla N_j) = \pm \sum^{n} k_j N_j N_d \qquad \text{(A.10)}$$

Denotation g represents gas; j corresponds to the interested species, either ion (i) or neutron dust particle (d); and k is the particle surface charging rate.

The ESP charging mechanisms include diffusion and field charging which are implemented based on the Knudsen number of particular dust particle diameter for a wide range of dust sizes (10^{-3} to 10^{2} μm). As discussed in previous chapter, particle size larger than 10μm is dominant by field charging, particle size smaller than 0.1μm by diffusion charging, and particle size in between by a combination of these two mechanisms.

The flow chart of MESP code is shown in Figure A.18.

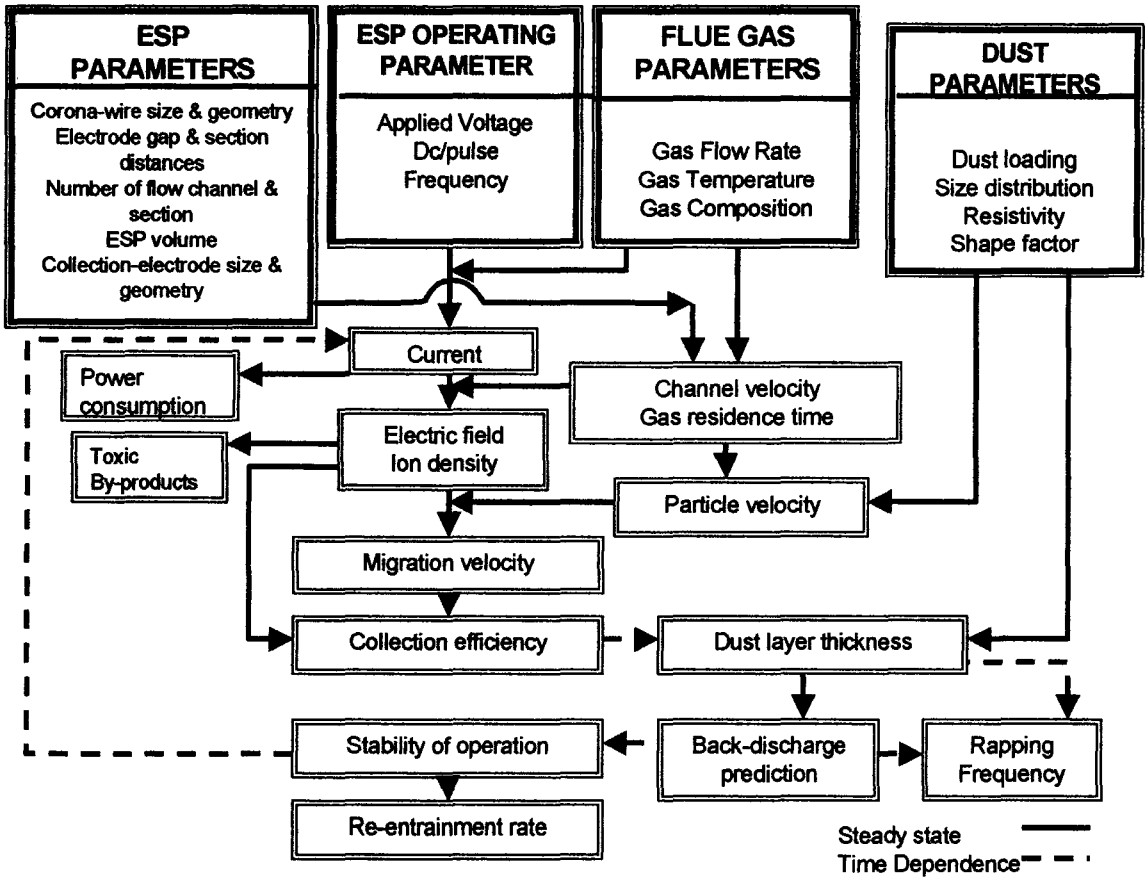

Figure A.18 Flow chart for MESP code [99]

The modeling is performed for wire-pipe type ESP. Main input characteristic parameters are tested, such as ESP geometry (corona wire diameter, pipe length and diameter), particle size (0.01 to 0.1μm), natural gas exhaust flow rate and system operating temperature. The sensitivity analyses based on the one-dimensional modeling results are shown in the Figures A.19~A.23.

From the sensitivity analysis by MESP code, we can conclude:

- The collection efficiency increases with increasing tube length. However, with η more than 90%, tube length is limited to about 1m due to space limitations;
- The collection efficiency increases with decreasing the tube diameter. However, to ensure a low pressure drop system, a tube diameter is tested no less than 2.54 cm;The collection efficiency increases with increasing the corona wire diameter. However, wire diameter cannot be too large to suppress the current density to be too small;The collection efficiency increases with increasing the applied voltage. However, sparking, power consumption, and power supply limitations have to be considered;The collection efficiency increases with decreasing the gas flow rate. Thus, the greatest number of tubes possible should be considered to minimize the flow rate;The collection efficiency decreases with increasing the gas temperature. Therefore gas temperature should be minimized.ESP is performed more efficient for particles with larger diameter.

Based on above sensitive analysis, the geometry of ESP is optimized for the existing experiment rig as listed in Table A.2.

Table A.2 Geometry of Experiment ESP

d_{ce} [mm]	L_{ce} [mm]	d_{de} [mm]
63.5	432	0.7

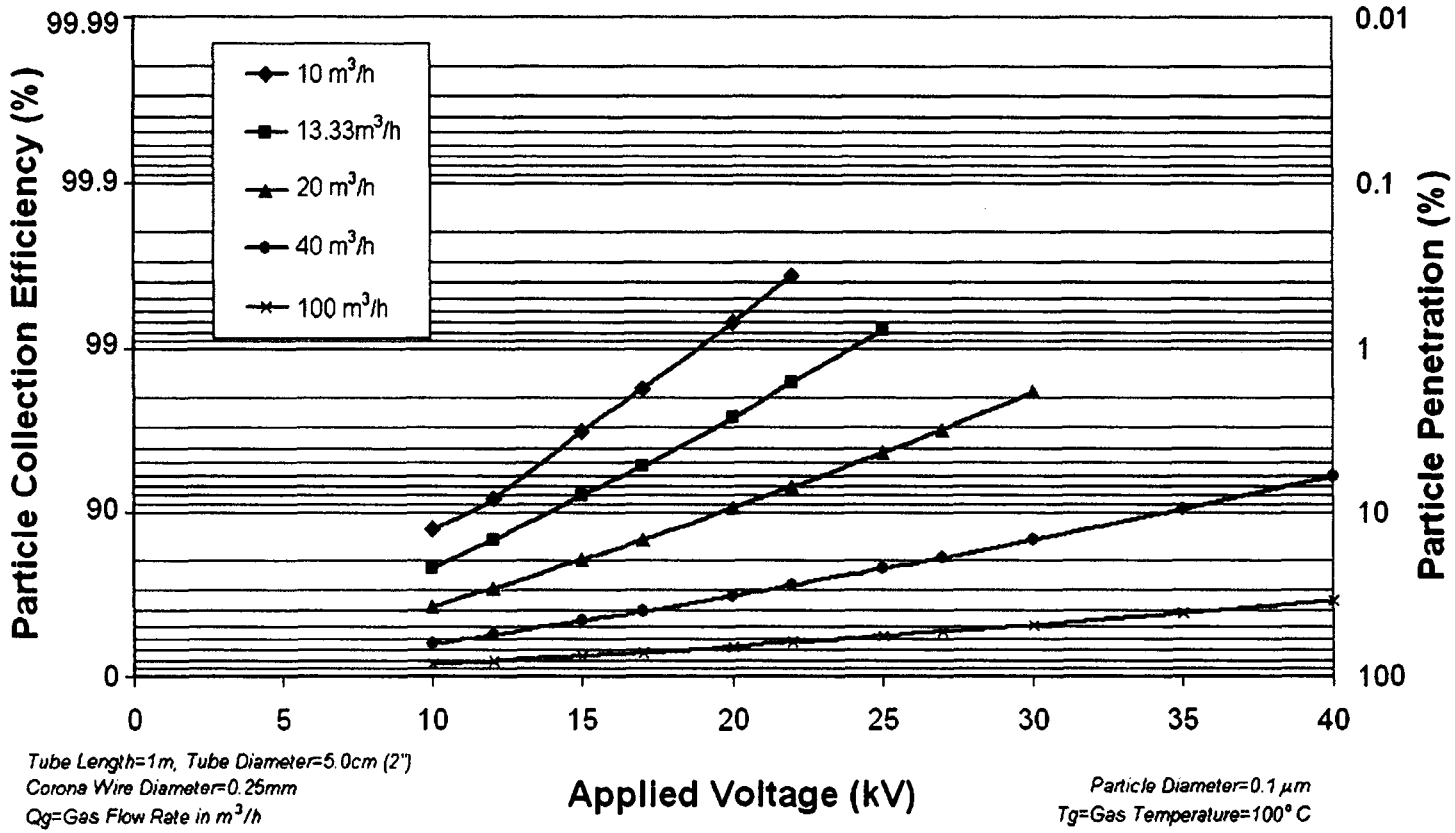

Figure A.19 Particle collection efficiency as functions of applied voltage, for various exhaust flow rates

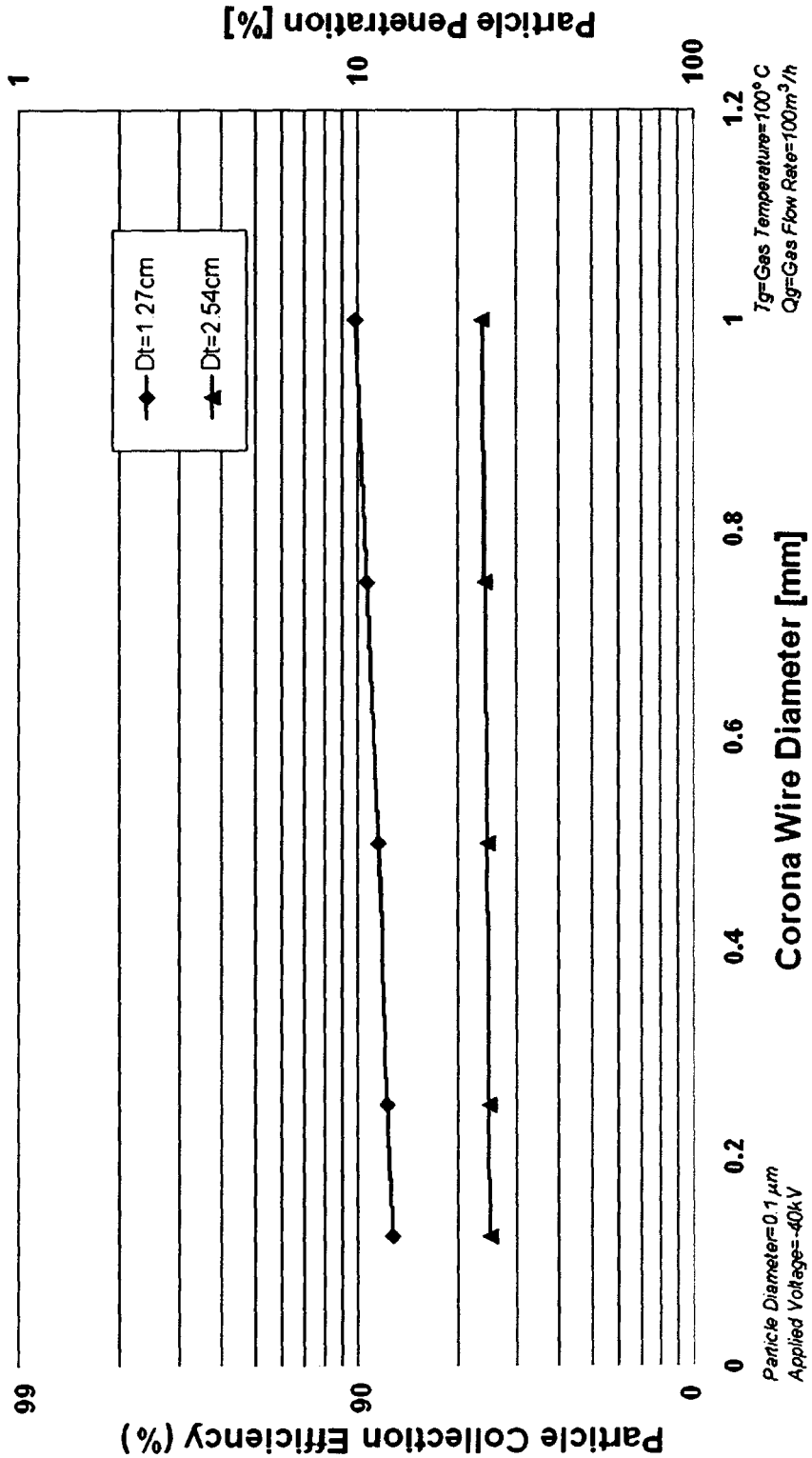

Figure A.20 Particle collection efficiency as functions of corona wire diameter for various tube diameters

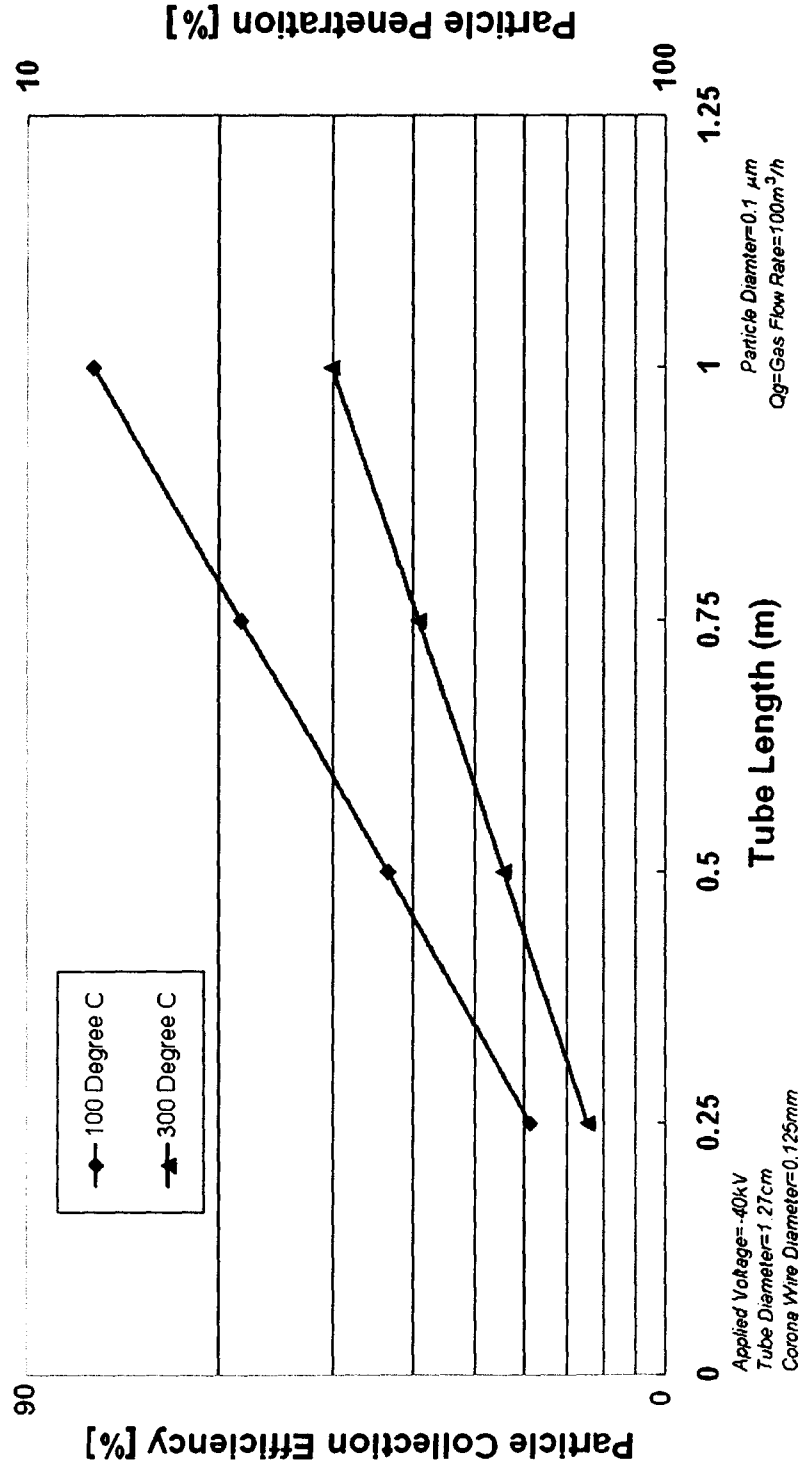

Figure A.21 Particle collection efficiency as functions of ESP tube length for various system operating temperatures

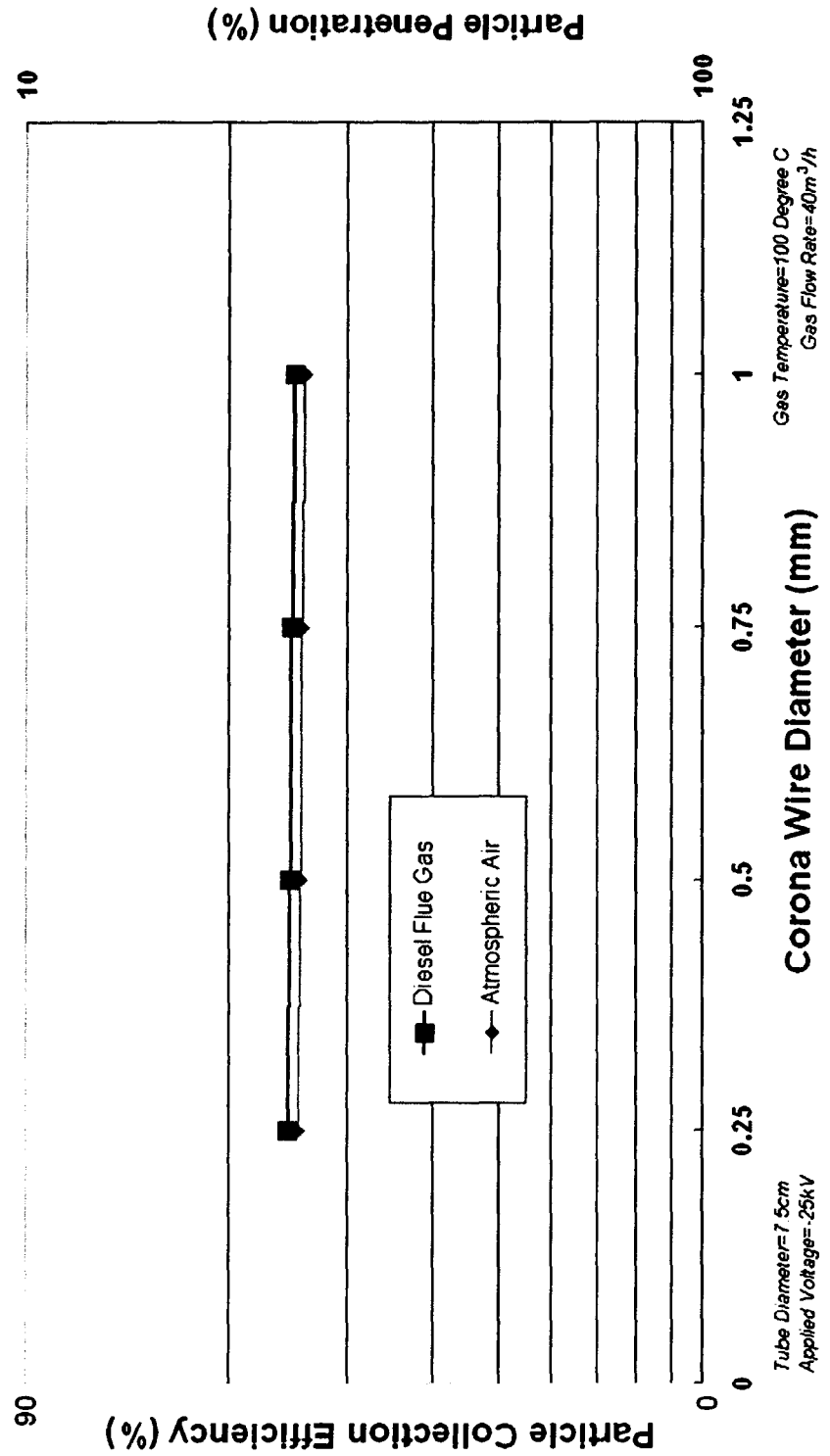

Figure A.22 Particle collection efficiency as functions of corona wire diameter for different flue gas properties

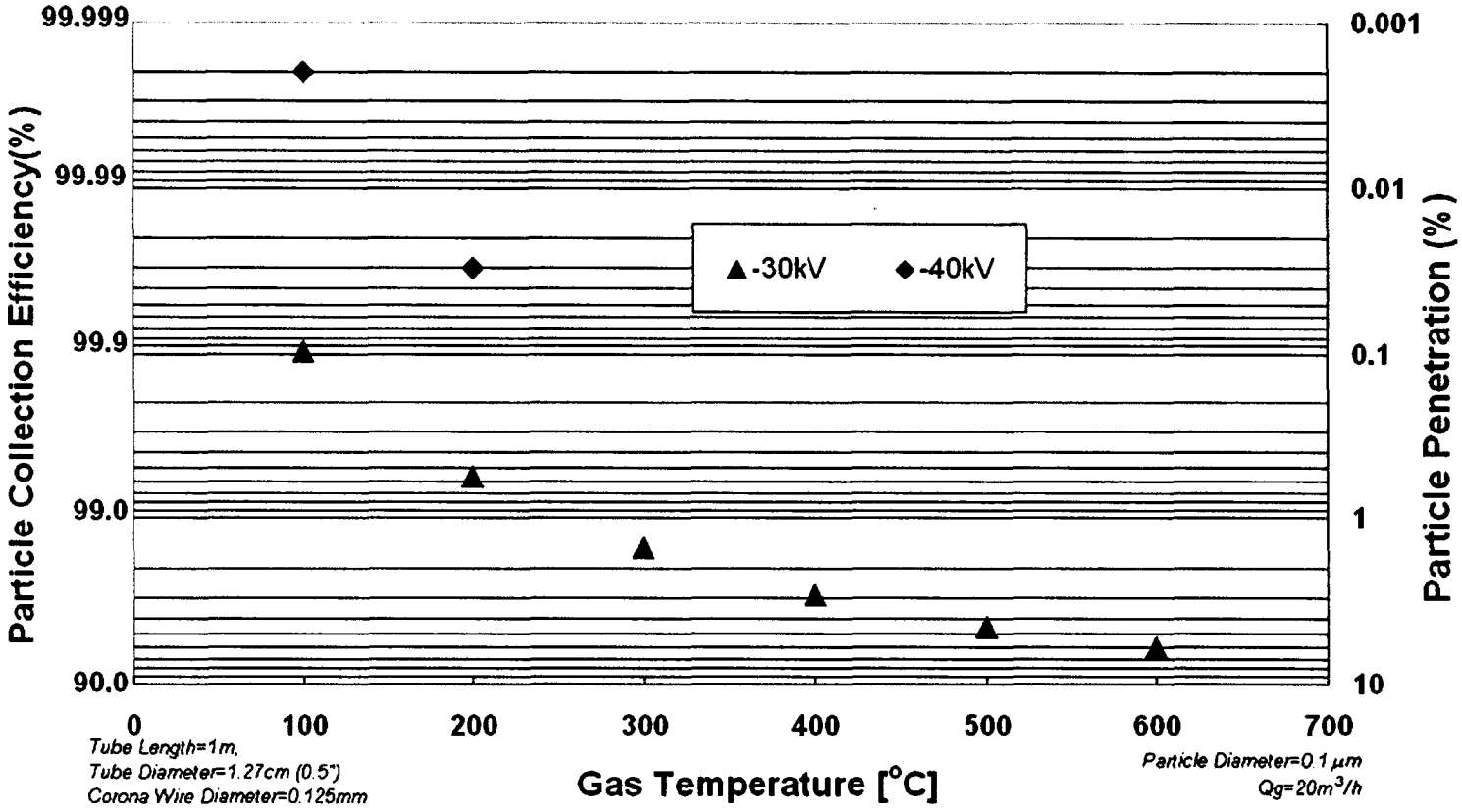

Figure A.23 Particle collection efficiency as a function of exhaust gas temperature

APPENDIX B

EXPERIMENT RESULTS WITH 0.23MM SIZE CORONA WIRE AND RELATED EHD EFFECTS

A 0.23mm diameter corona wire is examined for the number particle collection efficiency, and the results are shown in Figure B.1. Temperature at upstream (MP1) was around 140°C, and about 90°C at downstream (MP2). The total gas flow was set at 2.5Nm^3/h. It is observed from the results that particle collection efficiency is reduced with increasing ESP applied voltage, even dropping to a negative value at 20kV, which means the outlet particle number density is greater than the inlet. The same phenomenon was also observed by Zukeran et al. [76] in the experiment of collection efficiency of ultrafine particles by an ESP for those particles smaller than 0.1μm and heavy particle loading cases. The principle cause is maybe due to the particles reentrainment from the collection electrode caused by electrohydrodynamic (EHD) induced secondary flow. Another factor could be the disjointing of agglomerates according to Zukeran et al [76].

The EHD effect as a function of ESP applied voltage is analyzed, where $(Ehd/Re^2)<<1$ is the condition that EHD secondary flow can be neglected [89][100]. In Figures B.2 and B.3 present the results for 0.23mm and 0.70mm diameter corona wires respectively at various gas flow rates, and figure B.4 for different size of corona wire at 8.5Nm^3/h gas flow rate. Firstly, the ratio of EHD to Reynolds number square increases as decreasing the gas flow rate. Secondly, EHD effect is not neglectable for 0.23mm

diameter corona wire since the ratio of EHD to Reynolds number square is way greater than 1 according to figure B.2. Thirdly EHD flow of 0.7mm wire is much smaller than that of 0.23mm wire, as compared in Figure B.4. The EHD effects of 0.7mm wire on the flow velocity measured at upstream (MP1), downstream (MP2) and middle of the main channel (MP3) are also tested. Results are presented in Figures B.5 to B.12.

Therefore, all the experiments for ESP performances were conducted for the 0.70mm diameter corona wire.

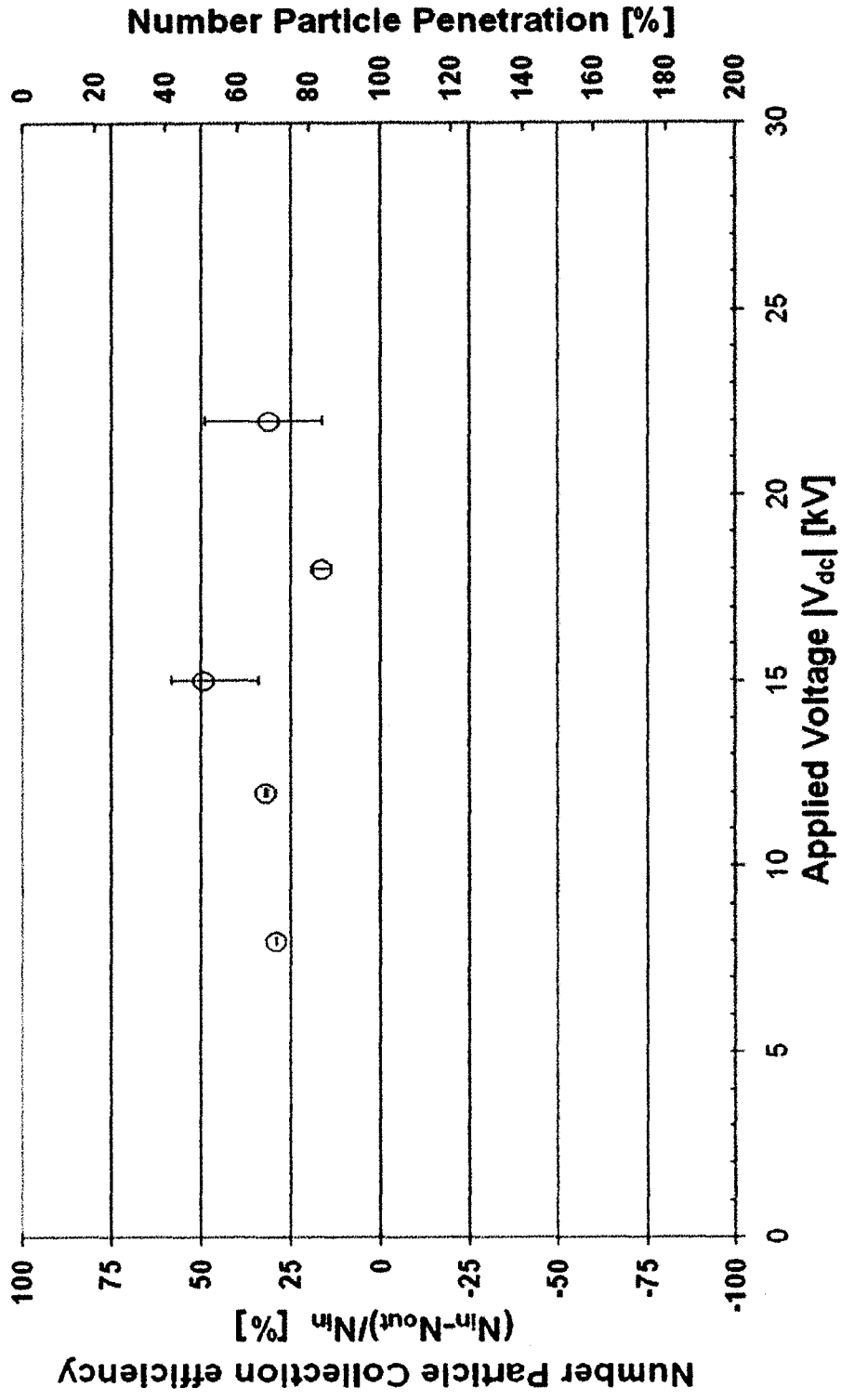

Figure B.1 Particle collection efficiency based on number density versus ESP voltage for 0.23mm diameter corona wire at 2.5Nm^3/h gas flow rate

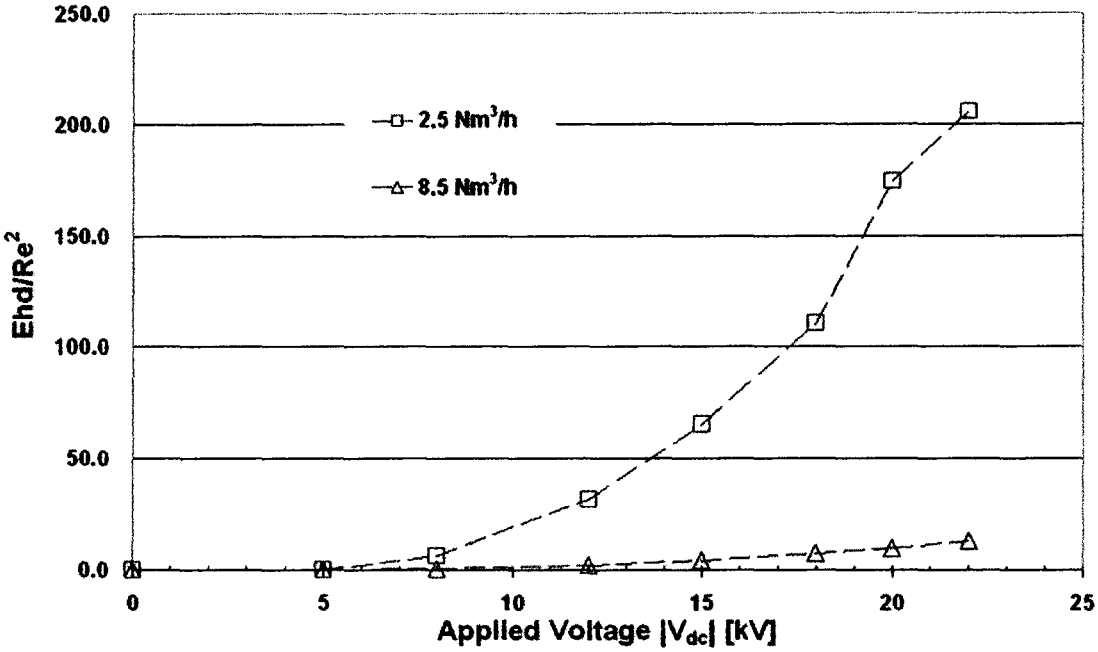

Figure B.2 The EHD number as a function of ESP applied voltage for 0.23mm diametercorona wire at various gas flow rates

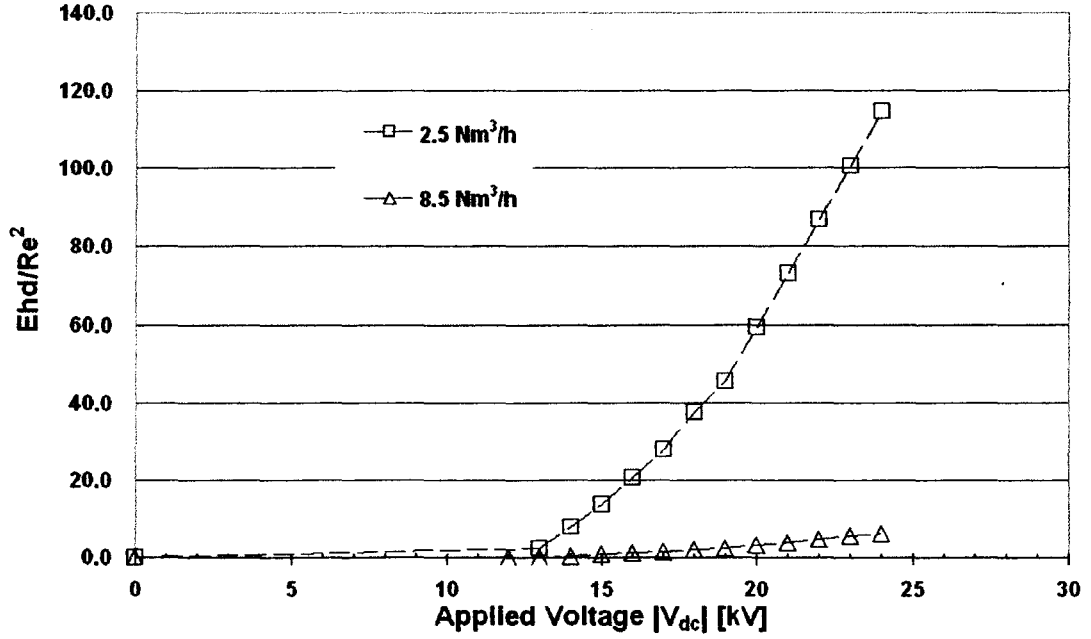

Figure B.3 The EHD number as a function of ESP applied voltage for 0.70mm diameter corona wire at various gas flow rates

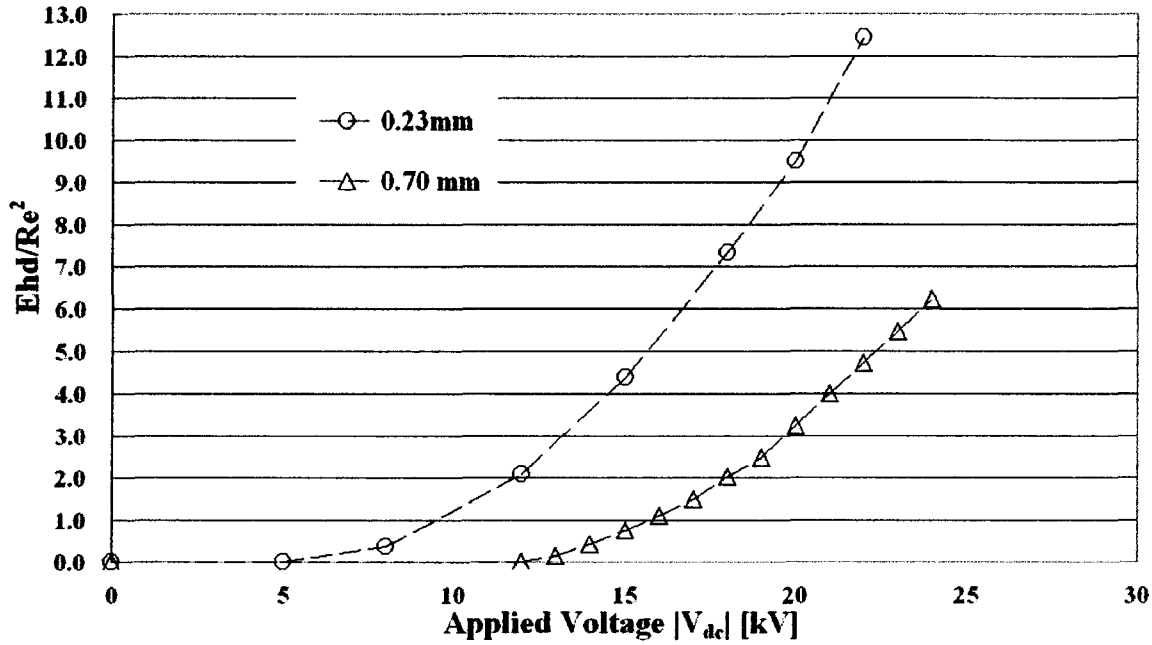

Figure B.4 The EHD number as a function of ESP applied voltage for various corona wire diameters at 8.5Nm^3/h gas flow rate

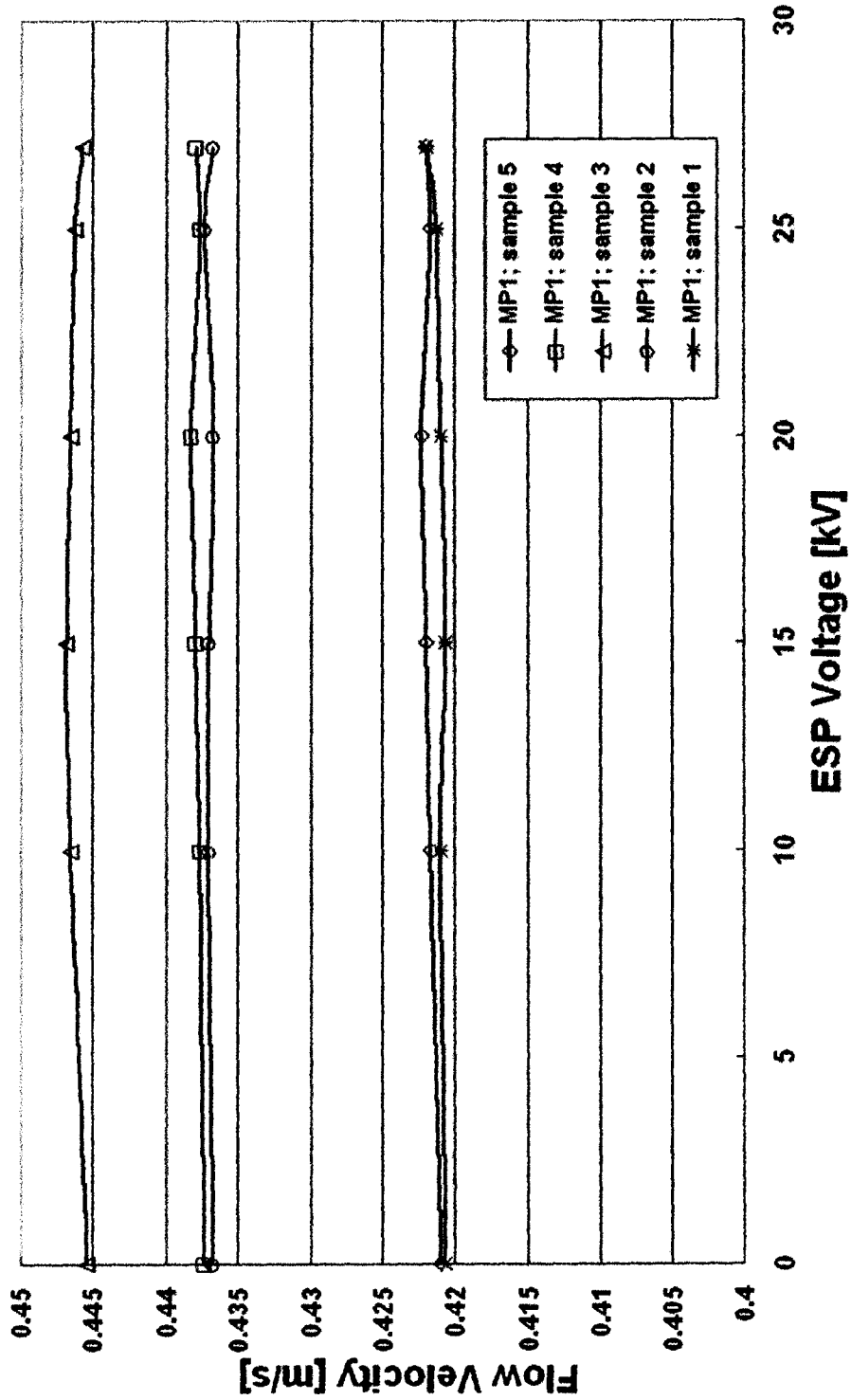

Figure B.5 Time averaged flow velocity at upstream (MP1) vs. ESP voltage at various Pitot tube locations for Q at 7 Nm^3/h

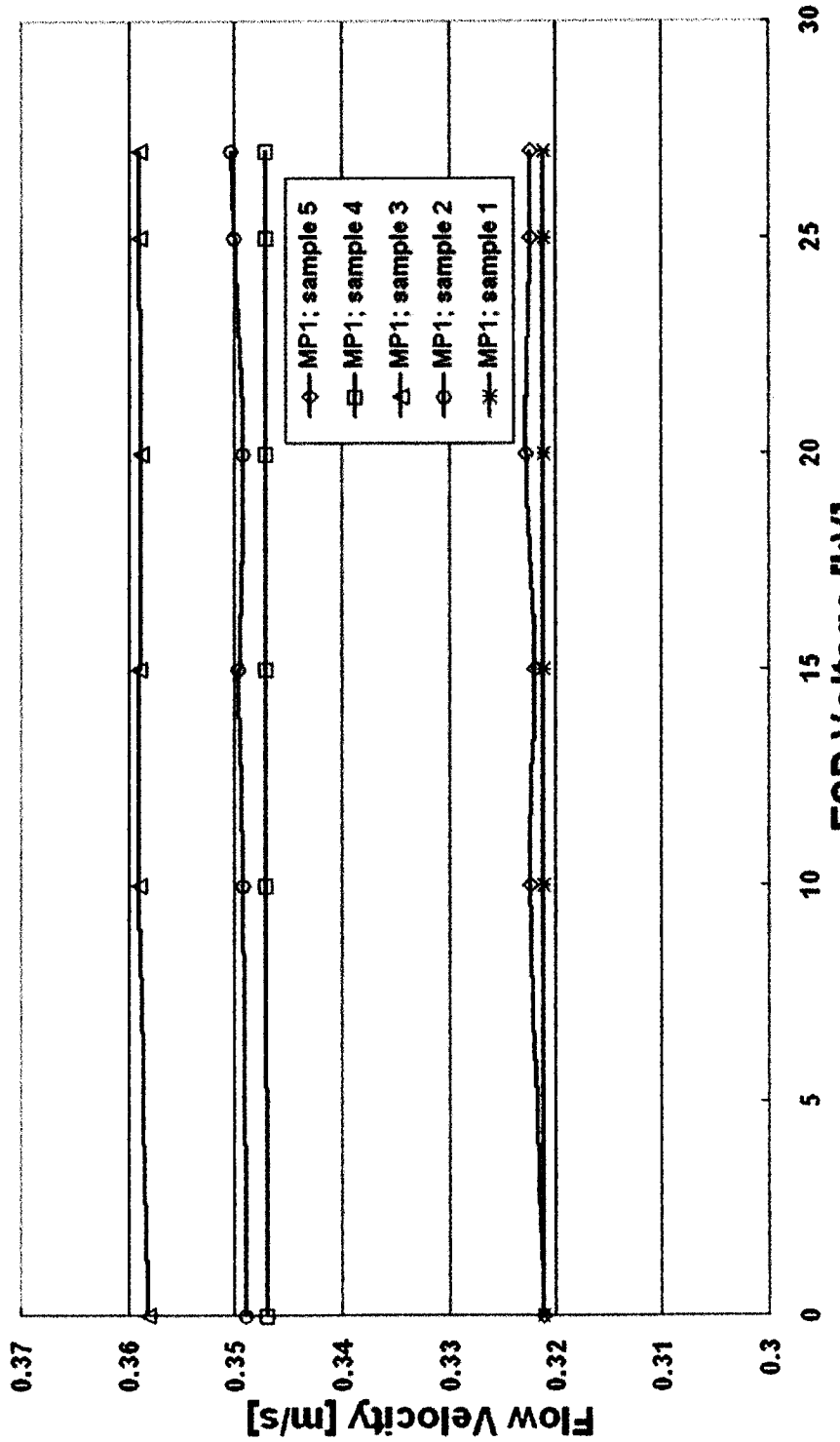

Figure B.6 Time averaged flow velocity at upstream (MP1) vs. ESP voltage at various Pitot tube Locations for Q at 5 Nm^3/h

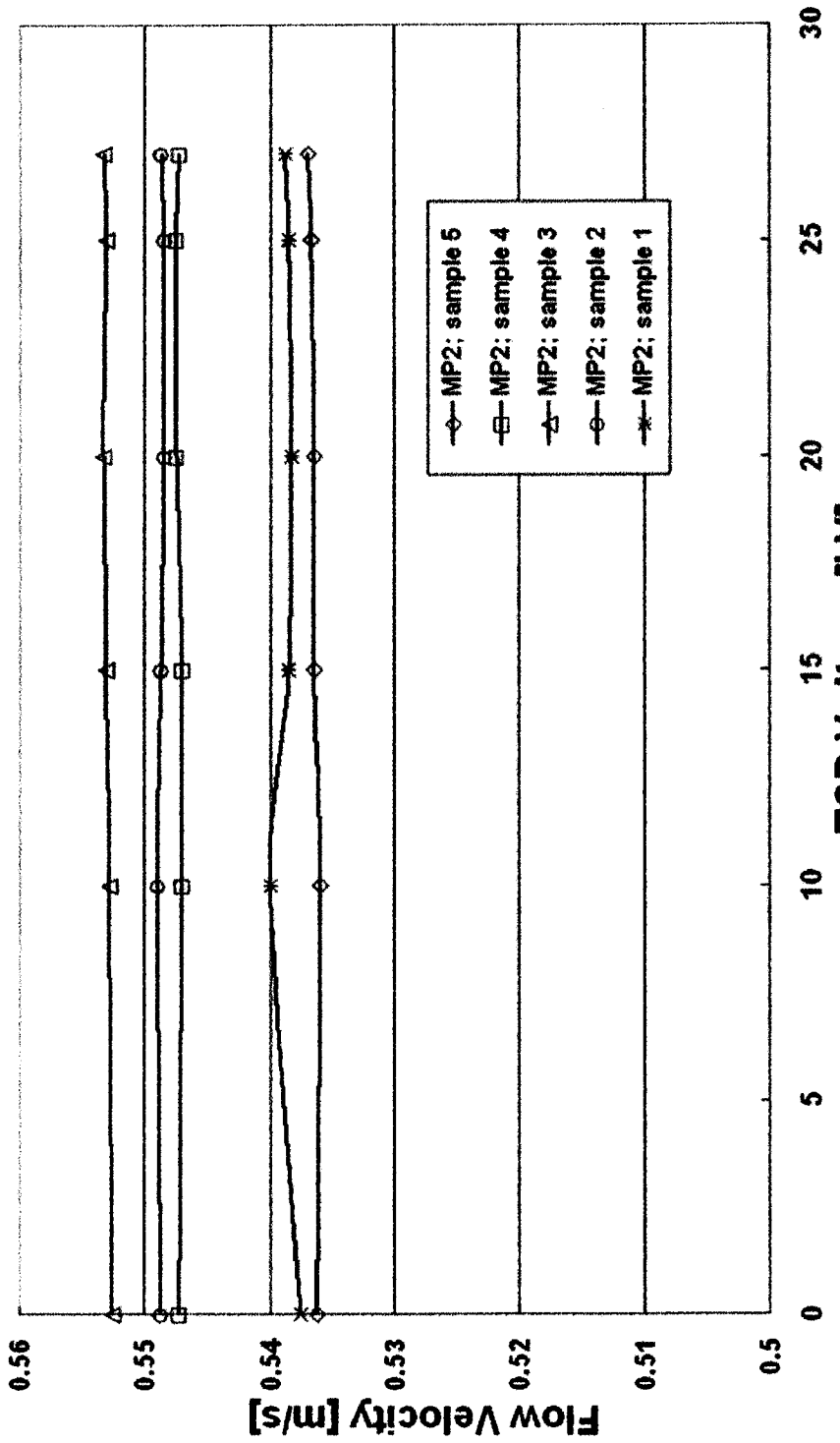

Figure B.7 Time averaged flow velocity at downstream (MP2) vs. ESP voltage at various Pitot tube locations for Q at 8.5 Nm^3/h

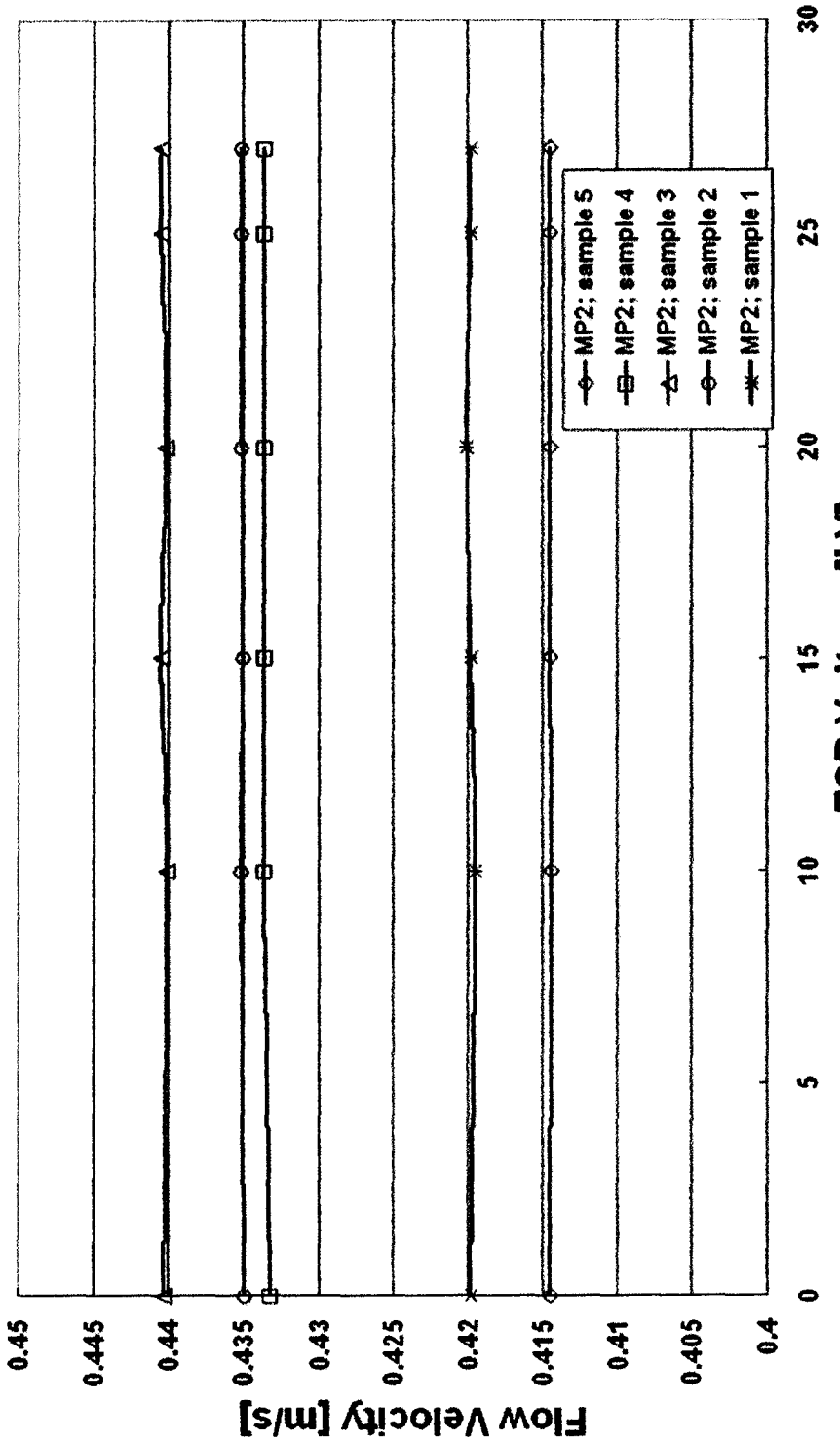

Figure B.8 Time averaged flow velocity at downstream (MP2) vs. ESP voltage at various Pitot tube locations for Q at 7 Nm^3/h

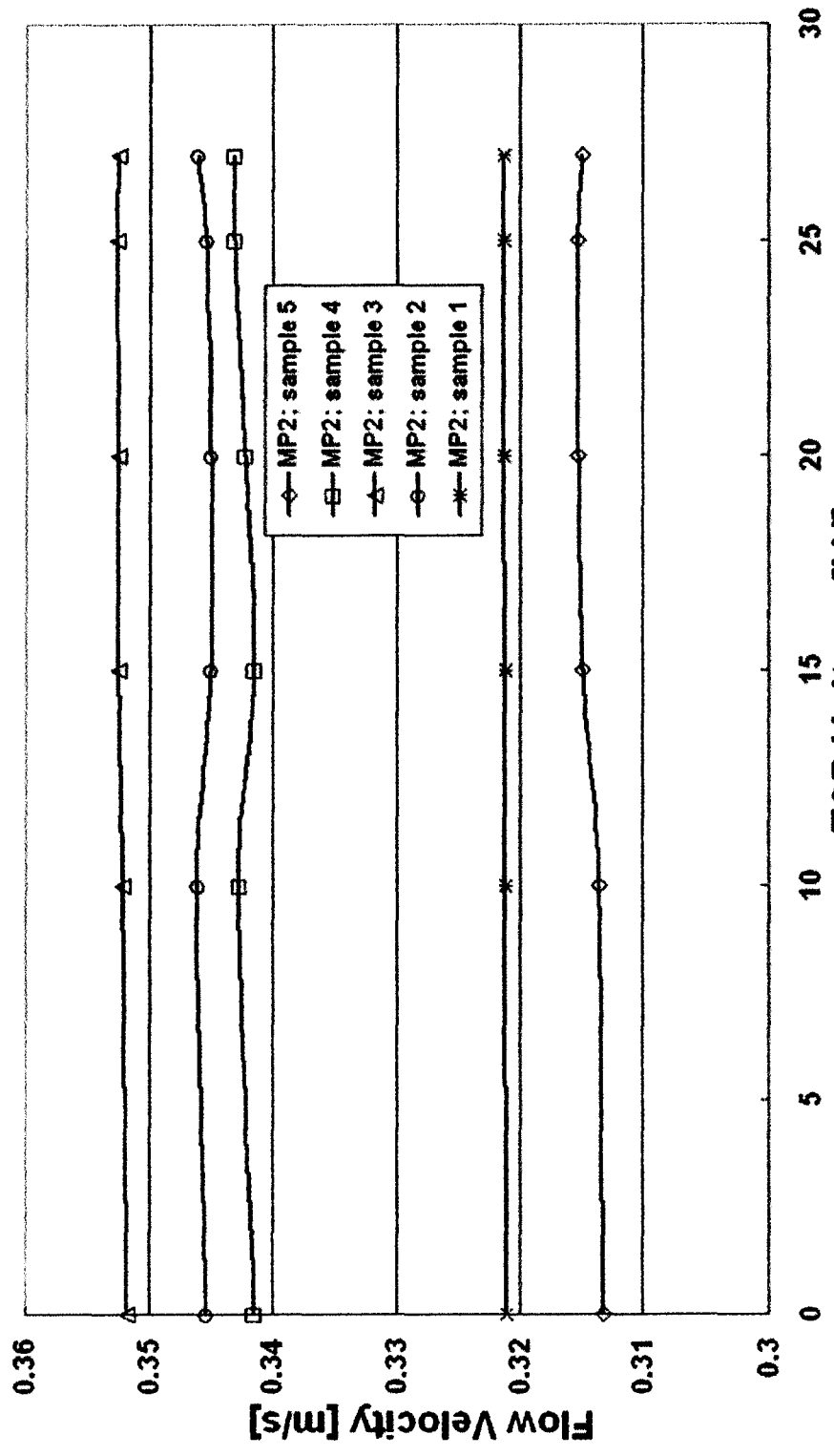

Figure B.9 Time averaged flow velocity at downstream (MP2) vs. ESP voltage at various Pitot tube locations for Q at 5 Nm^3/h

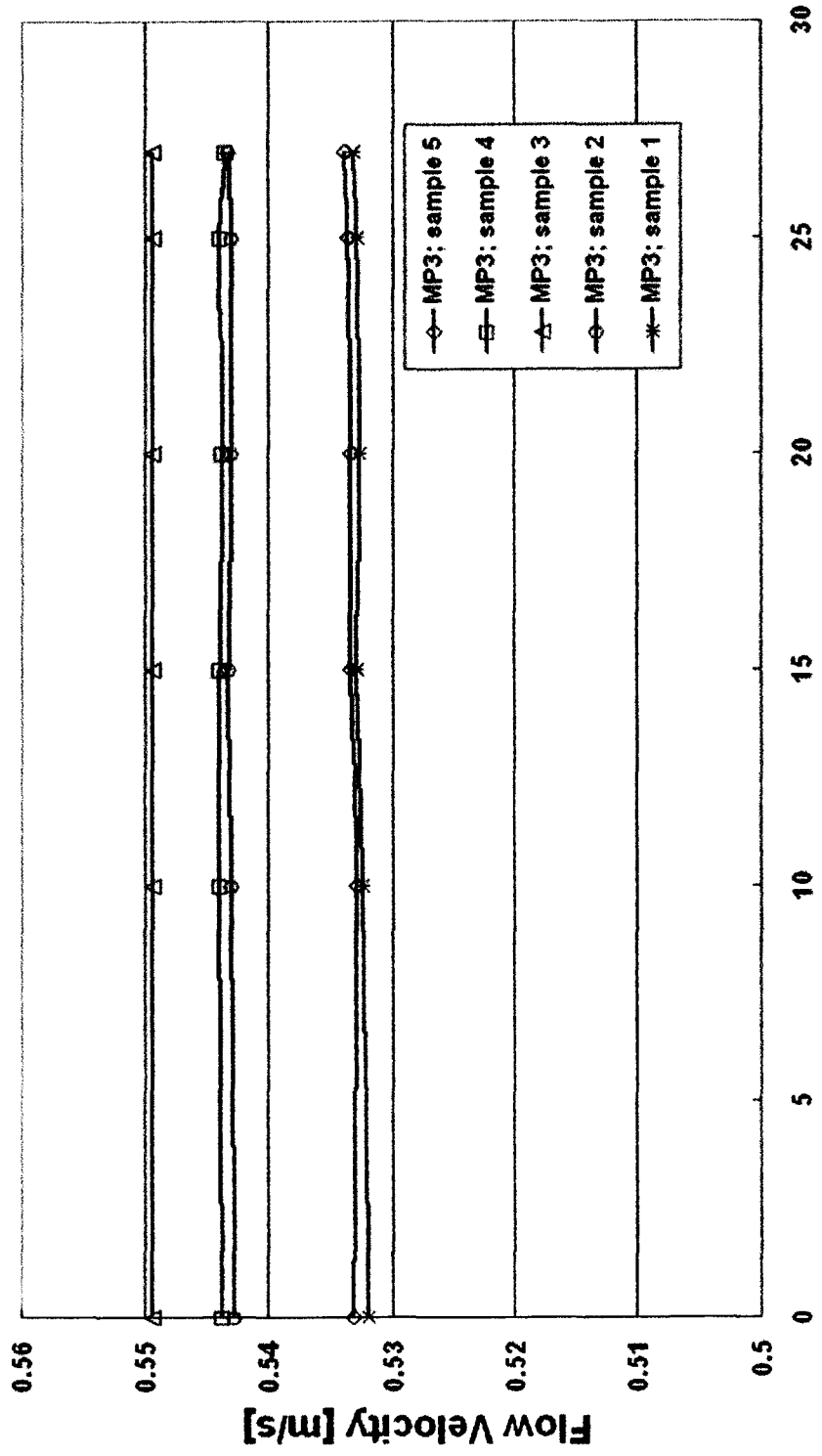

Figure B.10 Time averaged flow velocity at MP3 vs. ESP voltage at various Pitot tube locations for Q at 8.5 Nm^3/h

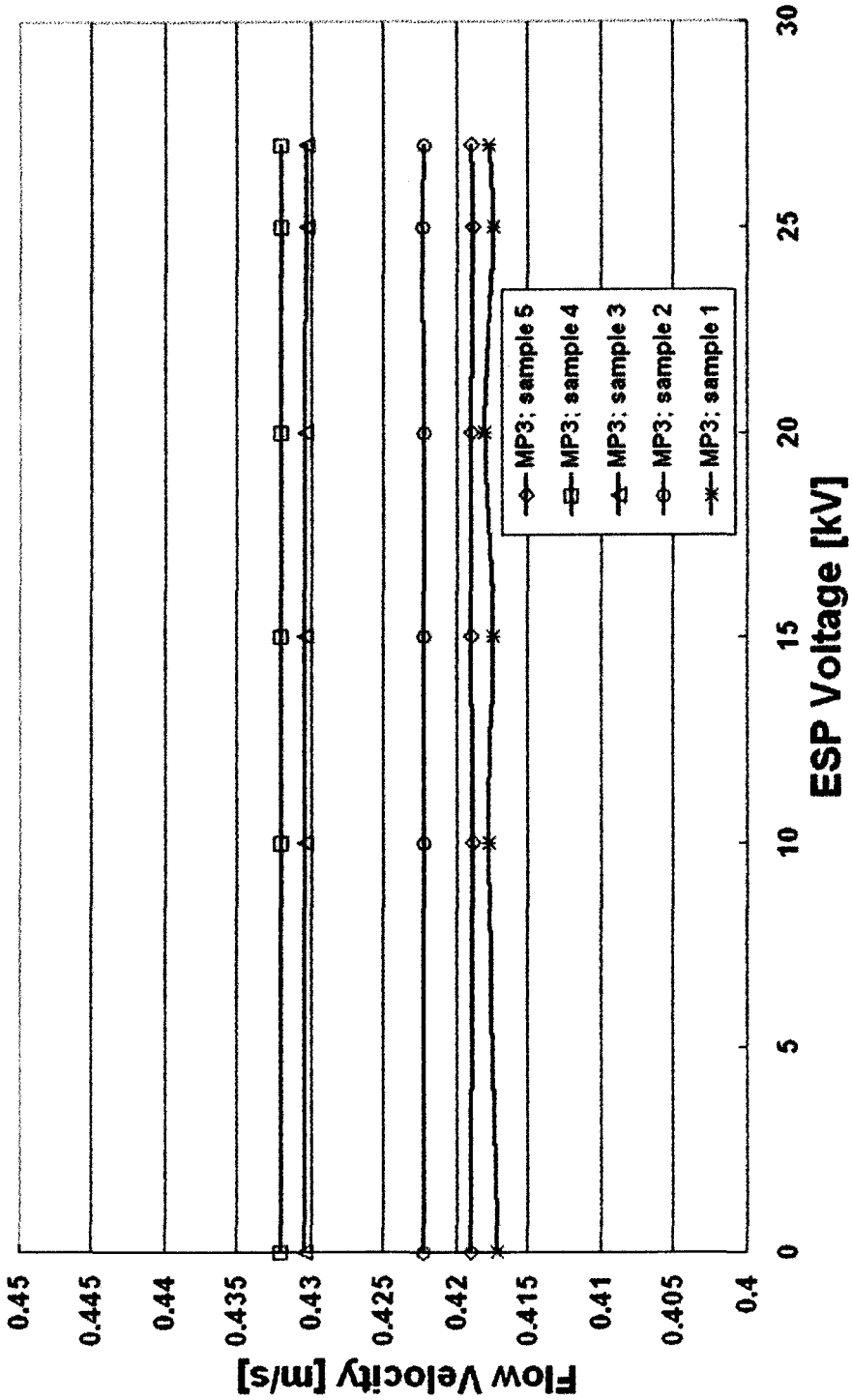

Figure B.11 Time averaged flow velocity at MP3 vs. ESP voltage at various Pitot tube locations for Q at 7 Nm^3/h

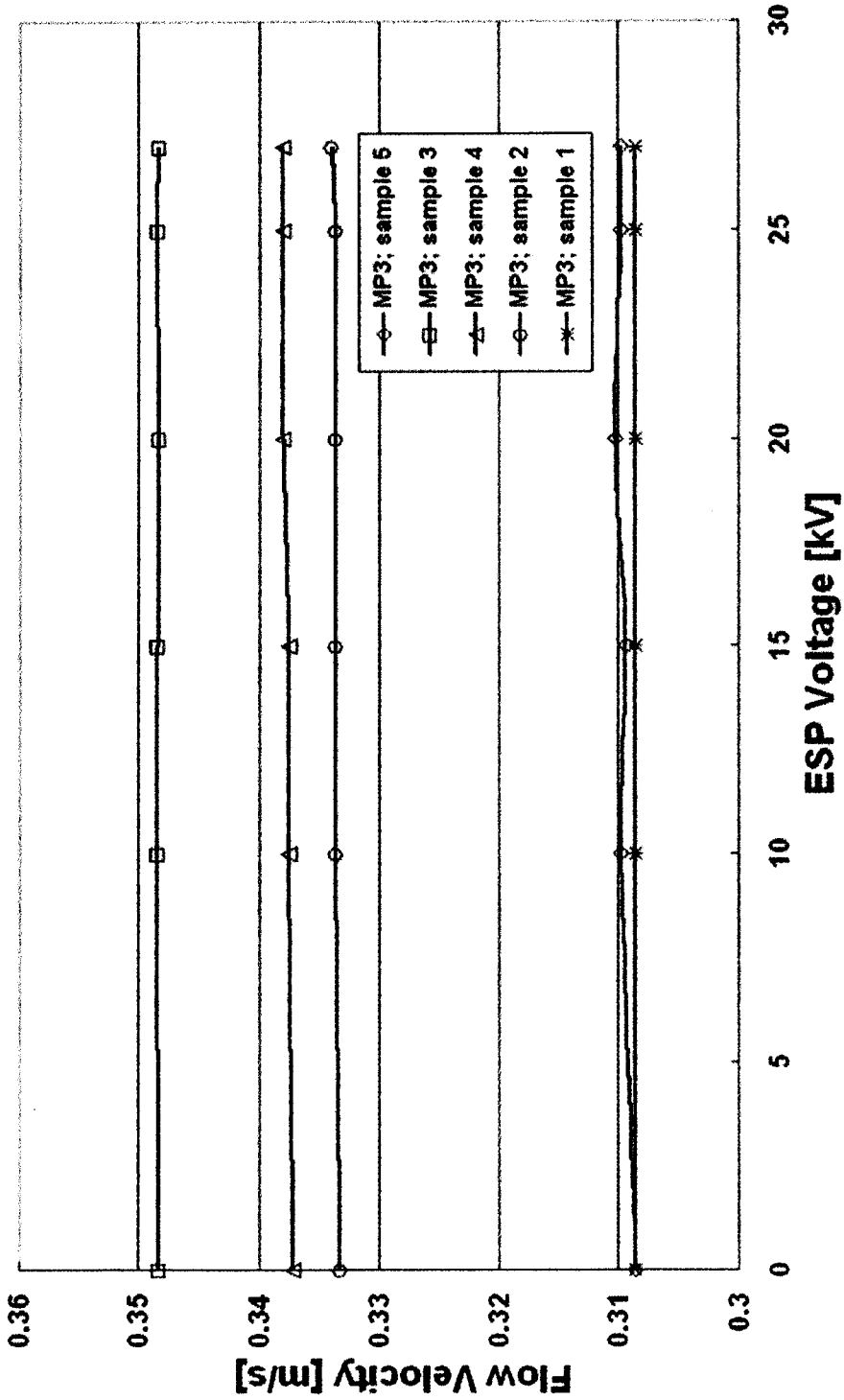

Figure B.12 Time averaged flow velocity at MP3 vs. ESP voltage at various Pitot tube locations for Q at 5 Nm^3/h

Appendix C

Table: Corrected flow and corresponding sampling probe size in the loop with different temperature

				Q [indicated] on the flow meter [scfm]				
				1.5	3	4	5	6
T	Density	Viscosity		Q in the loop				
°C	kg/m^3	kg/(m*s)	m^2/s	scfm				
160	0.81559	2.42E-05	2.96E-05	3.14	6.43104028	8.712365	11.2	13.76682
155	0.82552	2.40E-05	2.90E-05	3.10	6.3536827	8.607566	11.1	13.60122
150	0.83559	2.38E-05	2.85E-05	3.06	6.27711215	8.503833	11.0	13.43731
145	0.84575	2.36E-05	2.79E-05	3.02	6.20170517	8.401676	10.8	13.27589
140	0.85598	2.34E-05	2.73E-05	2.99	6.12758726	8.301266	10.7	13.11722
135	0.86624	2.32E-05	2.68E-05	2.95	6.05501033	8.202944	10.6	12.96186
130	0.87649	2.30E-05	2.62E-05	2.92	5.98420078	8.107015	10.4	12.81028
125	0.88669	2.28E-05	2.57E-05	2.88	5.91536179	8.013757	10.3	12.66292
120	0.89688	2.26E-05	2.52E-05	2.8	5.84815376	7.922707	10.2	12.51904
115	0.90715	2.24E-05	2.47E-05	2.82	5.78194581	7.833013	10.1	12.37731
110	0.91759	2.22E-05	2.41E-05	2.79	5.71616097	7.743892	9.98	12.23649
105	0.9283	2.19E-05	2.36E-05	2.76	5.65021237	7.654549	9.86	12.09531
100	0.93938	2.17E-05	2.31E-05	2.72	5.58356804	7.564264	9.75	11.95265
95	0.95094	2.05E-05	2.15E-05	2.69	5.51569199	7.472309	9.63	11.80735
90	0.96306	2.13E-05	2.21E-05	2.66	5.44627764	7.378271	9.51	11.65875
85	0.97585	2.11E-05	2.16E-05	2.62	5.37489588	7.281568	9.38	11.50595
80	0.98941	2.09E-05	2.11E-05	2.59	5.30123219	7.181773	9.25	11.34826

(Continue)

				Q [indicated] on the flow meter [scfm]				
				1.5	3	4	5	6
Temperature	Density	Viscosity		Sampling Probe Diameter				
°C	kg/m^3	kg/(m*s)	m^2/s	cm				
160	0.81559	2.42E-05	2.96E-05	0.660379	0.461185	0.396231	0.4275	0.386051
155	0.82552	2.40E-05	2.90E-05	0.664387	0.463984	0.398635	0.430095	0.388394
150	0.83559	2.38E-05	2.85E-05	0.668427	0.466806	0.401059	0.43271	0.390756
145	0.84575	2.36E-05	2.79E-05	0.672478	0.469635	0.40349	0.435333	0.393124
140	0.85598	2.34E-05	2.73E-05	0.676533	0.472467	0.405923	0.437958	0.395495
135	0.86624	2.32E-05	2.68E-05	0.680576	0.47529	0.408349	0.440575	0.397858
130	0.87649	2.30E-05	2.62E-05	0.68459	0.478094	0.410758	0.443174	0.400205
125	0.88669	2.28E-05	2.57E-05	0.688562	0.480868	0.413141	0.445745	0.402527
120	0.89688	2.26E-05	2.52E-05	0.692508	0.483623	0.415508	0.448299	0.404833
115	0.90715	2.24E-05	2.47E-05	0.696461	0.486384	0.41788	0.450858	0.407144
110	0.91759	2.22E-05	2.41E-05	0.700457	0.489175	0.420278	0.453445	0.409481
105	0.9283	2.19E-05	2.36E-05	0.704533	0.492021	0.422723	0.456084	0.411863
100	0.93938	2.17E-05	2.31E-05	0.708725	0.494949	0.425239	0.458798	0.414314
95	0.95094	2.05E-05	2.15E-05	0.713073	0.497985	0.427847	0.461612	0.416856
90	0.96306	2.13E-05	2.21E-05	0.717603	0.501148	0.430565	0.464544	0.419504
85	0.97585	2.11E-05	2.16E-05	0.722352	0.504465	0.433415	0.467619	0.42228
80	0.98941	2.09E-05	2.11E-05	0.727353	0.507958	0.436416	0.470857	0.425204

Appendix D

A copyright (figures, tables and text etc) of this thesis is co-owned with my supervisors Dr. J. S. Chang and Dr. G. D. Harvel.